Ulm University Medical Centre

Institute of Orthopaedic Research and Biomechanics
Centre for Trauma Research Ulm
Director: Univ. Prof. Dr. Anita Ignatius

Computational investigation on the aetiology of adolescent idiopathic scoliosis

Dissertation to obtain the Doctoral Degree of Human Biology

at the Medical Faculty of Ulm University

by Franz Benedikt Johannes Schlager
born in Göttingen

2018

Acting Dean: Prof. Dr. rer. nat. Thomas Wirth

1st reviewer: Prof. Dr. Hans-Joachim Wilke

2nd reviewer: Priv.-Doz. Dr. med. Michael Akbar

Day of graduation: 9th of November 2018



[Modified from Nicolas Andry, "L'Orthopedie", 1741]

Dedicated to my parents.

Table of contents

Abbreviations VI

Journal articles based on this dissertation VIII

1. Introduction 1

1.1 Mechanobiology - Bone growth and mechanical interaction 3

1.1.1 Bone growth 4

1.1.2 Mechanical stimuli for bone growth 5

1.2 Biomechanics of the spine and chest 5

1.2.1 The spine 6

1.2.2 The chest 7

1.3 Mechanical loads acting on the spine 9

1.4 Spinal deformation: scoliosis 14

1.4.1 Pathology and treatment 14

1.4.2 Aetiology hypothesis for AIS 15

1.5 Aim of this thesis 20

2. Material and Methods 21

2.1 Morphology quantification 22

2.1.1 Patient group 22

2.1.2 Landmark placement 23

2.1.3 Morphology parameters 23

2.1.4 Statistical analysis 25

2.2 Finite element model of the chest and spine 25

2.2.1 Spinal segment 26

2.2.2 Costovertebral joint (CVJ) 32

2.2.3 Material calibration 37

2.3 Intrapleural pressure model 40

2.3.1 Background to pleura mechanics 40

2.3.2 Pleura model generation 41

3. Results 44
3.1 Morphology analysis 44
3.1.1 Non-scoliotic (healthy) patient group 45
3.1.2 Comparison between AIS and healthy groups 46
3.2 Finite Element model of the spine and chest 52
3.2.1 Spinal segment 52
3.2.2 Costovertebral joint 57
3.2.3 Material calibration algorithm 60
3.3 Intrapleural pressure analysis 61
4. Discussion 68
4.1 Morphology analysis 68
4.2 Finite element model of the spine and chest 70
4.2.1 Spinal segment 70
4.2.2 Costovertebral joint 71
4.2.3 Material calibration algorithm 72
4.3 Intrapleural pressure analysis 73
4.4 Outlook 77
4.4.1 Numerical model of the spine and chest 77
4.4.2 Aspects on an asymmetry in the intrapleural pressure 78
5. Summary and Conclusion 80
6. Literature 82
Appendix 98
Acknowledgment 104
Curriculum vitae *(removed)* 105

Abbreviations

Abbreviation	Description
2-d	Two-dimensional
3-d	Three-dimensional
ACC	articulatio capitis costae
ACT	articulatio costotransversalis
AIS	Adolescent idiopathic scoliosis
ALL	Anterior longitudinal ligament
c.b.	Cranial border
CL	Capsular ligament
cm	centimetre
CT	Computer tomograph
CVJ	costo vertebral joint
e.g.	“exempli gratia” (for example)
Ext	Extension
F	force
FCT	fovea costalis transversalis
FE	Finite element
FEM	Finite element model
i.c.s.	Intercostal space
IAP	intraabdominal pressure
IPP	Intrapleural pressure
ISL	Inter spinal ligament
IVD	Intervertebral disc
LCCI	ligamentum capitis costae intraarticulare
LCCR	ligamentum capitis costae radiatum
LCT	ligamentum costotransversarium
LCTL	ligamentum costotransversarium laterale
LCTS	ligamentum costotransversarium superior
LF	Ligamentum flavum
M	moment

m	metre
mm	millimetre
MPa	mega pascal
N	Newton
Nm	Newton meter
NUC	nucleus
Pa	pascal
PLL	Posterior longitudinal ligament
Ref	Reference
RoM	range of motion
SSL	Supra spinal ligament
VA	Vertebral arch
VB	Vertebral body

Journal articles based on this dissertation

Parts of this dissertation were published in the following journals:

Schlager B, Krump F, Boettinger J, Niemeyer F, Ruf M, Kleiner S, Beer M, Wilke HJ. 2018. Characteristic morphological patterns within adolescent idiopathic scoliosis may be explained by mechanical loading. Eur Spine J. 27:2184–2191. DOI: 10.1007/s00586-018-5622-0

Schlager B, Niemeyer F, Galbusera F, Wilke HJ. 2018. Asymmetrical intrapleural pressure distribution: a cause for scoliosis? A computational analysis. Eur J Appl Physiol. 118:1315–1329. DOI: 10.1007/s00421-018-3864-5

Schlager B, Niemeyer F, Galbusera F, Volkheimer D, Jonas R, Wilke H-J. 2018. Uncertainty analysis of material properties and morphology parameters in numerical models regarding the motion of lumbar vertebral segments. Comput Methods Biomech Biomed Engin. DOI: 10.1080/10255842.2018.1508571 *[Epub ahead of print]*

Schlager B, Niemeyer F, Liebsch C, Galbusera F, Boettinger J, Vogele D, Wilke H.-J. 2018 .Influence of morphology and material properties on the range of motion of the costovertebral joint – a probabilistic finite element analysis, Comput Methods Biomech Biomed Engin. DOI: 10.1080/10255842.2018.1516762 *[Epub ahead of print]*

1. Introduction

The design of the human spine has fascinated researchers of many disciplines throughout history. In particular, the relationship between form and function has been subject of research in philosophy, anthropology, biology, medicine and engineering. Certain medical specialties, such as orthopaedics, have even chosen the investigation and treatment of abnormalities in the spinal form as a symbol (Figure 1). In this thesis, the focus was placed on bony deformities of the thorax and how they interact with the development and shape of the spinal curvature.

One of the most common spinal "deformities" is scoliosis. Scoliosis is characterised by a three-dimensional deformation of the straight spine to a C- or S-shaped spinal curvature within the frontal plane.

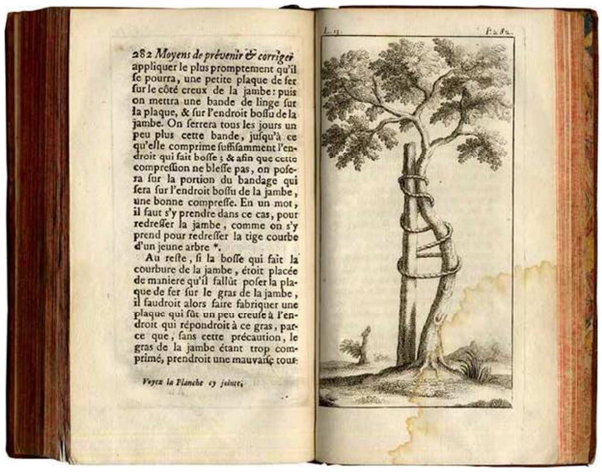


Figure 1: "The crooked tree", symbol of Orthopedics. Drawn in "L'Orthopedie" or the Art of Correcting and Preventing Deformities in Children, from Nicolas Andry in 1741. [Figure used by courtesy of Hagströmer Library, Karolinska Institute, Stockholm, Schweden]

Despite extensive research, the causes of scoliosis during adolescence in 85% of cases are still unknown, therefore called idiopathic. While different hypotheses for the causation of the deformity have been proposed [67, 181], no single causative factor has yet been identified [91, 155]. Therefore, no clear consensus on the optimal strategy for the treatment and correction of this spinal deformity has been found [13, 90].

A scoliotic condition of the spine, considered as a mechanical imbalance, requires a representative model to investigate the biomechanics and the aetiology of this spinal deformity.

Animal models have been used to investigate hypotheses for the development and treatment of scoliosis [82]. The basic drawbacks of these animal models include, not only ethical concerns, but also primarily the different biomechanical loading mechanisms

between the quadrupedal animals and the bipedal upright posture of humans. Additionally, the reproducibility of certain scoliotic patterns in animals is low.

In vitro models of scoliosis have been created by manually deforming normal spines post-mortem by dissecting certain structures and fixing the spinal curvature using either screws and rods [182], or adhesive and silicon [162, 186]. Thus, major curvatures in the frontal plane (with Cobb-angles > 40°) could be artificially produced [186]. A main limitation of these models lies in the fact that the mechanics of the soft tissue are strongly altered and an accurate reproduction of the scoliosis types is very difficult.

Numerical models, as applied in this study, have the potential to consider the individual morphology of patients, analyse particular complex loading conditions, and allow for performing extensive parameter studies. Within numerical models, multiple data sets can be assembled from various *in vivo* and *in vitro* experiments to explore hypotheses and perform predictions. In addition, they allow for the analysis of usually inaccessible regions within experiments.

The validity of a numerical model, however, is always limited by the accuracy of the numerical formulation of the nature, as well as, the amount and quality of the experimental data that has been used for verification and validation [176]. Numerical models of the spine have been recently developed to simulate surgical approaches [25, 34, 61, 69, 107, 108, 110, 118, 119, 139, 174, 180, 192] or brace treatment [40]. With the increasing amount of computer power and implementation of more sophisticated material models, numerical models have the potential to be of great benefit to biomechanical research.

Within this thesis, the aetiology of scoliosis was investigated by analysing the interaction between the morphology of the spine and mechanical loads which potentially trigger the deformation, as illustrated in Figure 2.

During adolescence, a scoliotic spine shows characteristic changes in the shape and biomechanical imbalance. Yet, what enables the spine to develop in a certain way and which factors trigger an abnormal development? Furthermore, to what forces is the spine exposed, and what are the biomechanical characteristics of the thorax?

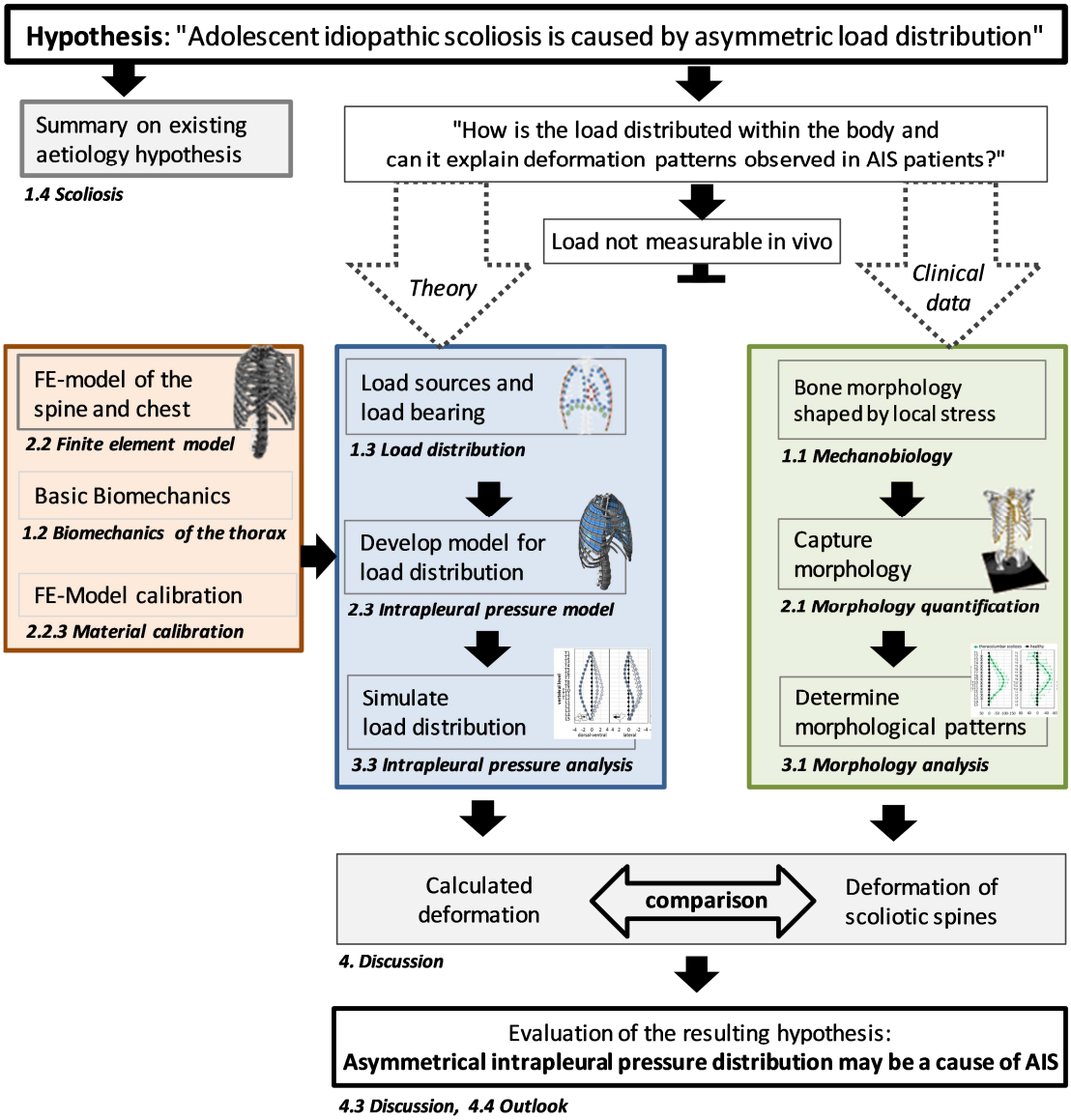


Figure 2: Illustration of the approach and line of argument for investigating the hypothesis. (FE: Finite Element, AIS: adolescent idiopathic scoliosis)

These questions are relevant for understanding and developing an adequate biomechanical model of the spine and chest. Structural and biomechanical characteristics are outlined in the following sections.

1.1 Mechanobiology - Bone growth and mechanical interaction

The skeleton exhibits a close relationship between form and function [27]. In the context of analysing the bone morphology of patients, the different stages of bone modelling and its mechanical adaptation during adolescence are briefly described.

1.1.1 Bone growth

The relevant regions for bone morphology analysis, are regions in which ossification occurs, due to their high content on osteogenic cells and high potential to adapt to mechanical stimuli [167]. The formation and growth rate of the bone depends on the stage during life development.

In the early stages of foetal development, the mesenchyme cells (mesoderm) give rise to the muscles and skeletal system, in particular to the cartilage, bone, muscle and connective tissue. During foetal development, the mesenchyme extends backwards on either side of the neural tube and surrounds it.

The at first uniformly distributed mesenchymal cells later become condensed in a region which develops to the intervertebral disc (IVD). The IVD grows postnatally most likely due to cell proliferation and matrix synthesis [76, 173]. The growth rate of the IVD is smaller compared to the vertebral body growth [168].

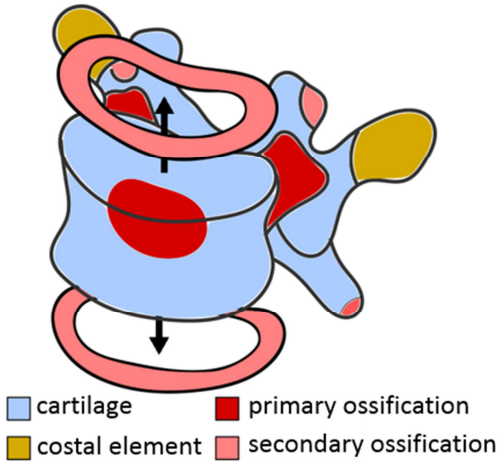


Figure 3: Ossification and growth plates of the vertebral body during adolescence. Figure based on Moore et al. [128] (p. 454).

The vertebral body is built from a framework of cartilage which defines where bone will form. It grows specifically in height by endochondral ossification at the growth plates adjacent to the IVD, as illustrated in Figure 3. An increase in diameter of the vertebral body is mainly attributed to appositional growth [41]. Bone is additionally built from the primary ossification centres. These are regions within the cartilage which are penetrated by capillaries.

The mesenchyme also extends laterally, forming the transverse process, and continues ventrally into the body wall, which is the future position of the ribs. Hereby, the mesenchyme undergoes chondrification (cartilage generation) and subsequent ossification to form the ribs. The sternum is formed by fusion of two sternal bars that develop on either side of the midlines [9].

While this bone modelling occurs primarily during adolescence, bone remodelling dominates after maturity is reached. The bone remodelling process primarily maintains the bone mass during adulthood in order to restore or sustain skeletal integrity. At this stage, old or damaged bone is resorbed by osteoclasts and rebuild by osteoblasts. The shape and mass of the bone remains stable until age-related bone loss begins [100].

1.1.2 Mechanical stimuli for bone growth

Bone adapts to local mechanical stimuli as described by Wolff's Law [190]. If the load increases, the bone becomes stronger. Conversely it dissipates if the load decreases. Specifically, Wolff identified that the trabecular structure of the bone undergoes adaptive changes as it orients along the trajectory of the stress field.

Later, the Hueter-Volkmann Principle extended Wolff's Law [75, 177]. It states that a mechanical compression across the growth plate decreases the longitudinal growth. In contrast, tensile load across the growth plate stimulates longitudinal growth. The length of the bone, therefore, is dependent on the tensile force to which it is locally exposed.

These bone adaptation theories were further redefined on the cellular level by Frost [53, 54]. He suggested that the bone adaptation process depends on the magnitude of strain which the tissue is locally exposed to. Strain values above a certain modelling threshold provoke a strengthening of the bone, whereas strain values below a certain remodelling threshold would cause resorption of the bone.

1.2 **Biomechanics of the spine and chest**

The biomechanics of the body can be divided into three aspects:

1. The intrinsic weight and weight bearing within the body;
2. Passive structures (soft tissue) which provide support and stability within the body;
3. Active structures (muscles) which counterbalance the gravitational forces of the weight and provide movement.

Muscles play an essential role in biomechanics of the spine. Yet, due to their redundant composition and the difficulties in measuring their forces, the influence of each isolated muscle is very difficult to estimate. In this thesis, the focus was placed on the intrinsic loads and the passive structures which support the spine and chest.

1.2.1 The spine

The spine can be separated into functional spinal units (motion segments) which mainly determine the mechanical behaviour (stiffness) of the spine. Excluding the muscles, each spinal unit includes two adjacent vertebrae, an intervertebral disc and seven ligaments. The intervertebral disc consists of a gel-like nucleus which is surrounded by a fibrocartilage ring called the annulus. The pressure within a non-degenerated nucleus is quasi hydrostatic. This pressure is sustained by the annulus ring which provokes a tension stress within the annulus.

The stiffness of a spinal segment is governed by the morphology and material properties of the soft tissue. These vary within subjects and between vertebral levels leading to a wide possible range of motion (RoM) [185].

Material properties

The identification of the material properties is an essential step while modelling the spine, as it affects the mechanical behaviour of the spine. The material parameters are commonly extracted from published literature [43]. However, only a few experimental studies explicitly deal with the measurement of distinct material properties.

In recent years, the properties of the lumbar annulus fibrosus was subject of a few comprehensive studies [48, 49, 74, 84]. The mechanical behaviour of the annulus fibrosus is determined by the properties, orientations and densities of the collagen fibres, as well as the property of its ground substance.

The *in vitro* testing of isolated ligamentous structures revealed high standard deviations, resulting in a wide range of possible material property values which, in turn, impact the mechanical behaviour of the spinal segment [197].

To solve this issue, a stepwise reduction method was introduced to allow for the determination of the material properties. This involved leaving the specimen embedded and performing mechanical testing after step-wise removal of the various anatomical structures [71].

Numerical models to simulate spine biomechanics

Various numerical models have been developed in the past to simulate the biomechanics of the spine. The type and complexity of the models can be differentiated by their application.

Common Finite Element (FE) models generate a representative spinal column which considers the morphology of one ideal (often lumbar) spine [43]. These FE models attempt to replicate the average mechanical behaviour of a spinal segment by modelling the passive structure of the spine. They are mainly utilized in implant research, for instance, to identify the change in stiffness of the spine after instrumentation, or to identify the stresses acting on the implant [12, 57, 108, 111, 156].

Further models focus primarily poroelasticity of the nucleus. This enables the investigation of disc diffusion and disc degeneration processes [56, 116].

Spinal muscles are commonly simulated by using multibody models [8, 55, 165]. These are useful for conducting motion analysis in a relative rapid and robust manner. A typical model comprises a multitude of rigid bodies, joints and constraints together with their kinematic relationships. The main limitation of multibody simulation is that the morphology and biomechanics are numerically very roughly described. Additionally, there is a great lack of calibration/validation data to simulate the spinal muscle architecture.

1.2.2 The chest

The rib cage plays an important role in human trunk biomechanics, such as respiration [6, 26, 189], protection and support of the viscera, as well as, the stabilization of the spine [7, 21, 105, 106, 134].

The chest consists of twelve ribs on the left and right sides, which originate from the thoracic spine and form via the costal cartilage and the sternum a closed mechanical construct.

The main mechanical links between the rib cage and the thoracic spine are the costovertebral joints (CVJ) which provide an articular connection between a rib and its adjacent vertebrae. The costovertebral joint provides a stable link between a rib and the adjacent vertebra and has the ability to transmit high loads to the spine, while simultaneously offering enough flexibility for respiration.

The biomechanical properties of the CVJ were first investigated by Schultz et al. [157]. They performed *in vitro* studies using five human costovertebral articulations at six rib levels by measuring the displacements in superior-inferior, posterior-anterior and medial-lateral directions. Their results indicated that the CVJ stiffness varies depending on the loading direction and the rib level. The stiffness of the CVJ increased from T1 to the mid-thoracic region, and decreased towards the lower rib levels. Lemosse et al. identified that the rotational stiffness along the axis of the rib head was lower than along the cranial-caudal and posterior-anterior axes [104].

Stepwise resection steps were also performed to investigate the influence of each ligament on the RoM of the CVJ. According to Lemosse et al., the ligaments surrounding the articular costo transversalis had the strongest influence on the RoM. Duprey et al. replicated some of the tests from Lemosse, yet with less specimens, and found comparable results [46].

Further *in vitro* and numerical studies of the chest primarily investigated blunt trauma to the chest [88, 160, 170]. *In vitro* experiments on the entire chest by Eckert et al. revealed that the axis of rotation of the CVJ is not fixed and that, therefore, the kinematics cannot be represented by a single axis pivot element [50]. Further *in vivo* measurements identified that the axis of rotation of the joint was not in line with the anatomical axis of the rib neck axis during respiration [16, 17].

Most numerical models of the entire rib cage simplify the CVJ to a single spherical kinematic joint which adheres to a moment–angle relationship obtained from *in vitro* data of Duprey et al. [88, 175]. By varying the CVJ properties within four orders of magnitude, Kindig et al. noticed that the total rib movement depends strongly on the stiffness of the CVJ. They identified that the stiffness of the CVJ effected mainly the magnitude, rather than the direction of rotation of the ribs.

While past numerical models considered the motion of the CVJ within the whole chest, the main goal was to establish a refined, more accurate model of this joint which can subsequently serve as a building block for a reliable model of the complete chest. This study, therefore, focused on the isolated motion and properties of the CVJ in order to find an adequate model that represents the complex biomechanical behaviour of the CVJ, and thus, sufficiently models the load transmission between the ribs and the adjacent

vertebrae. Modelling the load transmission is particularly relevant to simulate the interaction between rib cage and spine. This could be useful to investigate the influence of brace treatment on the spinal shape. *(see [154])*

1.3 Mechanical loads acting on the spine

During daily activities, the upper human body is most frequently in an upright position. In this posture the spine must carry the weight of the upper body and transmit this load to the pelvis. To model the mechanics of the spine in an upright posture, it is necessary to know the magnitude of the loads and how the body weight is transmitted to the spine.

Body segments

The weight of the body segments and organs was measured in a few human cadaver studies [22, 33, 38, 66]. According to the literature, the head contributes in average 6.6 - 8.5 % to the body weight and the torso without extremities 44.2 - 50.7 %. The weight of the upper and lower limbs, human heart, brain, lungs, liver, spleen and kidneys were measured and summarized in Table 1 [126, 127]. In summary, more than 50% of the body weight is located above the pelvis which needs to be transmitted through the spine to the pelvis in an upright posture (Figure 4).

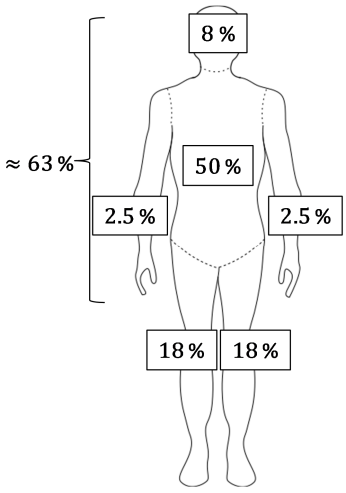


Figure 4: Body weight distribution in % of the total body mass [22, 33, 38, 66]

Table 1: Weight of extremities and main organs that act on the spine.

Structure	Weight [kg]	% of total body mass	Literature
Head (and neck)	5.2 +/- 0.8	7.92 +/- 0.85 %	[38]
Arms	1.6 +/- 0.4	2.64 +/- 0.3 %	[38]
Abdomen	14.2 +/- 4.3	16 +/- 2.6 %	[137]
Lung	0.11 - 0.72	-	[127]
Heart	Total: 0.09-0.7 Mean: 0.2-0.4	-	[126]
Liver	0.9 - 1.9	-	[127]
Spleen	0.03 - 0.23	-	[127]
Kidneys	0.08 - 0.18	-	[127]

Load bearing of the head and arm

The cervical spine balances the weight of the head using several muscles, such as the sternocleidomastoideus and scalenus muscles.

The arm is connected via the shoulder joint (glenohumeral joint) to the thorax. It is a multiaxial joint which involves articulations between the shoulder blade (scapula) and the head of the humerus. The main stability to the shoulder is provided by the connected muscles. Multiple muscles connect the arm with the ribs, scapula and clavicle. From there, widely spread muscles transfer loads to the spine. The scapula can slide within connective tissue along the back of the upper ribs. It creates a compressive force on the rib cage. Thus, the weight of the arms is transmitted to the cervical and upper thoracic spine.

Load bearing within the torso

The major weight contribution of the upper body lies within the torso. A great amount of the gravitational load can be attributed to the bones and muscles. The density of muscles is about 1.06 kg/litre. Theoretically, their weight can estimated by knowing the size of each muscle and their attachment points. The latter can be deduced from literature [51, 136].

Further gravitational loads originate from the intrathoracic and intraabdominal organs.

To date, a correct anatomical schema that addresses the transmission of organ weight to the spine has not been investigated. Previous models have considered the body weight by applying a force at the boy centre of gravity. A bit more advanced study measured the density distribution within the transverse planes and calculated the point of gravity

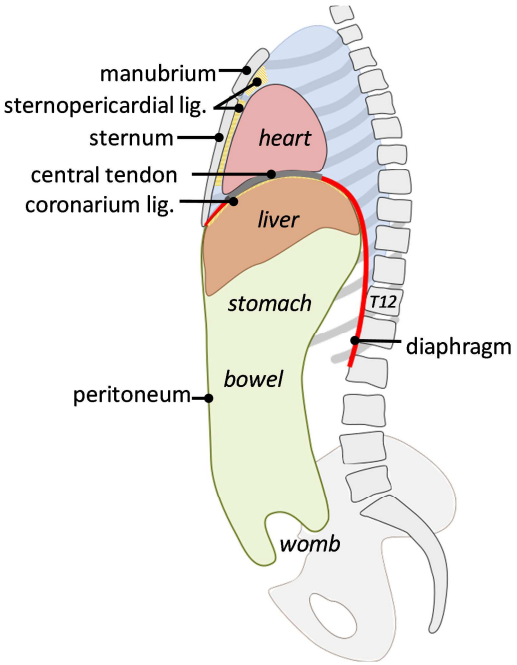


Figure 5: Sketch of the human torso in the sagittal symmetry plane, derived from [136, S.132-180] . The liver is connected via the coronarium ligament to the inferior surface of the diaphragm. The heart via sternoparicaridal ligaments to the sternum.

within transverse cross-sections within the body [137, 138]. This data on gravity distribution continues to be the basis of various numerical models [59]. In these models, the centre of gravity in each transverse plane is applied via a beam to each vertebral level. The main limitation of this approach is that the anatomically correct load bearing structures are not considered, since no beam-like structure is present within the abdomen.

To identify the correct load distribution, it is necessary to analyse the individual organs and their attachment points:

Heart

The heart is located in the middle mediastinum, anteriorly bounded by the sternum and the 2^{nd}-6^{th} costal cartilages and posteriorly by the vertebrae T5-T8. It is contained within a double-walled sac, called the pericardium. The pericardium is attached on the caudally to the central tendon of the diaphragm. Cranially it is connected to the sternum (manubrium and xiphoid process) and is adherent to the mediastinal pleura, as illustrated in Figure 5. It is most likely held in place by the ligaments connected to the sternum (sternopericardial ligaments), as well as by the recoil force of the lungs.

Organs within the peritoneum

The organs in the abdomen are covered by a doubled-walled sac called the peritoneum. It covers the liver, spleen, kidneys, as well as most of the small and large intestine. The outer layer is, called the parietal peritoneum, which is attached to the abdominal and pelvic walls. The liver and spleen belong to the intraperitoneal organs which are covered by the visceral peritoneum. The kidneys lie behind the peritoneum and are only partially covered by the visceral peritoneum, and are therefore referred to as the retroperitoneal organs. The latter are fixed in their location, whereas organs in the intraperitoneal are generally mobile.

The liver is attached to the peritoneum via the falciform ligament and coronarium ligament which connect to the diaphragm and rectus walls, ensuring that the liver stays in place.

The organs are connected to each other by peritoneal ligaments, omenta and mesenteries. Cranially they are attached to the central tendon of the diaphragm and

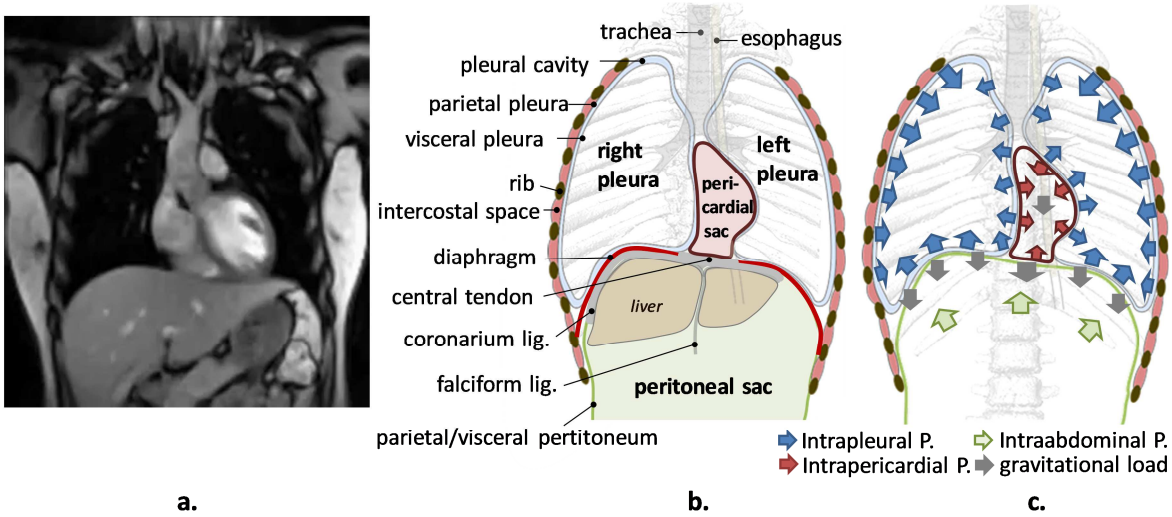


*Figure 6: **a**. Cross-sectional MRI image of the thorax in men.* **b**. Schematic image of the anatomy within the thorax. **c**. Assumed direction of the load vectors within the cross-section surrounding the lung in an upright posture. These vectors originiate from the intrapleural pressure (blue), intrapericardial pressure (red), intraabdominal pressure (green), as well as the weight of the intrathoracic and abdominal organs (gray). The latter is thought to be transmitted through the chest to the spine. (lig.: Ligament, P.: pressure) [*MRI image used by courtesy of J. Frahm, MPI biophysical chemistry, Goettingen, Germany; Adapted with permission by Springer Nature]*

therefore hang within the peritoneum. Thus, the weight within the abdomen is most likely also carried through the central tendon via the pericardium to the sternum.

Pleura

The lung is a serous membrane covered by a double-walled sac called the pleura. The pleural cavity is a fluid-filled region between the visceral and parietal pleura (Figure 6). The visceral pleura is an elastic membrane which contracts and expands relative to the parietal pleura [64, 103]. Hereby, the intrapleural fluid lubricates the movement of the elastic visceral pleura. The intrapleural fluid can be seen as a mechanical link between the forces generated within the thorax and abdomen and the rib cage which again transmits the forces to the spine.

The biological tissue of the visceral pleura contributes greatly to the recoil force and the volume limitation of the lung. It contains a large amount of collagen and elastic fibre networks which are both intermingled. While the interwoven collagen networks limit the dilatation of the lung, the elastic fibres provide the recoil force to restore the collagenous mesh to the lungs resting position [103]. A study reported that the elastic fibres increase in size and content during adolescence, but remain unchanged when growth maturity is

reached [195]. This might be correlated to the increase in size and weight of the body during growth until skeletal maturity is attained.
Alterations in the distribution of both collagen fibre types are associated with illnesses such as bullous pleura disease and pulmonary emphysema.

The amount of fluid within the pleural cavity also plays a decisive role in the mechanics of the lung, while the thickness of the interpleural space correlates with the intrapleural pressure (IPP) [3, 5]. In general, interpleural thickness values in mammals were measured within the range of 0.005mm and 0.8 mm [3–5, 178]. Studies on dogs, rabbits and mice revealed that the IPP magnitude increases exponentially with a reduction of interpleural thickness, while the IPP becomes zero at an interpleural thickness of about 1.2 mm [3].
In humans, a similar correlation between IPP and the amount of fluid in the interpleural space can be measured while performing pleural manometry during thoracentesis [42].

Anatomically, the interpleural spaces of the right and left lungs are separated. To what degree the intrapleural pressures between the left and right side interact is unclear to date. Simultaneous measurements of the IPP at the right and left lungs in dogs during acceleration revealed that the pressure can vary significantly, while the local IPP depends on gravitational forces and posture [149, 191]. The authors found that the displacement of the heart during acceleration correlated with the IPP distribution [149]. Simultaneous measurements of the left and right sides indicate that the pressure on the left hemithorax may be more negative than on the right hemithorax [35].
Also, since the organs within the thorax and abdomen in humans are not symmetrically positioned with respect to the sagittal plane, a general asymmetry in the IPP can be assumed.

Summary of the load bearing principal

The weight within the peritoneum in an upright posture is most likely transmitted through the diaphragm in two ways (Figure 6c): firstly, via the diaphragm and the pleura to the chest walls bilaterally, and secondly, through the central tendon and pericardium to the sternum. To model this load distribution, the load could simply split up into three

components: intrapleural pressure on the right and left sides across the inner surface of the hemithorax, and a third component acting on the sternum.

1.4 Spinal deformation: scoliosis

Scoliosis is a spinal deformity which exhibits changes of the shape of the bone during adolescence. To understand the mechanisms which lead to the altered bone morphology, the pathology and aetiology of scoliosis are briefly described in following sections.

1.4.1 Pathology and treatment

Scoliosis is a three-dimensional deformity of the spine. A slight deformity of the spine can be observed in almost every individual [93]. The prevalence of AIS is 0.47-5.2%, generally defined once an angle of the main spinal curvature (Cobb-angle) of >10° is observed [114].

Scoliosis may have different ages of onset. It is commonly classified based on the age it is diagnosed:

- <3 years: Infantile (congenital) scoliosis;
- 3-9 years: Juvenile scoliosis;
- 10-18 years: Adolescent scoliosis;
- >18 years: Adult / Degenerative scoliosis

Infantile and juvenile scoliosis share many characteristics and are commonly grouped under the name of early onset scoliosis to distinguish them from the most common “adolescent” type. Adult scoliosis can be classified as degenerative or “de novo” scoliosis, which appears in the adult due to degenerative changes in the spine. Almost every second person above 60 years develops the “degenerative scoliosis” type [28, 158].

The spinal deformity goes hand in hand with several other factors such as deformation of the chest, reduction in lung capacity, modification of the soft-tissue, changes in the muscle architecture, as well as, asymmetrical shoulder and head balance. These factors can lead to disabilities, cosmetic issues, pain, activity limitation, quality of life issues and breathing problems. In addition, possible health issues into and throughout adulthood remain, such as, increased risk of disc degeneration and curve progression.

Initial treatment of patients with AIS involves physical therapy and bracing. Surgery is generally recommended when conservative treatment fails, the curvature progresses and a Cobb-angle greater than 40° is reached. During this very invasive surgery, the curved spine is first mobilized by resecting soft tissue (e.g. facet joints, intervertebral discs), then straightened using manual force, and finally stabilized with screws and rods.

1.4.2 Aetiology hypothesis for AIS

In approximately 85% of scoliotic cases in adolescence, a causative factor has not yet been identified [91].
AIS occurs more often in girls (7 girls to 1 boy) and the incidence of scoliosis within the family is increased [58]. Genetics, however, indicate a predisposition but do not explain the cause for the development of this spinal deformation.

According from the data from literature, four different mechanisms could potentially cause a spinal deformity, as illustrated in Figure 7:

a. A pre-existing initial asymmetry in the shape and material properties of the mechanical construct. This asymmetry then increases once the construct is mechanically loaded;
b. Disorder of the passive (connective tissue) and/or active (muscles) supporting structures for an erect spine;
c. An asymmetric growth in bone leading to deformity of the spine;
d. Intrinsic loads, such as an asymmetrical weight distribution that deform the construct.

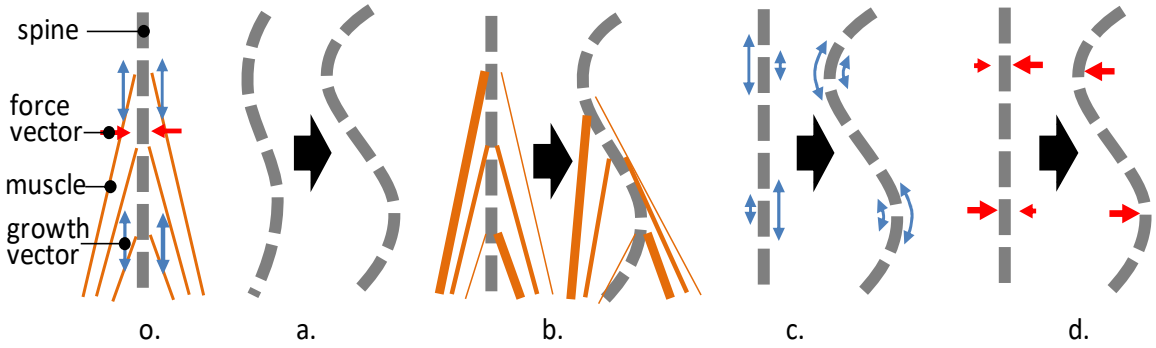


Figure 7: Sketch of aetiology theories for the development of adolescent idiopathic scoliosis. ***o.*** *Healthy stable erect growing spine.* ***a.-d.*** *Theoretical mechanisms that might lead to a spinal deformity: an initial spinal asymmetry increases over time (a.), supporting structures (orange) which are necessary for the stability of the erect spine are disturbed (b.), asymmetrical growth of the bone (c.), and/or asymmetrical forces deform spine (d.)*

The published hypothesis on the aetiology of AIS can be grouped according to these four aspects. One of the main challenges is to identify which factor is primary or secondary to the formation of scoliosis.

a. Pre-existing deformation

This theory proposes that the spine inherits a pre-existing deformation, e.g. at birth, which increases over time.

On average, a pre-existing vertebral rotation is present in every human and quadruped [80, 81, 94]. Yet, only 0.5%-5% of the population develop a pathological deformation of the spine during adolescence [155]. How strong an initial deformity needs to be pronounced to become unstable and to progress is unknown.

Children and adolescents with curve angles of 5° to 19° have a probability of curve progression of 22%, and curve angles between 20° to 29° a probability of 68% [113]. Curves angles < 30° after growth maturity will most likely not progress.

A predisposition to a strong spinal deformation can exist, which is referred to as congenital scoliosis. Congenital scoliosis includes anomalies during embryonic formation, such as fusion of vertebral segments and/or ribs, or local disturbances of the growth plate which lead to malformation of vertebrae, called hemivertebra. These malformations can be considered as a disturbance in the statics of the spinal construct. This can cause a deformation of the entire spine which usually worsens with growth. The shape of the spinal deformation depends on the structure of the anomaly in which the child may

exhibit a scoliotic curvature to the right or left, kyphosis, and/or a lordosis. Currently there is no evidence that this condition can be inherited.
Patients with AIS do not show any congenital abnormalities. AIS is usually diagnosed before Cobb-angles above 20° are obtained. Currently, curve progression is not possible to predict.

In summary, clinical data has not presented any evidence that a pre-existing curvature could cause AIS.

b. Disorder of the supporting structures of the spine

Many structural components interact to provide a stable erect posture of the spine. This interaction consists of intervertebral disc, bone and ligaments, muscles and gravity.
Disorders in the connective tissue can cause scoliosis, such as a reduced bone mineral density (osteopenia), as well as be part of syndromes such as Marfan, Ehlers-Danlos, Osteogenesis Imperfecta syndrome. In patients with AIS, alterations were observed in the extracellular matrix of the connective tissue, such as the collagen composition within the disc, and the elastic fibres [18, 196]. This is most likely secondary to scoliosis.
The Euler Stability theory is also often referred to when explaining spinal deformations. This theory describes the amount of maximal load a long ideal straight column can carry without buckling. In the *in vitro* experiments on cadaveric human spinal specimens, devoid of muscles and ribs, it was measured that the spine buckles at a load of 20 N to 80 N [36], whereas the buckling-load depended on the length of the spine. In comparison, it is assumed that an axial load of more than 500 N acts on the lumbar spine *in vivo* [144, 184]. To compensate this almost 10-fold axial load which indicates potential instability, the spine needs to be stabilised using muscles.
Reduced strength and activity of the supporting musculature of the spine may indeed lead to scoliosis as part of neuromuscular disorders such as in muscular dystrophy [194]. Furthermore, disorders were observed including those with neurological deficit, abnormalities in the contractile apparatus [89][147], as well as differences in the ratio of muscle fibre type I/II (slow/fast twitch) between the convex and the concave side of the spinal curve [121]. Curve patterns in patients with scoliosis secondary to neuromuscular diseases also appeared comparable to those patterns in patients with AIS [95]. A

weakness of the muscles may be a possible nonspecific trigger for the development of scoliosis.

Whether a disorder of the supporting structures is the primary cause of scoliosis is questionable. Firstly, the mentioned Euler stability theory is not directly comparable to the spinal deformation, particularly since the spinal shape is not ideally straight and the stiffness of the spine is not homogeneous along its length. In addition, muscles inherit a great ability to adapt to loading conditions which could explain the differences in the muscle activity between concave and convex sides. Also, neither general physical therapy [131] nor scoliotic specific exercise [145] have been proven to reduce the curve or stop curve progression. Current literature provides weak evidence that anthropometric data, such as body weight and spinal length, and neuromuscular disorders, such as a decrease trunk muscle strength, are associated with AIS [155].

In summary, the question whether the stability of the passive or active structures is a primary or secondary cause for AIS remains a matter of debate. Evidence indicates it is most likely secondary.

c. Asymmetrical growth

Morphological studies revealed a disproportional growth between the anterior and posterior spinal column [63, 143]. This led to the theory that either an abnormal growth of the anterior column, or a tethering of the spinal canal might inhibit the growth of the posterior column [142, 143].

Furthermore, a decreased melatonin level in AIS patients has been measured [117]. Scoliosis can also be part of the Noonan Syndrome in which the growth regulation is disturbed.

As described in chapter 2.1, the vertebral growth originates via endochondral ossification of the epiphyseal growth plates on superior and inferior endplates. Although a different growth kinetic between convex and concave side of the spine has been measured within patients with AIS [179], there is no evidence that AIS is caused by a primary growth disturbance [24].

The explanation of the observed asymmetrical morphology is rather provided by the Hueter-Volkmann Principal [167]. This law states that bone is formed by compression and

distraction forces to which bone is exposed. Animal studies have demonstrated that asymmetrical loading can lead to bone formations comparable to AIS [123, 129, 169].

In summary, morphological variations are most likely caused by adaption to altered loading rather than to a primary growth disturbance.

d. Intrinsic load distribution

The *in-vivo* load distribution along the scoliotic, as well as the healthy spine, is fairly unknown.

Other than an axial load component, a lateral load component originating from the ribs potentially acts on the thoracic spine. The ribs transmit muscle forces of the sternum and rib cage to the spine. Extensive animal studies on the influence of rib resections on the spine identified that only unilateral resections of the posterior ends of 5 to 6 adjacent ribs resulted in a progressive scoliosis [101, 102, 124]. It is also known that children with thoracotomies, particularly in the posterior region above the 6^{th} rib level, are of higher risk to develop scoliosis [39, 52, 60, 85].

However, patients with AIS usually have no history of surgical interventions performed on the rib cage. Additionally, weak evidence of an increased chest asymmetry within patients with AIS exists.

The treatment of spinal deformations with a brace to which distinct load points are applied on the chest wall can lead to a momentary straightening of the spinal curvature. Evidence that the brace treatment can prevent curve progression is yet lacking [130].

It can be assumed that intrinsic forces indeed trigger the spinal deformation, although the underlying mechanisms remains unclear.

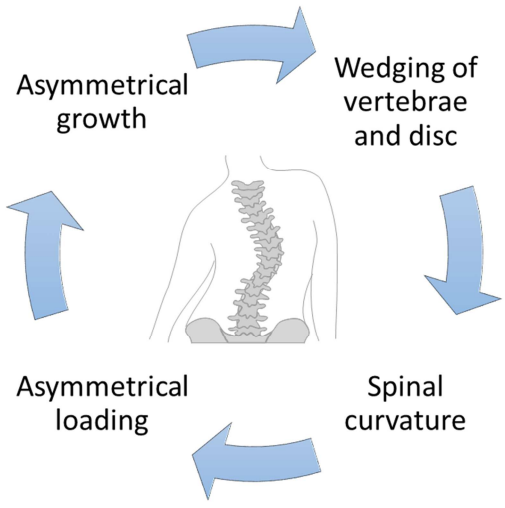


Figure 8: Vicious cycle on the development of scoliotic curvature, proposed by Stokes et al. [169]. *Small disturbances activate that circle which leads to an increase of the curvature over time.*

The common conclusion of literature reviews on the pathogenesis of scoliosis is that the

mechanics triggering scoliosis are complex and its aetiology is most likely multifactorial [67, 91, 114, 181]. This multifactorial process was illustrated as a vicious cycle by Stokes et al. [169] (Figure 8). However, the causal mechanisms as well as the constellation of the components which lead to scoliosis are not yet understood [155]. In general, the spinal disorder classified as “idiopathic” is not homogenous. This leaves the possibility that different causative factors might explain the aetiology of AIS.

1.5 Aim of this thesis

The objective of this thesis was, firstly the development of a fully parametric numerical model of the spine including the rib cage to perform biomechanical simulations. Secondly, the bone morphology of healthy and scoliotic individuals was quantified to obtain morphology parameters for the model generation. This data was further analysed to identify morphological patterns within scoliotic spines.

With this model, the development of scoliosis was investigated with emphasis on the potential influence of an asymmetry in the intrapleural pressure distribution on the spinal deformation.

2. Material and Methods

The determination of the *in vivo* mechanics of biological living tissue is very challenging, since the structures involved in the mechanics are highly complex and difficult to measure. In addition, these naturally inherit a high standard deviation within and in-between subjects. To approximate the *in vivo* condition, multiple data sets can be obtained from either *in vivo* or *in vitro* measurements. A strong potential of numerical methods is that all these data sets can be pieced together into one model as in a puzzle. This allows the testing of hypothesis, estimating predictions and approximating the *in vivo* condition.

Within this thesis, a finite element model was created which aimed to represent the biomechanical condition of the chest and spine. The model was intended to approximate the biomechanical condition within individual patients. The steps from the images of an individual patient to the complete FE-model are illustrated in Figure 9.

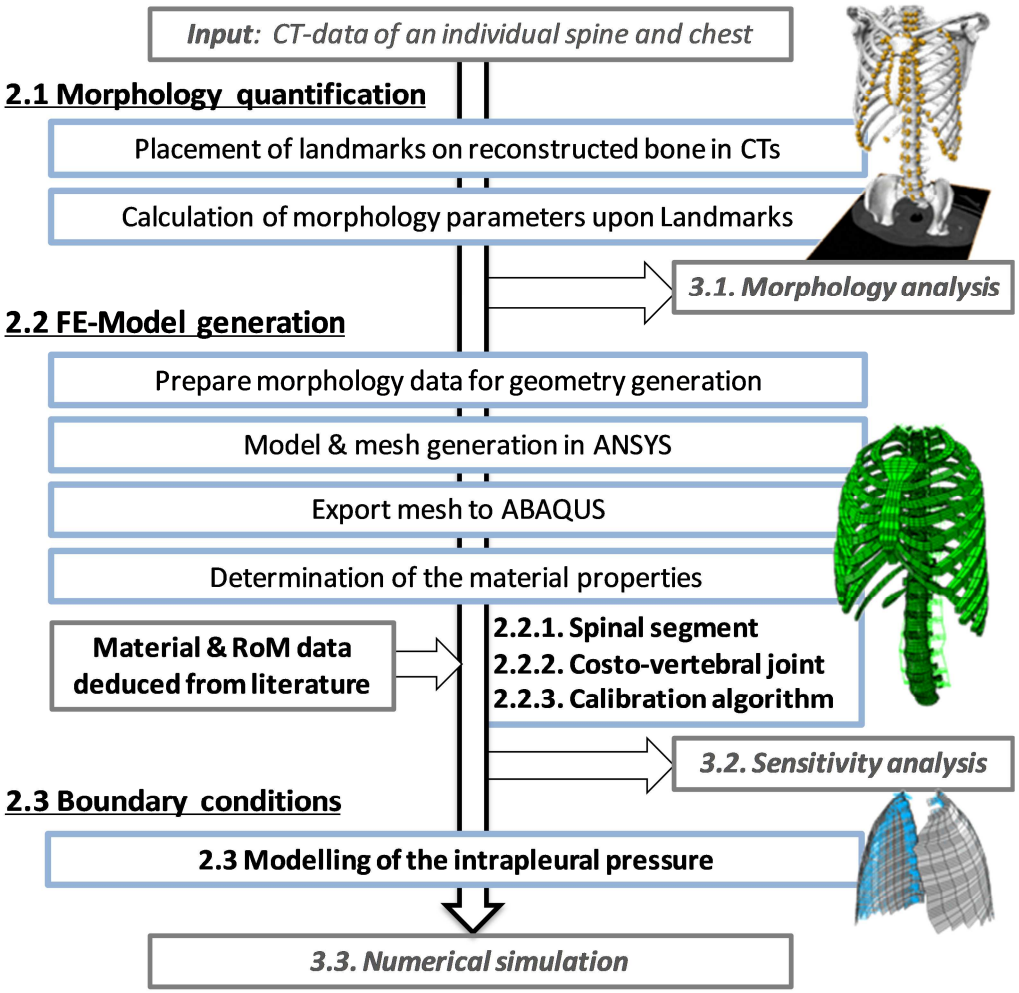


Figure 9: Basic schema for generating a numerical model of an individual human spine and chest.

To generate a biomechanical model of an individual, two main aspects must be considered: the morphology/geometry and the material properties of the soft and hard tissues. Both aspects are nearly impossible to represent in a personalized model, particularly since most of the data cannot be directly obtained from neither *in vivo* nor from *in vitro* measurements. Extracting mean material property values from the literature does not necessarily result in a biomechanically correct representation of the individual spinal motion segment.

These issues were dealt with by generating a model in which the morphology and material properties were defined using a set of parameters. The variation of these parameters allows, firstly, a quick adaption of the model to simulate, for example, different types of scoliotic curvatures. Secondly, it enables the estimation of sensitivity of a chosen parameter set towards the obtained results.

The following chapter describes the general acquisition of the morphology and material parameters, as well as the background and generation of the numerical model of the spine, chest and boundary conditions.

2.1 Morphology quantification

The morphology of the spine and chest was quantified by placing landmarks on reconstructed bone from CT-data of patients.

2.1.1 Patient group

Morphology parameters of the spine were obtained retrospectively by evaluating collected computed tomography (CT) images of 21 patients diagnosed with AIS (AIS group) and 48 patients without any visible spinal abnormalities (healthy group) (ethical votes: 418/15-Zo/Sta in 2016, and B-F-2016-053 in 2016). The mean age was 15 ± 2 years for the AIS group and 23 ± 12 years for the healthy group. Inclusion criteria for the CT data were a visibility of the spinal levels T1 to S1, including the entire chest. In addition, the slice thickness of the CT-data was <1 mm and the in-slice resolution 0.91 mm, resulting in a voxel size of 0.91 mm × 0.91 mm × 1 mm.

The AIS cases were subdivided into the three groups depending on the location of the main curvature: lumbar (n = 5), thoracic (n = 12), and thoracolumbar (n = 4). This allowed for a better comparison of the data and identification of morphology patterns. (*see* [151])

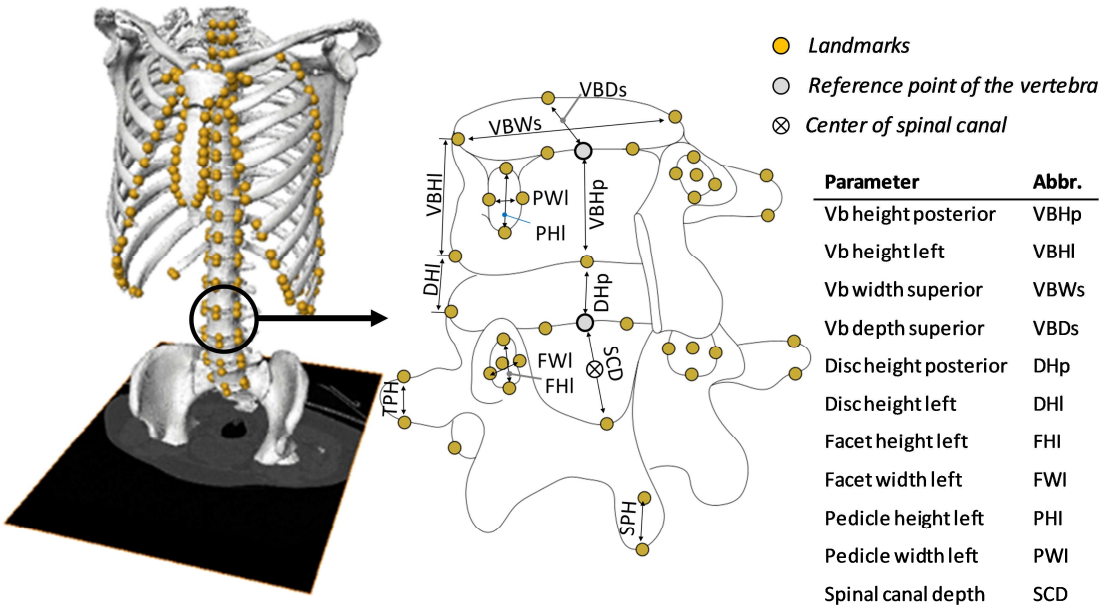


Figure 10: Landmarks that were placed on the reconstructed spine and chest. Right: List of exemplary parameters of a vertebral segment. Abbr.: Abbreviation, Vb: vertebral body. [151]. [Reprinted with permission from Springer Nature]

2.1.2 Landmark placement

The skeletal structure was reconstructed from CT data using the software tool AVIZO (release: 8.0; FEI Visualization Sciences Group, Hillsboro, Oregon, USA). Landmarks were placed manually on predefined characteristic morphological points on the spine and chest. The location of the main landmarks on a vertebra was comparable with those of previous studies [11, 109].

2.1.3 Morphology parameters

Morphological parameters were derived from the coordinates of those landmarks.

More than 300 parameters were calculated from the landmarks: 62 global parameters (e.g. position of the vertebrae relative to S1), about 100 for each vertebral level (e.g. vertebral body width), and 125 parameters for the rib cage (e.g. width of a rib).

The focused was placed on the analysis on the overall dimensions of the spine, the shape of the vertebrae and discs, as well as the cross-sectional area of pedicles and the articular facet joint surface area. In addition, other global morphology parameters of the rib cage, such as the lateral position of the posterior section of each rib, were quantified.

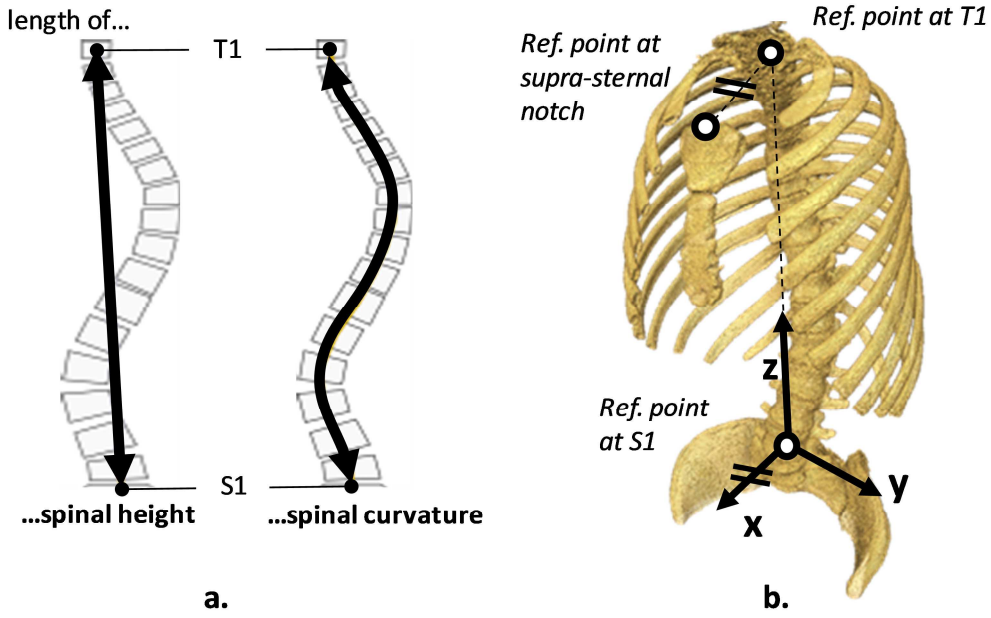


*Figure 11: **a**. Sketch of the specified "spinal height" and "spinal curvature". **b.** Orientation of the global coordinate system of each patient. The z-axis points from the middle of the posterior edge of the superior endplate of S1 to T1, while the sagittal plane was defined by the vector between T1 and the centre of the suprasternal notch. Ref.: Reference [151]; [Reprinted with permission from Springer Nature]*

An average endplate size for each spine was calculated by summarizing the endplate area at each vertebral level (i) for all levels (m) (sup: superior, inf: inferior).

$$\bar{A} = \frac{1}{m}\sum_{i=1}^{m}\frac{A_{i,\text{sup}} + A_{i,\text{inf}}}{2}$$

The endplate area was assumed to have an elliptical shape.

To investigate potential length differences between the anterior and posterior spinal column, the length of the spinal canal was quantified by connecting the centre of the spinal canal at each vertebral level. The centre of the spinal canal was positioned in midline: between the posterior tip of the canal on the lamina and the point on the posterior edge of the superior endplate (Figure 10).

Furthermore, the individual length of the spinal curvature and height of the spine was calculated (Figure 11a). Each length was calculated in three-dimensional space: "spinal height" between middle of the superior endplates of T1 and S1, and the "spinal curvature" by connecting the midpoint of the superior endplate of each vertebra.

A patient-specific coordinate system was created using three landmarks to reduce parameter variations in-between individuals (Figure 11b).

Spinal parameters, such as the displacement in the coronal plane and rotation of the vertebrae, were calculated relative to the superior endplate of S1. (*see* [151])

2.1.4 Statistical analysis

The intra- and inter observer variability for the placement of the landmarks was analysed by two observers who repeated the placement of the landmarks six times on a non-scoliotic and a scoliotic spine. The variability of placing landmarks was quantified by analysing the variance of the deduced morphology parameters. The coefficient of variation was calculated for each parameter at each level. An average coefficient of variation was estimated by calculating the mean value of the coefficient of variation over all levels. This enabled the measurement of the dispersion of a parameter value due to individual observers. Furthermore, a Bland–Altman plot was generated for specific parameters to visualize and analyse the variance between the two observers.

The results of the healthy group were statistically analysed using a two-sided one sample *t*-test by comparing the values to an expected true mean.

To identify significant differences between the healthy and scoliotic spines, the mean values at each level were compared using the *t*-test for unpaired data. A significance level of 0.01 was considered. The statistical analysis was performed using the SciPy package (version 0.16.0) with Python (version 3.4.3) [135]. (*see* [151])

2.2 **Finite element model of the chest and spine**

A full parametric finite element (FE) model of the anatomy and material properties of the thoracic and lumbar spine, including the rib cage, was developed. The model generator is based on the methodology published by Niemeyer et al. [133], in which morphology parameters were used to generate the geometry of the spine using geometric primitives. The basic principal of this method was adopted, yet modifications in the code structure, the overall geometry, as well as further extensions were included, such as the

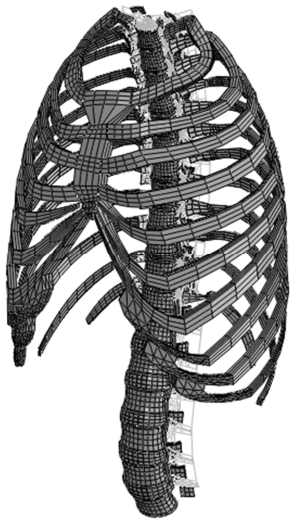


Figure 12: Examplary finite element model of a 13-year-old male obtained using the FE-model generator. This model was used for this study. [Reprinted with permission from Springer Nature]

entire rib cage. Although the muscles of the spine were also implemented, their model generation and calibration are beyond the scope of this thesis and, therefore, omitted here. According to the model-scheme illustrated in Figure 9, the model was generated from a parameter database. This database included morphology and material parameters. The morphology parameters were imported into an in-house code which automatically generated a finite element model of the spine and chest. The model also included the disc, the surrounding ligaments and boundary conditions. The model generation was implemented in APDL using ANSYS (Release 15.0, Ansys Inc., Canonsburg, PA, USA). The meshed model was then exported into ABAQUS (Release 6.12, SIMULIA Dassault Systems, Johnston, RI, USA), where the simulations were performed.

In this thesis, the model generation was demonstrated on one particular patient: a 13-year-old male who did not showed any signs of abnormal spinal deformities. The geometry of the model was generated from computed tomography data of that particular patient in the supine position.

Since the RoM of a vertebral segment and the CVJ vary along the spine, their material properties also differ. The RoM distribution of the vertebral segments [185, 187] and costovertebral joints [104] was extracted from literature.

The main joints that contribute to the biomechanical behaviour of the thorax include the spinal segments and the costovertebral joints. Their kinematics are determined by the material properties of the soft tissue and the morphology. The material properties can vary within subjects and between vertebral levels, leading to a wide possible range of motion of a spinal segment and CVJ. To identify the influence of the material properties and the morphology parameters on the RoM, a sensitivity analysis was performed on both a spinal segment and costovertebral joints. Subsequently, a method was developed to estimate the material properties based on a given RoM and the morphology of the joints.

2.2.1 Spinal segment

The numerical model of the spine as described here is based one spinal segment, which represents the smallest functional unit of a spine. It involves an intervertebral disc between two adjacent vertebral bodies.

In order to capture the variability of the spine morphology within and in-between subjects, the geometry of the spine was constructed numerically using geometric primitives. This led to a strong simplification of the spinal geometry, yet allowed for a rapid and robust generation of subject-specific models that considered the individual spine morphology and shape.

2.2.1.1 Numerical model

The cortical bone, the cancellous bone and cartilage endplates of the vertebral bodies were formulated using eight-node isoparametric solid elements, as listed in Table 2. The posterior structures were constructed as a framework of beam elements. The motivation behind the selection of a beam framework for the posterior structures was, firstly, the challenge of replicating the geometry of the posterior structures using the parametric approach. Secondly, the framework facilitated the inclusion of various muscle and ligament attachment points on the posterior structures.

The annulus ground substance was modelled using 8-node brick elements. Rebar elements were embedded in the mid-plane of the annulus ground substance using membrane elements to model the collagen fibre network. The nucleus was represented as a fluid cavity in which hydrostatic conditions were present.

2.2.1.2 Material model

The material properties which have potentially have a strong influence on the RoM of the spinal segment were identified and parameterized.

The following material properties were parameterized: the annulus fibrosus, the anterior longitudinal ligament (ALL), the posterior longitudinal ligament (PLL), the capsular ligament (CL), the flaval ligament (FL), intraspinous ligament (ISL) and the supraspinous ligament (SSL). In addition, the size of the gap between the respective inferior and superior articular areas of the facet joints was varied. The facet gap is difficult to deduce from radiographs and CT scans, adding a further unknown. Since the stiffness of bone is much higher than that of the annulus fibrosus and the ligaments, the influence of a variation in bone properties on the overall flexibility was assumed to be negligible.

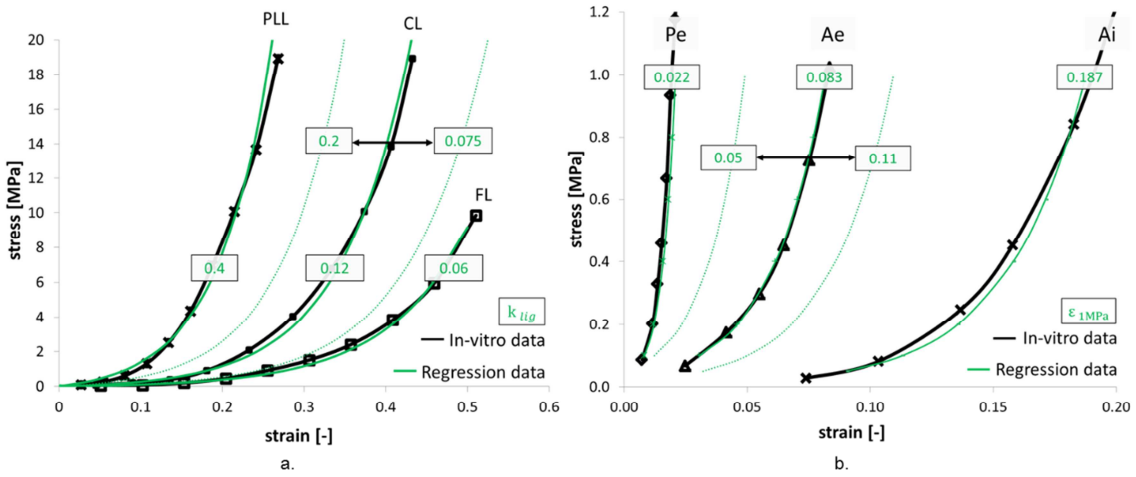


Figure 13: Exemplary comparisons of the in vitro data with the calculated stress-strain relationship using the parametric regression equations. ***a****. Parametrised ligament behaviour, with the in vitro data from Pingel et al. [140].* ***b.*** *Annulus fibrosus fibre behaviour, with in vitro data from Holzapfel et al. [74]; Pe: posterior external, Ae/i: anterior external/internal part of the annulus fibrosus ring. [152] [Reprinted with permission from Taylor & Francis]*

In the FE model, the ligaments were represented by membrane elements with embedded rebar properties. The rebar behaviour was parameterized using a functional relationship between stress (σ) and strain (ε):

$$\sigma(\varepsilon)_{\text{lig}} = k_{\text{lig}} \cdot \exp\left(k_{\text{lig},2} \cdot \varepsilon\right) - k_{\text{lig}} \,, \qquad \textit{(Eq. 1)}$$

where k_{lig} determines the overall stiffness and the derived quantity

$$k_{\text{lig},2} = 2.62 \cdot \ln\left(k_{\text{lig}}\right) + 17.44 \qquad \textit{(Eq. 2)}$$

The parameter (k_{lig}) allows the adaption of the ligament properties to the *in vitro* data published by Pingel [140] (Figure 13a). The constant coefficients in the equations (Eq. 2) where obtained by regression analysis of the *in vitro* data.

In addition to the nonlinear stress-strain relationship, the cross-sectional area of the ligaments was varied. The annulus fibrosus was modelled by embedding the collagen fibres as rebar elements by superimposing membrane elements, which were again embedded in continuum solid brick elements. This allowed for the consideration of a non-linear behaviour of the collagen fibres, a non-uniform fibre distribution, as well as, the variation of the fibre orientation in all three axial directions. The collagen fibre property was varied in circumferential and in radial direction, since the stiffness of the annulus fibrosus decreases towards the nucleus pulposus [23].

Table 2: Material properties and numerical model of the tissues used in the finite element model. SSL: supraspinal lig., ISL: interspinal lig., FL: flaval lig., CL: capsular lig., PLL: posterior longitudinal lig., ALL: anterior longitudinal lig., ACC: articulatio capitis costae, ACT: articulatio costotransversalis, LCTS: lig. costotransversarium superius, LCT: Lig. costotransversarium

Structure	Numerical model	Properties						Source
Cortical bone	Solid 8-node brick element	Young's modulus in MPa		Shear modulus in MPa		Poisson's ratio		[10]
		E_{xx}	11300	G_{xy}	3800	ν_{xy}	0.48	
		E_{yy}	11300	G_{yz}	5400	ν_{yz}	0.20	
		E_{zz}	22000	G_{xz}	5400	ν_{xz}	0.20	
Cancellous bone	Solid 8-node brick element	Young's modulus in MPa		Shear modulus in MPa		Poisson's ratio		[87]
		E_{xx}	140	G_{xy}	48.3	ν_{xy}	0.45	
		E_{yy}	140	G_{yz}	48.3	ν_{yz}	0.32	
		E_{zz}	200	G_{xz}	48.3	ν_{xz}	0.32	
Cartilage	Solid 8-node brick element	Young's Modulus $E = 26$ MPa, Poisson's ratio $\nu = 0.4$						[172]
Nucleus	Fluid cavity.	Bulk modulus $K = 2200$ MPa						[1]
Annulus ground substance	8-node brick elements.	Neo-Hookean: $C_{10} = 0.348$ MPa, $D_1 = 0.3$						[65, 193]
Annulus collagen fibres	Rebar elements embedded in the mid-plane of the annulus ground substance.	Empirical relationship between the strain at 1 MPa (ε_{1MPa}) and the stress (σ) (Eq. 3)						[74]
Ligaments: SLL, ISL, FL, CL, PLL, ALL	Rebar elements embedded in membrane-elements.	Empirical relationship between strain (ε) and stress (σ) (Eq. 1)						[140]

The fibre material properties were parameterized by an empirical stress-strain relationship:

$$\varepsilon(\sigma)_{\text{annulus}} = k_{A,1} + k_{A,2} \cdot \ln(\sigma/\sigma_0) \quad \textit{(Eq. 3)}$$

$$\text{with } k_{A,1} = \varepsilon^{1MPa}$$

$$\text{and } k_{A,2} = 0.053 + 0.013 \cdot \ln(\varepsilon^{1MPa}) \quad \textit{(Eq. 4)}$$

where ε^{1MPa} refers to the strain at 1 MPa (Figure 13 b), and $\sigma_0 = 1\ [MPa]$. The constant coefficients in the equation (Eq. 4) were determined by fitting the equation to the data published by Holzapfel [74].

The properties of the annulus fibrosus were also varied in circumferential direction for each sector $i_{\text{sec}} \in \{1,2,\dots,6\}$ (ant. – post.) according to

$$\varepsilon_{ext,i_{sec}}^{1\text{MPa}} = \varepsilon_{ext,\ ant}^{1\text{MPa}} + \left(\varepsilon_{ext,\text{post}}^{1\text{MPa}} - \varepsilon_{ext,\text{ant}}^{1\text{MPa}}\right) \cdot ((i_{sec} - 1)/5)^{k_A} \quad \textit{(Eq. 5)}$$

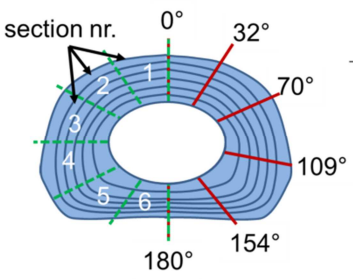
To vary the properties in radial direction, a factor ($k_{A,int}$) was introduced which varied the strain in the inner ring ($\varepsilon_{1MPa_{int,i_{sec}}}$) relative to the strain in the outer ring ($\varepsilon_{1\text{MPa}_{ext,i_{sec}}}$) at each section ($i_{sec}$).

$$\varepsilon_{int,i_{\text{sec}}}^{1\text{MPa}} = \varepsilon_{ext,i_{\text{sec}}}^{1\text{MPa}} \cdot k_{A,\text{int}} \quad \textit{(Eq. 6)}$$

The collagen fibre angle was varied along the circumferential direction of the annulus by interpolating between the fibre angle at the anterior section ($\alpha_{A,\text{ant}}, i_{\text{sec}} = 1$) and the posterior section ($\alpha_{A,\text{post}}, i_{\text{sec}} = 6$) (Figure 14):

$$\alpha_{A,i_{\text{sec}}} = \alpha_{A,\text{ ant}} + \left(\alpha_{A,\text{post}} - \alpha_{A,\text{ ant}}\right) \cdot ((i_{sec} - 1)/5)^{k_{\text{angle}}} \quad \textit{(Eq. 7)}$$

where i_{sec} is the section number of the annulus and k_{angle} an exponent controlling the amount of non-linearity in the spatial distribution of the fibre angles. The fibre angles were not varied in the radial direction, since Eberlein [49] did not find any significant dependency between fibre angle and depth.



Polar-angle	Fibre-angle	
	min-SD	max-SD
0°	18.6°	27.4°
32°	22.6°	25.4°
70°	20.9°	26.5°
109°	32.2°	51.4°
154°	36°	52°
180°	55.1°	59.5°

Figure 14: Standard deviation (SD) of the collagen fibre angle in the annulus fibrosus in circumferential direction. The annulus fibrosus was divided into six sections, defined by the polar angle. Values were extracted from Eberlein et al. [49]. [152] [Reprinted with permission from Taylor & Francis]

The material properties were extracted from the literature and varied within the specified standard deviations (Table 3). The nucleus was represented as a hydrostatic fluid cavity. An exponential pressure-overclosure contact condition was chosen to model the contact behaviour of the articular surfaces of the facet joints, with a clearance of 0.4, a contact pressure of 170 [MPa] at zero clearance and a friction coefficient of 0.001 [133]. (*see* [152])

Table 3: List of the investigated parameters, including their ranges, as well as the resection steps affecting the corresponding structures. [152]

Resectstep	**Resected structure**	**Investigated structure**	**Investigated parameter range**	**Source**
0	- (Intact)	SSL	area_{SSL}: 1 – 100 mm^2; $k_{\text{lig}} = 0.1 - 0.4$ [MPa]	[30, 140, 141, 161, 197]
1	SSL	ISL	area_{ISL}: 1 – 100 mm^2; $k_{\text{lig}} = 0.15 - 0.6$ [MPa]	
2	ISL	FL	area_{FL}: 50 – 300 mm^2; $k_{\text{lig}} = 0.03 - 0.12$ [MPa]	
3	FL	CL	area_{CL}: 1 – 10 mm^2; $k_{\text{lig}} = 0.075 - 0.2$ [MPa]	
4	CL	Facet gap	0.5 – 5 mm	
5	VA	PLL	area_{PLL}: 10 – 100 mm^2; $k_{\text{lig}} = 0.3 - 0.5$ [MPa]	
6	PLL	ALL	area_{ALL}: 10 – 100 mm^2; $k_{\text{lig}} = 0.2 - 0.4$ [MPa]	
7	ALL	Annulus embedded rebar properties. Parameters of the functional relationship (Eq. 3) anterior outer ring: $\varepsilon_{1\text{MPa}_{\text{ext, ant}}}$: 0.05 – 0.11 [−] posterior outer ring: $\varepsilon_{1\text{MPa}_{\text{ext, post}}}$: 0.01 – 0.05 [−] distribution: $k_{A,\text{ext}}$: 1 (linear) – 4 (quartic) Annulus strain at 1 MPa of inner ring: $k_{A,\text{int}}$: 3 – 4	[49, 74]
		Annulus collagen fibre angle. Parameters of the functional relationship (Eq. 8). fibre angle: anterior: $\alpha_{A,\text{ant}}$: 16° - 31° posterior: $\alpha_{A,\text{post}}$: 41° - 60° distribution: k_{angle}: 1 (linear) – 4 (quartic)	

2.2.1.3 Simulation procedure

A total of 500 different models were generated, each based on a unique parameter combination. The parameters were varied within specified ranges which corresponded to the mean standard deviation (+/-SD) of published experimental data (Table 3). All parameters were sampled together using the uniform latin-hypercube sampling method (with pyDOE 0.3.6). The intact condition and all seven resection steps were simulated for each parameter combination which led to a total of 4000 simulations. In accordance with the *in vitro* experiments of Heuer [71], pure moments of 7.5 Nm were applied for each simulation in flexion, extension, lateral bending and axial rotation. Prior to applying the pure moments, a hydrostatic pressure of 0.1 MPa was applied to the nucleus pulposus.
The inferior endplate of the caudal vertebra (L5) was fixed. The loads were applied on a node rigidly connected to the superior endplate of the cranial vertebra (L4). (*see* [152])

2.2.2 Costovertebral joint (CVJ)

The main structure which governs the motion of the rib cage, is the costovertebral joint. Therefore, the focus was placed on modelling its mechanical behaviour which included the load transmission to the adjacent vertebral bodies.

2.2.2.1 Background on the CVJ

Within the CVJ, two synovial joints, the articulatio capitis costae (ACC) and the articulatio costotransversalis (ACT), connect the rib to the spine. At the spinal levels T1, T11 and T12 the ACC is typically attached to one vertebral body only, while at T2-T10 the ribs articulate with an ACC that spans two adjacent vertebrae. The ACT, which is mainly pronounced at the levels T1-T10, connects a rib to the transverse process of the adjacent caudal vertebrae. The connection between rib and spine is also reinforced by cross-linked ligaments: the ligamentum costotransversarium (LCT), the ligamentum costotransversarium superior (LCTS), the ligamentum costotransversarium laterale (LCTL), the ligamentum capitis costae radiatum (LCCR) and the aforementioned ligamentum capitis costae intraarticulare (LCCI) (Figure 15). The LCTS connects the transverse process of the superior vertebra to the rib head on each thoracic level [78]. *(see [154])*

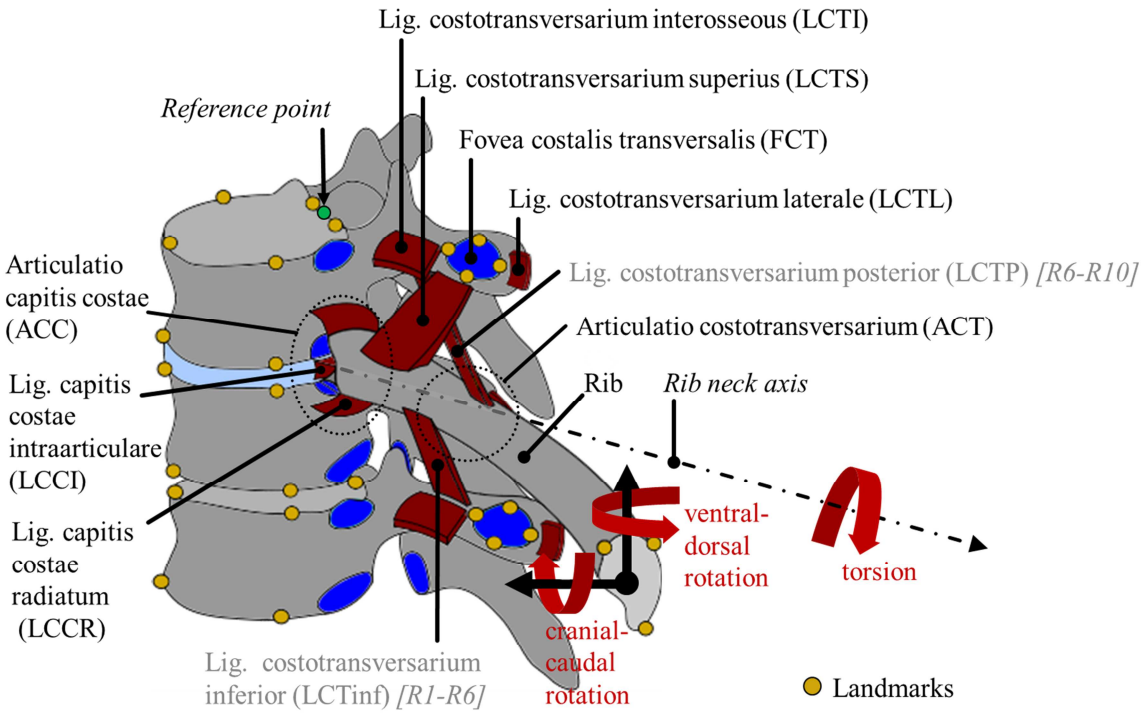


Figure 15: Coordinate system and load conditions of the CVJ. The orientation of the coordinate system reflects the orientation of the two joints: the x-axis points normal to the surface, while the y-axis points perpendicular to the surface. [154] *[Reprinted with permission from Taylor & Francis]*

2.2.2.2 Numerical model

An FE-model was developed which is fully parametric with respect to anatomy and material properties of the CVJ. A main goal was to accurately model the load transmission between the rib and the adjacent vertebrae. In accordance with the CVJ's anatomy, the model, therefore, included the load-paths between rib and adjacent vertebral bodies (via the ACC), between rib and transverse process (via the ACT), and between rib and the cranial vertebra (via the LCTS). Morphology and material parameters were imported into an in-house code, which automatically generated a finite element model of the spine. This included the rib cage and the surrounding ligaments, as well as the boundary conditions. The model generation was implemented in APDL using ANSYS (Release 15.0). The meshed model was then imported into ABAQUS (Dassault Systems, Release 6.12), where the simulations were performed.

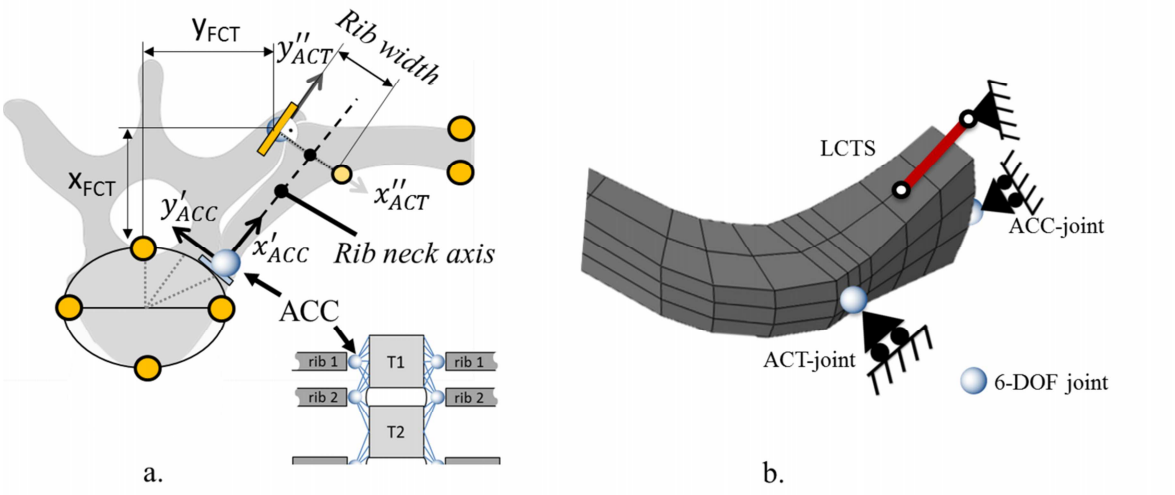


*Figure 16: **a**. Coordinate system and load conditions of the CVJ. **b.** Numerical model of the costovertebral joint including the boundary conditions. FCT: fovea costalis transversalis, ACC: articular capitis costae* [154]; *[Reprinted with permission from Taylor & Francis]*

The rib and joint geometry were simplified by using geometric primitives. The complex mechanics of the ACC and ACT joint with their capsular and surrounding ligaments were represented by connector elements (Figure 16). The ACC-connector element simulates the mechanics of the LCCR, LCCI, and synovial joint of the fovea costalis vertebralis, whereas the ACT-connector element represents the mechanics of the LCTL and the synovial joint of the fovea costalis transveralis. These connector elements allowed the assignment of nonlinear behaviour in six degrees of freedom. The motion perpendicular to the joint surface was restricted using connector-stop behaviour which represented a contact condition between rib and transverse process, as well as rib and vertebra.

The connector stiffness was parameterized using a quadratic force-displacement relationship (Eq. 8) in which a stiffness factor (k^{ACC}, k^{ACT}) was introduced to vary the mechanical behaviour of each connector in each degree of freedom according to the equation:

$$force = k_j^i \cdot displacement^2 \text{ with } i = \text{ACC, ACT and } j = x, y, z, rx, ry, rz \qquad \textit{(Eq. 8)}$$

The mechanical behaviour of the LCTS was represented using non-linear tension-only truss elements which connected the rib neck with the corresponding transverse processes. The nodes of the truss elements were attached to the rib surface by rigid connector beam elements. The body of the rib was modelled using 8-node linear brick elements. Although no study was found which measured the isolated properties of the

costo-vertebral ligaments, a quadratic stress-strain relationship, deduced from spinal ligaments, was assumed:

$$stress = k_{\mathrm{LCTS}} \cdot strain^2 \,, \qquad \textit{(Eq. 9)}$$

Since bone is much stiffer than the ligaments, its influence was assumed as negligible and, therefore, the bone properties kept constant. *(see [154])*

Table 4: List of the modelled tissue and their properties. The rib properties were extracted from Sham et al. [159]. [154]

Structure	Numerical model	Properties
Rib	8-node linear brick elements	Elastic modulus: 12000 [MPa] Poisson-ration: 0.35 [-]
ACC, ACT	Connector element: - Section: Cartesian, rotation	Non-linear connector stiffness (Eq. 8) Contact of the joint surface was modelled using connector stop behaviour: -0.5,100 (perpendicular to joint-surface: negative $\mathrm{x}'_{\mathrm{ACC}}/\mathrm{x}''_{\mathrm{ACT}}$ - direction)
Ligaments (LCTS)	2-node truss element	- Thickness: 10 mm - Non-linear behaviour (Eq. 9)

2.2.2.3 Simulation procedure

In total 2000 different models were generated, each based on a unique parameter combination. The material and morphology parameters were varied within a chosen range, as listed in Table 5, and sampled using the latin hypercube sampling method (using pyDOE 0.3.6). The morphology parameters were sampled as a group, in which each parameter combination corresponded to the morphology of one of the CVJs from the 39 patients. This led to 780 (20 CVJs per patient × 39 patients) possible morphology parameter combinations, in which the selection of the CVJ occurred randomly. Pure moments of 0.6 Nm were subsequently applied around all three anatomical axes: the torsion axis of the rib head (x'_{ACC}-axis), the caudal-cranial (z-axis) and dorsal-ventral (x-axis) axes (Figure 16). The intact condition and two material resection steps were simulated for each parameter combination. This resulted in 6000 parameter conditions. When five loads steps were included, a total of 30000 simulations were obtained. *(see [154])*

Table 5: List of the investigated material parameters, including their range of value and the resection steps. [154]

Resection step	Resected structure	Investigated structure	Investigated parameter range
0	- (Intact)	LCTS	$k_{\mathrm{LCTS}} = 100 - 10000$ MPa
1	LCTS	ACT	$k^{\mathrm{ACT}}_{x'',y'',z''} = 0.05 - 15$ N/mm^2, $k^{\mathrm{ACT}}_{rx'',ry'',rz''} = 10 - 100000$ Nmm/rad^2
2	LCTS, ACT	ACC	$k^{\mathrm{ACC}}_{x',y',z'} = 0.05 - 15$ N/mm^2, $k^{\mathrm{ACC}}_{rx',ry',rz'} = 10 - 100000$ Nmm/rad^2

Data analysis

To check the plausibility of the results, the computed RoMs were compared to the *in vitro* data published by Lemosse [104]. The second resection step was neglected as the influence of the LCT was integrated in the properties of the ACC. Since no distinction was made between positive and negative loading conditions within the published data, it was assumed that rotation around an axis is symmetrical towards positive and negative direction.

To identify how strongly a variation each of the input parameters (morphology and material) affected the RoM, the Spearman correlation coefficient was determined for each pair of input parameter and response variable. In order to calibrate numerical models to emulate physiological mechanical behaviour, it was important to understand how the different input parameters interact. Therefore, the correlation of the model responses with all of the 262,143 possible multiplicative combinations of input variables was computed. Their influence on the RoM in each load-direction and resection step was then investigated. To accomplish this, all parameter values (p) were non-dimensionalized (p^*) using the equation:

$$p_i{}^* = \frac{p_i - p_{\min}}{p_{max} - p_{min}}, \qquad \textit{(Eq. 10)}$$

Spearman correlation coefficients were computed using the SciPy package [83]. *(see [154])*

2.2.3 Material calibration

The main parameter which was targeted during the calibration process was the range of motion of a joint. The RoM was defined as the maximal deflection angle while applying pure moments around the anatomical axes. A vertebral segment deforms non-linearly while applying pure moments in flexion-extension, lateral bending and axial rotation, as illustrated in Figure 18a.

The RoM can simply be obtained from numerical simulations and compared to *in vitro* experiments. The main question was: which material properties led to a certain RoM when considering the subject-specific morphology?

After the parameter analysis (chapter 2.2.1.3, 2.2.2.3), a parameter database was obtained which contained the relationship between morphology, material properties and RoM around each motion axis and at each resection step for the vertebral segment and the CVJ. From this database, the material parameters were extracted which theoretically should lead to a targeted RoM with a given morphology, as illustrated in Figure 17. (*see* [152])

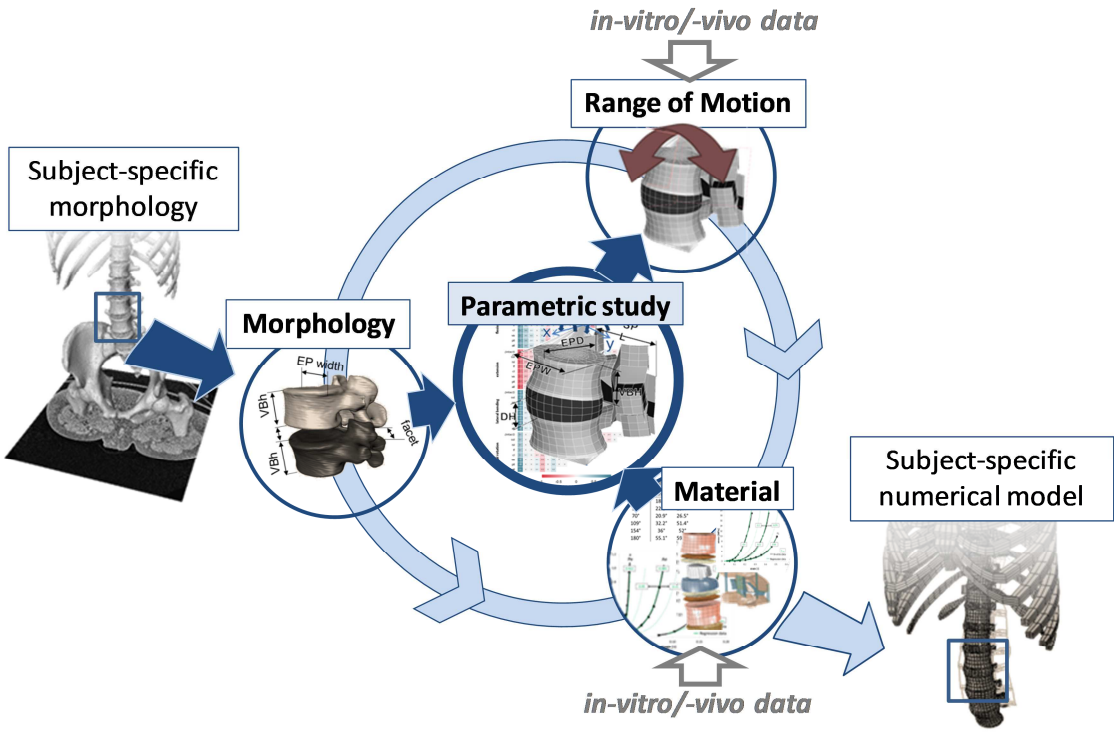


Figure 17: Sketch on the material calibration procedure, exemplary for the vertebral segment. First, a parameter study is performed using morphology and material parameters. As a result, the RoM of each parameter combination is obtained. Then, from a given morphology and a targed RoM, the material parameters were deduced and assigned to the numerical model.

2.2.3.1 Background on calibration data

Prior to performing material calibration, the targeted RoM values needed to be determined. This RoM-data of the vertebral segments were obtained from our in-house (UFB-institute) *in vitro* data, while the RoM data of the CVJ were extracted from the literature.

The ultimate goal was to assign any desired RoM within the physiological range of a joint to the model. Therefore, the *in vitro* data was non-dimensionalized towards a predefined reference condition. This reference condition was defined as the RoM at 7.5 Nm for a lumbar and 2.5 Nm for a thoracic intact segment in flexion-extension. All other resection steps and motion directions were referred to this RoM, as illustrated in Figure 19.

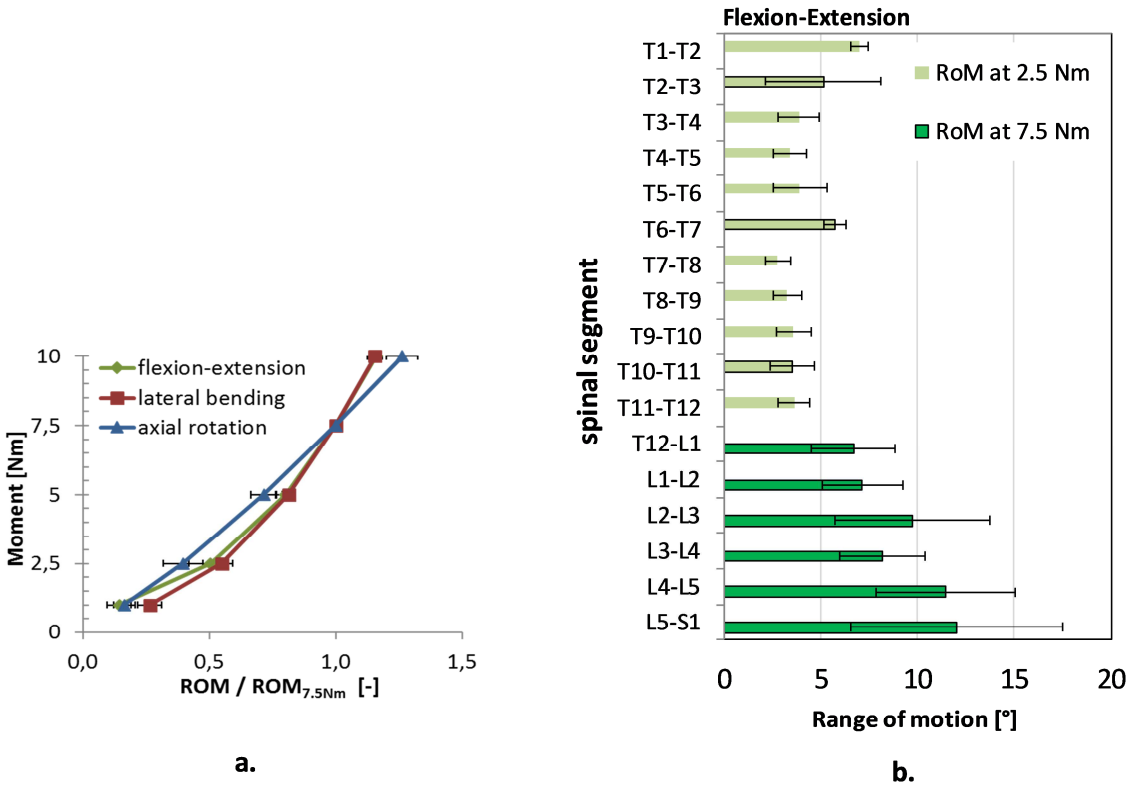


Figure 18: a. Range of motion (RoM) at different moments and directions, relative to the moment of 7.5 Nm. In-vitro data obtained from Heuer [71]. b. Total RoM of spinal segments in flexion and extension while applying 2.5 Nm in the thoracic region and 7.5 Nm in the lumbar region. The RoM values within the black box indicate RoM values that were directly obtained from in vitro experiments. The other values were interpolated from RoM measurements at 7.5 Nm by multiplying the values by 0.5 (see Figure a). In vitro data was obtained from [62, 70, 71, 187].

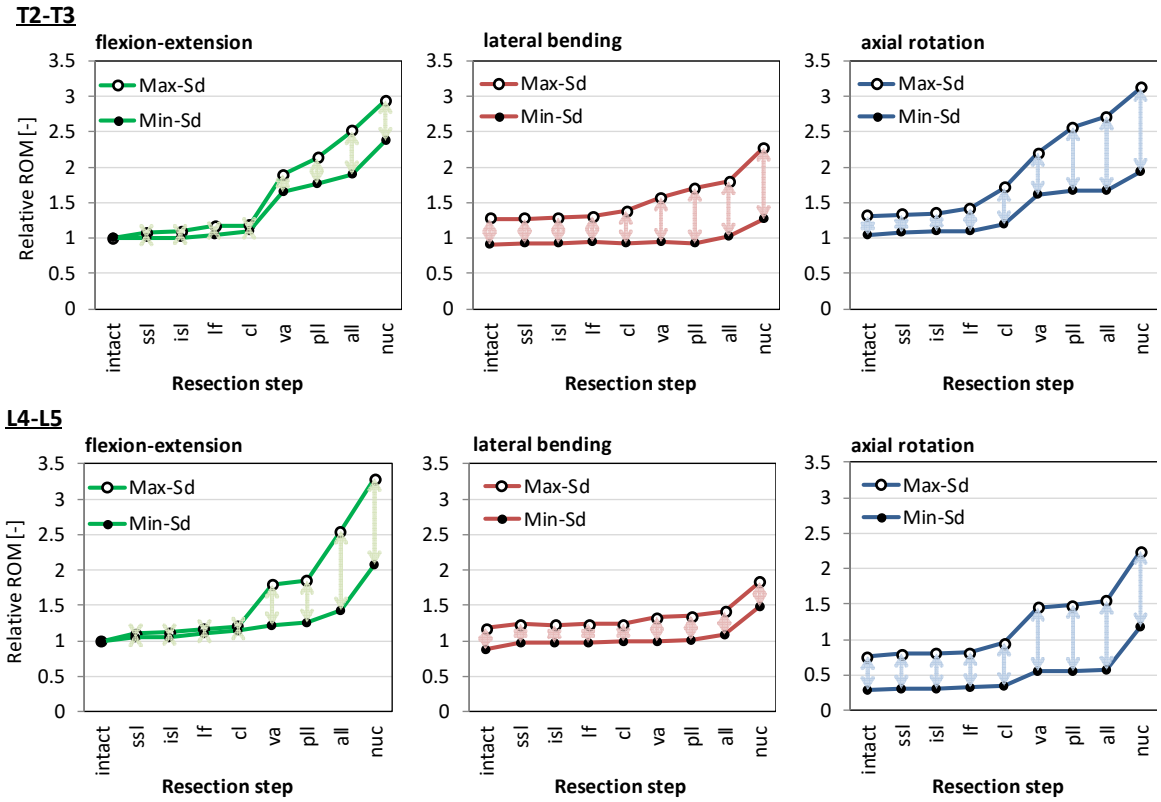


Figure 19: RoM values relative to the intact condition at flexion-extension for the thoracic region (T2-T3) and the lumbar region (L4-L5). The coloured region indicates the region of the standard deviation. In vitro data was obtained from Heuer [71]. (SSL: supraspinous ligament, ISL: interspinous ligament, lf: ligamentum flavum, CL: capsular ligament, va: vertebral arch, pll: posterior longitudinal ligament, all: anterior longitudinal ligament, nuc: nucleotomy)

2.2.3.2 Calibration procedure

As reference RoM, the RoM in combined flexion-extension at the intact condition was chosen. From this reference RoM, the possible range of variability of the RoMs was estimated at each resection step in all three directions. These values were then compared to the standard deviation reported by Heuer [71].

Subsequently, the material parameters were extracted from the parameter database using the nearest-neighbour methodology, in which the best parameter combination was identified that fitted to the expected RoM values. (*see* [152])

The accuracy of this method was tested by calculating the deviation between the expected RoM values from the *in vitro* data and the RoM values obtained by using the extracted material parameters. Fifteen models were created by increasing the reference RoM stepwise by 0.1° within the *in vitro* measured RoM range for an L4-L5 segment

between 6° and 21° [185]. Finally, the calculated deviations were averaged over all models, thus obtaining the accuracy of the desired RoM within the investigated parameter range. A basic procedure of the calibration process is illustrated in the appendix (A-2).

2.3 Intrapleural pressure model

The analysis of the weight and load-bearing structures within the upper body suggested that the main load on the erect spine originates from the head, the arms, muscles, bones and the intrapleural pressure. It was assumed that the latter includes the weight-impact of the intrathoracic and intraabdominal organs on the spine.

Considering the asymmetrical distribution of the organs within the thorax, it was hypothesised that a potential asymmetry in the intrapleural pressure has an impact on the shape of the spine. Therefore, focus was placed on the modelling of the intrapleural pressure distribution.

2.3.1 Background to pleura mechanics

Some fundamental concepts of pleural mechanics have been elaborated and summarized in the last decades [2, 98]. However, only a few researchers attempted to measure the IPP directly. Generally, the IPP at the end of expiration depends mainly on the recoil force of the lung [64], the weight of the heart and the abdomen [15, 77, 112], and the amount of fluid in the pleural space (thickness of the interpleural space) [2, 42].

During inspiration, additional loads triggered by the contraction of the diaphragm and thoracic muscles increase the magnitude of the IPP from approximately -300 Pa at the end of expiration to -1000 Pa at the end of inspiration [86].

A vertical pressure gradient in caudocranial direction exists along the chest wall which is not in hydrostatic equilibrium. The gradient varies in vertical and ventral-dorsal direction of the rib cage, while its magnitude depends on posture [2, 14, 37, 97, 148, 149, 171].

The weight of the abdomen [2] as well as the weight of the heart [15, 77] increase the vertical gradient. In particular, a change in the pressure gradient at the cranial border of the heart was observed in dogs [14, 171].

Table 6: Literature data on end-of-expiration measured intrapleural pressure gradients in dogs and pressure magnitudes in human. c.b.: cardiac border, i.c.s.: intercostal space [153]

Literature	Method	Subject	Vertical gradient [Pa/mm]	Measurement site
Krueger 1961 [96]	Pleural balloon	Dog (n=15)	Upright: above c.b.: -2.45, *below* c.b.: -5.50	Right side, from 4^{th}/5^{th} i.c.s to costophrenic sulcus
Suprenant 1963 [171]	Needle	Dog (n=8)	Upright: -9.12 ± 1.96	Right side, between 3^{rd}/4^{th} & 7/8/9^{th} i.c.s
Banchero 1967 [14]	catheter	Dog (n=5)	Upright: mean -7.06 Above c.b.: -2.94, below c.b.: -9.80	Left side, between apical and basal sites from heart.
McMahon 1969 [122]	Pleural balloon	Dog (n=4)	Upright: -1.96	Left side, between 3^{rd} & 6^{th} i.c.s
Coulam 1971 [35]	pleural catheter	Dog (n=6)	Upright: mean -5.89 ± 0.49 Above c.b.: -4.31, Below c.b.: -8.83	Left & right side, between apical and costophrenic surface
Rutishauer 1966 [148, 149]	Pleural catheter	Dog (n=9)	Supine: -6.27 ±0.40* Prone : +8.92 ± 0.53*	Right side, around c.b., *gradient from dorsal to ventral site
Wiener-Konish 1984 [183]	Rib capsule	Dog (n=15)	Upright: -5.20 ± 3.14 Supine: -4.51 ± 1.67 Prone: -2.25 ± 2.55	Right side, between 4^{th} & 6^{th} rib
			Absolute values [Pa]	
Cherniack 1955 [31]	Needle	Human (n=15)	Supine: -300 to -2600	In ventral 3^{rd}/4^{th} i.c.s
Kawamata 1994 [86]	Needle	Human (n=11)	Side: -280 ± 40	Below 8^{th} rib

To the best of the author's knowledge, measurements concerning the IPP gradient in humans are not available in the literature to date. However, it can be assumed that the IPP gradients are similar to the values measured in dogs, since the esophageal pressure gradients [171] and surface pressure gradients in both are comparable. Most likely, the absolute IPP values vary in a broad range between individuals due to differences in body size, anatomy, weight and weight distribution.

2.3.2 Pleura model generation

The IPP was applied perpendicular to the inner pleural surface in the region of the lung (Figure 20). An upright posture was modelled in which the IPP distribution was assumed to vary in the vertical direction only.

The exact distribution of IPP is difficult to estimate since the published data were quantified with different methodologies (Table 6). Different IPP distributions were simulated (Table 7): firstly, a constant IPP gradient of -6 $\frac{\mathrm{Pa}}{\mathrm{mm}}$, and secondly, a stepwise IPP gradient of -9 $\frac{\mathrm{Pa}}{\mathrm{mm}}$ below and -3 $\frac{\mathrm{Pa}}{\mathrm{mm}}$ above the cardiac border. An IPP of -300 Pa at the base of the lung was assumed (Figure 21). The pressure was assumed to be uniformly distributed in the transverse plane. The lung base was positioned at the level of the superior endplate of T11. *(see* [153]*)*

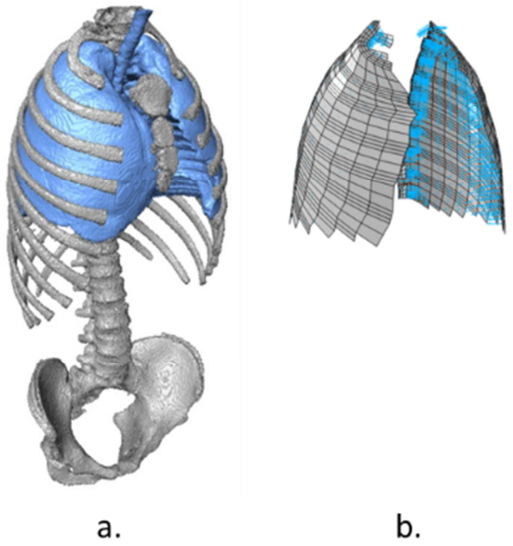


Figure 20: a. Reconstructed lung within the chest (blue). b. pleura surface of the chest with the vectors (blue) illustrating the region and the direction the interpleural pressure is acting. This surface is attached to the inner rib surface. [153]*; [Reprinted with permission from Springer Nature]*

Additionally, the effect of a potential difference in the IPP gradient between the left and right chest sides was investigated. The IPP asymmetry was induced by either reducing the gradient by 1 $\frac{\mathrm{Pa}}{\mathrm{mm}}$ on one side, or by reducing the base pressure to -200 Pa.

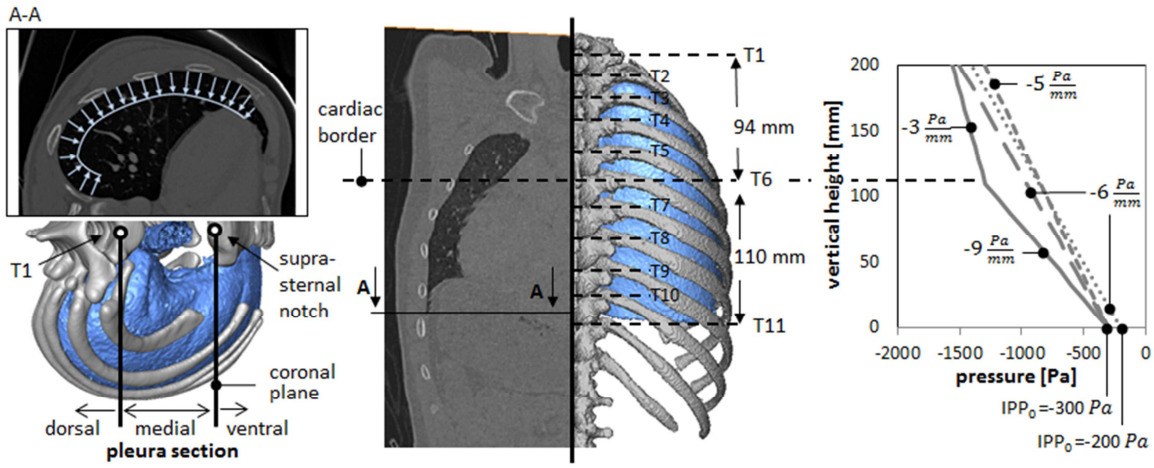


Figure 21: Modelled intrapleural pressure distribution acting on the inner chest wall. The pressure was distributed evenly within the transverse plane. In the vertical direction of the chest, three different cases of possible intrapleural pressure distributions were investigated (based on the literature in Table 6. [153]; [Reprinted with permission from Springer Nature]

Table 7: List of all simulated pressure distributions on the left and right side of the rib cage. c.b.: cranial border [153]

#	left pleura side				right pleura side			
	base IPP [Pa]	IPP gradient [Pa/mm]			base IPP [Pa]	IPP gradient [Pa/mm]		
		dorsal	medial	ventral		dorsal	medial	ventral
1	-300	-6			-300	-6		
2	-300	below c.b.: -9, above c.b.: -3			-300	below c.b.: -9, above c.b.: -3		
3	-300	-6			-300	-5		
4	-300	-5			-300	-6		
5	-300	-6			-200	-6		
6	-200	-6			-300	-6		
7	-300	-6			-300*	0	-6	-6
8	-300	-6			-300*	-6	0	-6
9	-300	-6			-300*	-6	-6	0

*only if IPP gradient is not 0, else 0 Pa

3. Results

A fully parametric model of the spine and chest was developed. At first a morphology database was created, which included information on shape and size of the spinal sections from T1 to S1 along with the corresponding ribs and the sternum.

From this given parameter database, a complete finite element model could be automatically generated. This included involving geometry generation, meshing, material assignment and implementation of the boundary conditions according to the workflow in Figure 9.

3.1 Morphology analysis

The morphology of 21 individuals diagnosed with AIS (AIS group) and 48 subjects without any visible spinal abnormalities (healthy group) were successfully analysed.

The inter/intra-rater variability was quantified by calculating the coefficient of variation and analysing the data using the Bland–Altman plot, as illustrated in Figure 22. On average, a coefficient of variation of 3% was obtained for the vertebral body height and the intervertebral disc height. The highest coefficient of variation was measured for the

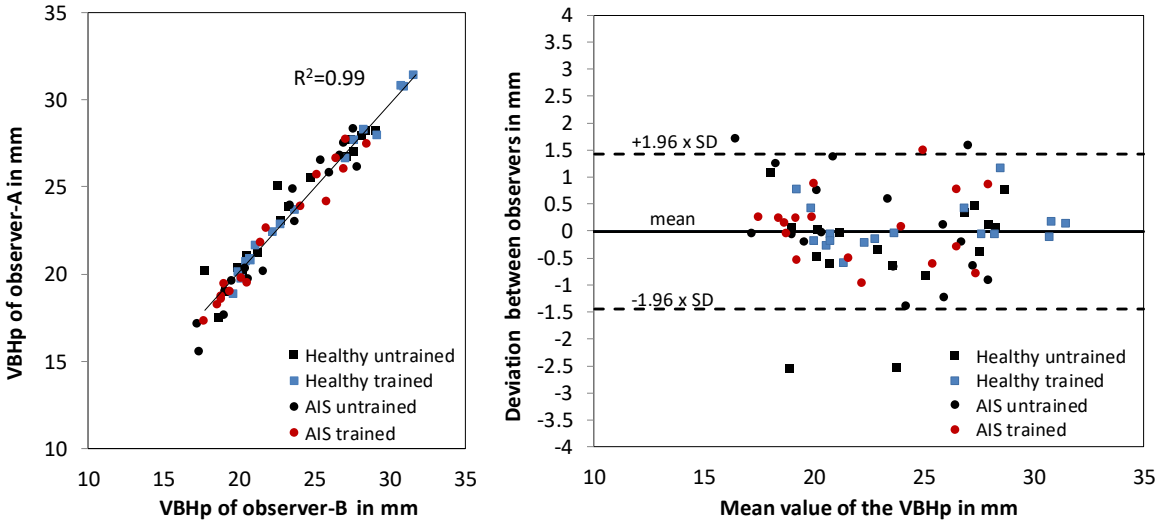


Figure 22: Exemplary inter- and inrarrater variability during the placement of the landmarks by two observer to calculate the posterior vertebral body height (VBHp). The squared points indicate the variability by placing landmarks on a healthy spine, and the circled points by placing landmarks on a scoliotic spine. The regression line in the left image indicates that the agreement between two observers dependently on the magnitude of the parameter. The Bland–Altman plot on the right illustrates the range of variation of the paramter. Untrained reflects the value of a (SD: standard deviation, AIS: adolescent idiopathic scoliosis)

orientation of the superior endplate surface (39%), articular facet joints (17%) and costovertebral joints (12%).

3.1.1 Non-scoliotic (healthy) patient group

The lateral displacement relative to the mid-sagittal plane of each individual coordinate system of the healthy patients varied in the ranges of -1.3 ± 5.0 mm at T7 and 0.8 ± 3.4 mm at L4 (Figure 23). Interestingly, the vertebrae of the healthy group exhibited an inherent rotation of the vertebrae which deviated significantly from zero at level T2 (2.6° ± 4.3°, $p = 0.009$). It should be noted that the reduction of the lateral displacement to 0 at T1 is due to the reference coordinate system in which S1 and T1 were used as reference points. Despite the high standard-deviation, the relative position of the posterior point of the ribs exhibit, in average, a more dorsal located right rib in the lower thoracic region (T7-T12) compared to the left rib (Figure 23d).

The pedicle area ratio between the left and right side were within the expected mean value of 1.0: between 0.9 ± 0.1 at T6, and 1.1 ± 0.2 at T1. In addition, the shape of the rib cage deformed within the transverse plane (Figure 23c). (*see* [151])

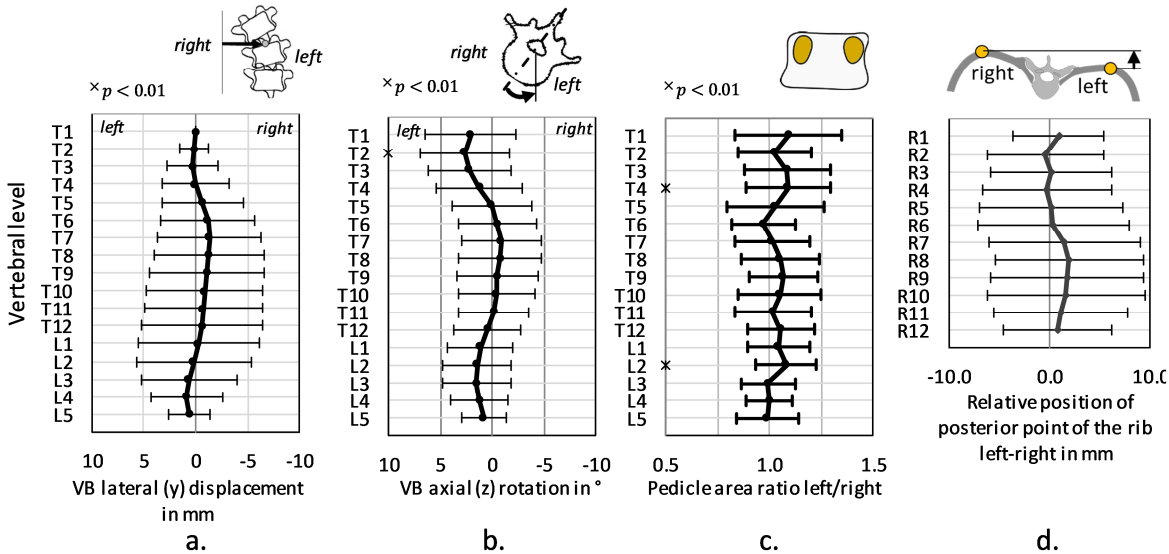


Figure 23: Mean value and standard-deviation at each spinal level of the lateral displacement (a.) and axial rotation (b.) of the vertebral body (VB), as well as the ratio between left and right pedicle area (c.) and deviation between left and right position of the posterior point of the rib (d.) for the non-scoliotic ("healthy") spine group. [151]; [Reprinted with permission from Springer Nature]

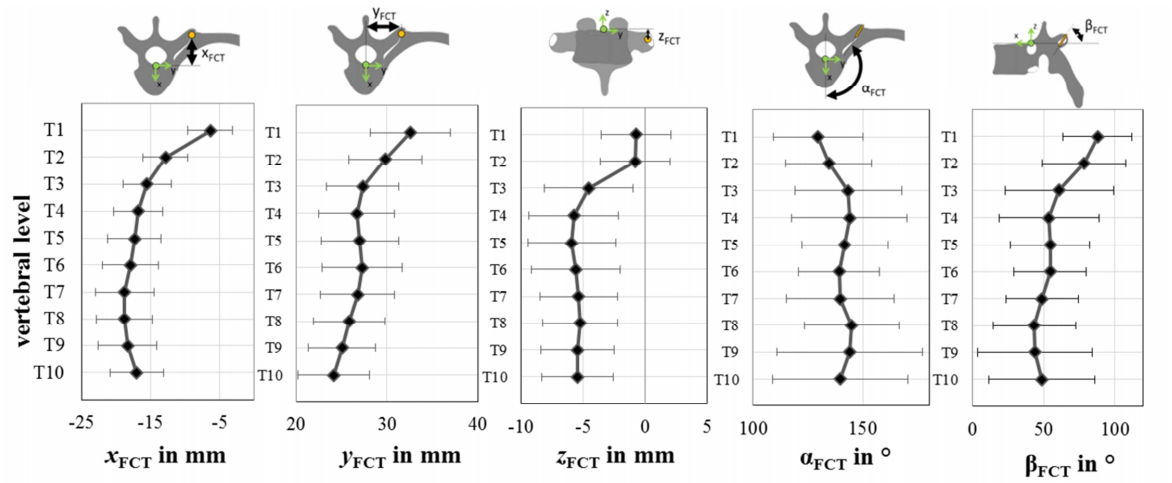


Figure 24: Position and orientation of the fovea costalis transversalis (FCT) relative to the posterior reference point of the superior vertebral endplate, depending on the vertebral level. Values indicate mean and standard deviation. [154] *[Reprinted with permission from Taylor & Francis]*

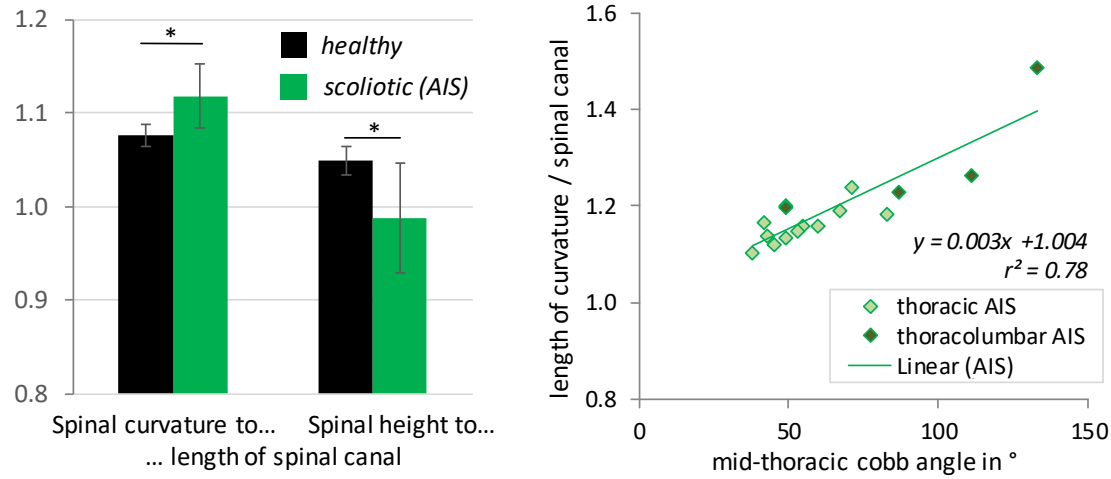
Position of the fovea costalis transversalis (FCT)

The position and orientation of the FCT varied according to the spinal level (Figure 24). The distance from the FCT to the vertebral reference point (x_{FCT}) increased in the dorsal direction from T1 (-6 ± 3 mm) to T8 (-19 ± 4 mm) and then decreased gradually towards T12 (-14 ± 3 mm). In the lateral direction (y_{FCT}) the position decreased from T1 (32 ± 4 mm) to T12 (21 ± 3 mm), whereas along the z-axis, the position remained fairly constant between the mid-thoracic region: T1 (-1 ± 3 mm), T6 (-6 ± 4 mm) and T12 (-11 ± 5 mm). The angle of the FCT varied in the transverse plane between 130° ± 20° at T1, and 145° ± 21° at T8. Within the sagittal plane the angle of the FCT relative to the superior endplate of the vertebrae decreased from 87° ± 24° at T1 to 43° ± 29° at T8.

3.1.2 Comparison between AIS and healthy groups

General length of the spine

Within the healthy group, the height of the spine from T1 to S1 correlated with the length along the spinal curvature ($r^2 = 0.99$) (Figure 26a). All scoliotic spines deviated from the almost perfectly linear relation present in the healthy group towards a disproportionally longer spinal curvature compared to their T1-S1 height. The anterior height of the vertebral bodies was in scoliotic spines higher than in non-scoliotic spines (Figure 26b). Whereas, the pedicle height was on average reduced in patients with AIS. (*see* [151])

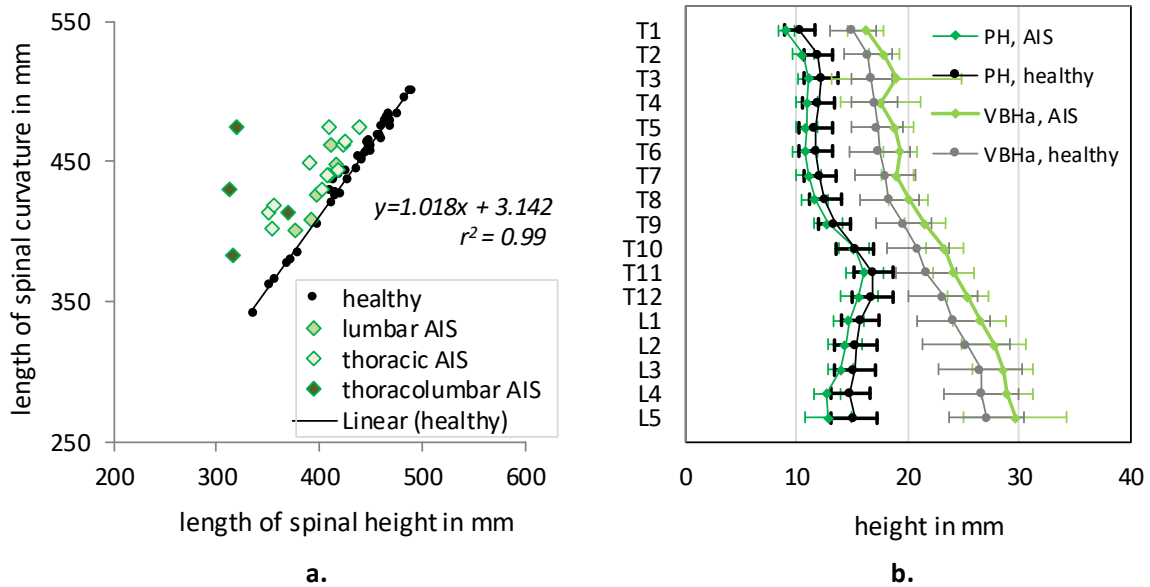


a. **b.**

*Figure 25: **a.** Relation between the length of the spinal canal to the spinal height and spinal length, for non-scoliotic (healthy, dark) and scoliotic spines (AIS, green). A significance level of p=0.01 was assumed. **b.** Relation between the length of the anterior spinal column and the length of the spinal canal compared to the Cobb-angle in the mid-thoracic region (only for thoracic and thoracolumbar scoliotic curvatures). [151]; [Reprinted with permission from Springer Nature]*

Spinal canal length

The average relation between the length along the curvature of the anterior spinal column and the spinal canal length was 1.07 ± 0.01 for healthy spines and 1.12 ± 0.03 for scoliotic spines (Figure 25a). This relation was found to be significantly increased in patients with AIS. In contrast, the relation between length of the spinal height and the



a. **b.**

*Figure 26: **a.** Relation between the length of the curvature and the spinal height for each spine. Linear regression was performed using the data of the healthy-group. [151] **b.** Pedicle height (PH) and anterior height of the vertebral body (VBHa) of non-scoliotic (healthy) spines and AIS. [Reprinted with permission from Springer Nature]*

length of the spinal canal was reduced in patients with AIS. (*see* [151])

The relation between length of spinal curvature and the spinal canal correlated significantly with the mid-thoracic Cobb-angle, measured within the thoracic and thoracolumbar AIS-group ($p<0.01$, Pearson's $r=0.88$) (Figure 25b).

Endplate

The averaged endplate area ($\bar{A}$) was compared to the height of the spine and the length of the spinal curvature (Figure 27). The averaged endplate area in relation to the spinal height could not reveal any differences between the healthy and AIS group. Yet, the endplate area was significantly smaller within the AIS group once the endplate area was compared with the length of the curvature. (*see* [151])

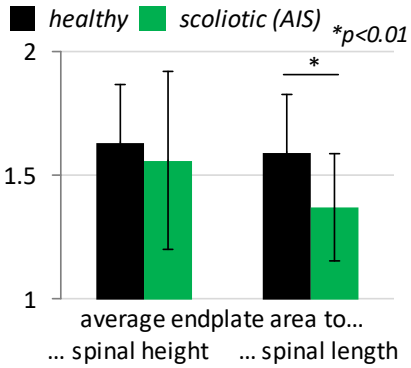


Figure 27: Relation between average endplate area and the spinal height, respectively, the length of the curvature, for healthy and scoliotic spines. [151] [Reprinted with permission from Springer Nature]

Spinal displacement

The lateral displacement of the scoliotic spine was significantly different in relation to the healthy spines. This was dependent on the position of the main scoliotic curvature (Figure 28 a). In the lumbar AIS group, the lateral offset was significantly varied within the lumbar levels and at T2, whereas the thoracic group exhibited significant differences in all levels between T4 and L5, with exception of T12. (*see* [151])

Axial rotation

The analyses revealed that axial rotation increased towards the apex vertebra of the scoliotic curvature (Figure 28b), whereas the rotational peak depended on the type of the scoliotic curvature. For lumbar AIS the values ranged from -8.9° ± 8.1° at T7 and 32.7° ± 5.3° at L1. The axial rotation at thoracic AIS curvatures ranged between -20.7° ± 14.1° at T9 and 25.9° ± 10.5° at L2. At the thoracolumbar AIS a main peak at T9 with -58.5° ± 11.0° was measured. (*see* [151])

Dorsal-ventral displacement

Scoliotic spines generally revealed a reduced kyphosis within the thoracic region, whereas in the lumbar area, the spinal shape in the sagittal plane depended on the type of scoliosis (Figure 28 c). Lordosis was decreased significantly at the levels L1 to L3 in lumber scoliosis types, while lordosis was increased in thoracolumbar scoliosis. (*see* [151])

Shape of the vertebral body

Wedging of the vertebral body was significantly pronounced in all three scoliotic types in the thoracic region between T7 and T10, with a lower vertebral body height on the left (concave) side compared to the right (convex) side of the curvature. A minimal ratio of 0.67 ± 0.1 at T8 in the thoracolumbar AIS group was observed (Figure 28 d). This relation was reversed in the lumbar region for lumbar and thoracic AIS cases, with maximal values of 1.25 ± 0.16.

The relation between the anterior and posterior vertebral body height was generally higher in scoliotic spines than in healthy spines (Figure 28 e). Compared to the posterior height, the anterior height in scoliotic spines was lower in the upper thoracic region (min. 0.91 ± 0.05). In the lumbar region, the heights were equal or in an opposite relation to the thoracic region, with a maximum of about 1.25 ± 0.07. (*see* [151])

Shape of the intervertebral disc

Lateral wedging of the disc was significant in the lumbar region with a maximal value of 2.06 ± 0.37 in the thoracolumbar AIS group (Figure 28f). The relation between the anterior and posterior disc height was overall reduced within the thoracic levels T1 to T9 in the AIS groups in comparison with the healthy spines (Figure 28g). (*see* [151])

Articular facet joint area

The superior facet joint areas exhibited differences especially in the lower thoracic region between T8 and T12, with a relation of 2.3 ± 0.5 (Figure 28 h). This relation was reversed above and below this spinal region, which resulted in a smaller facet area on the left side compared to the right facet (min. 0.5 ± 0.2 at T4 for thoracolumbar AIS). (*see* [151])

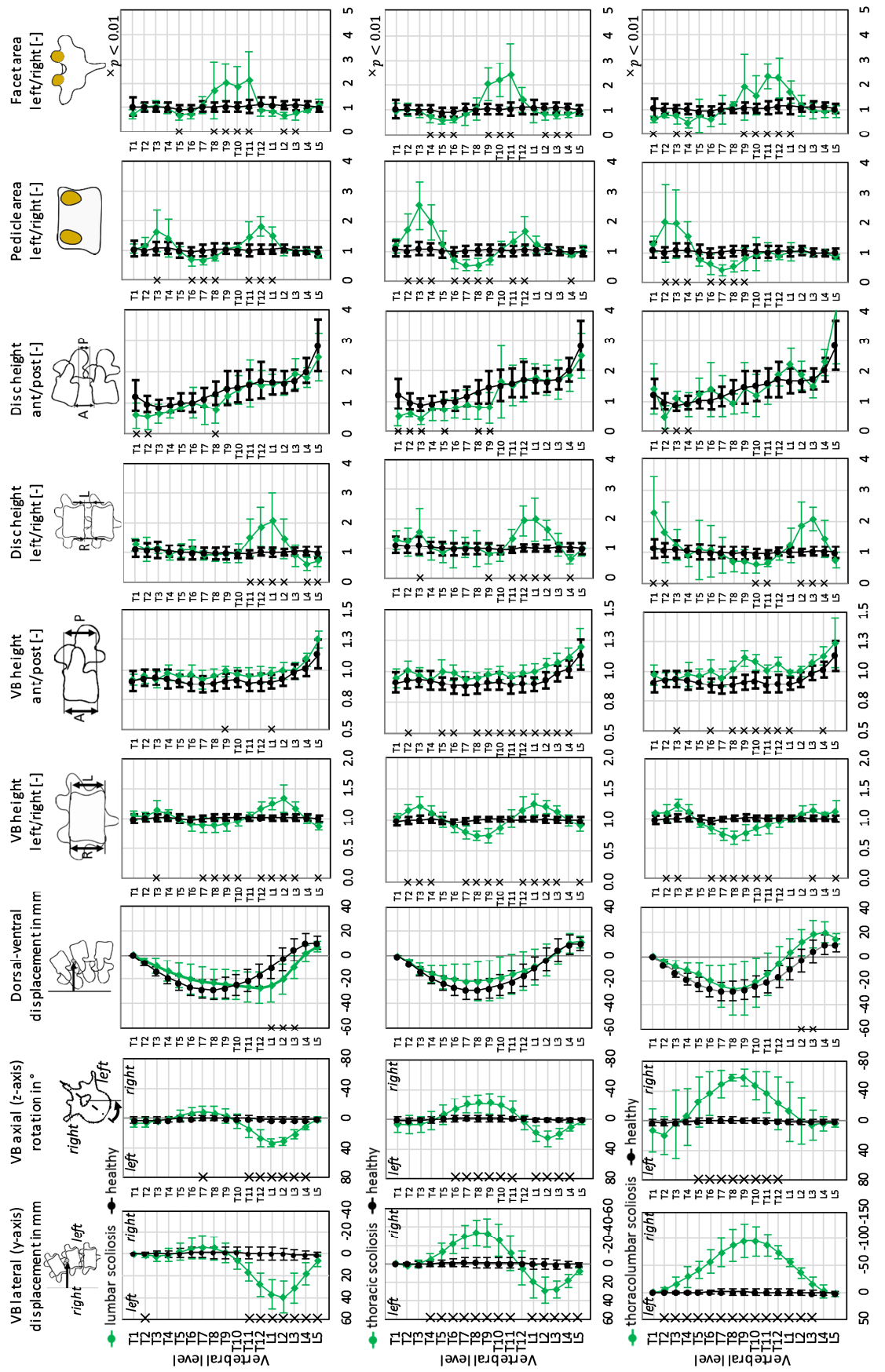


Figure 28: Nine morphology parameters (a.-i.) and their development along the spinal levels for healthy spines (black) and scoliotic spines (green). Scoliotic spines were grouped depending on the position of the main scoliotic curvature: top row lumber AIS (n=5), middle row thoracic AIS (n=12) and bottom row thoracolumbar AIS (n=4). [151]; [Reprinted with permission from Springer Nature]

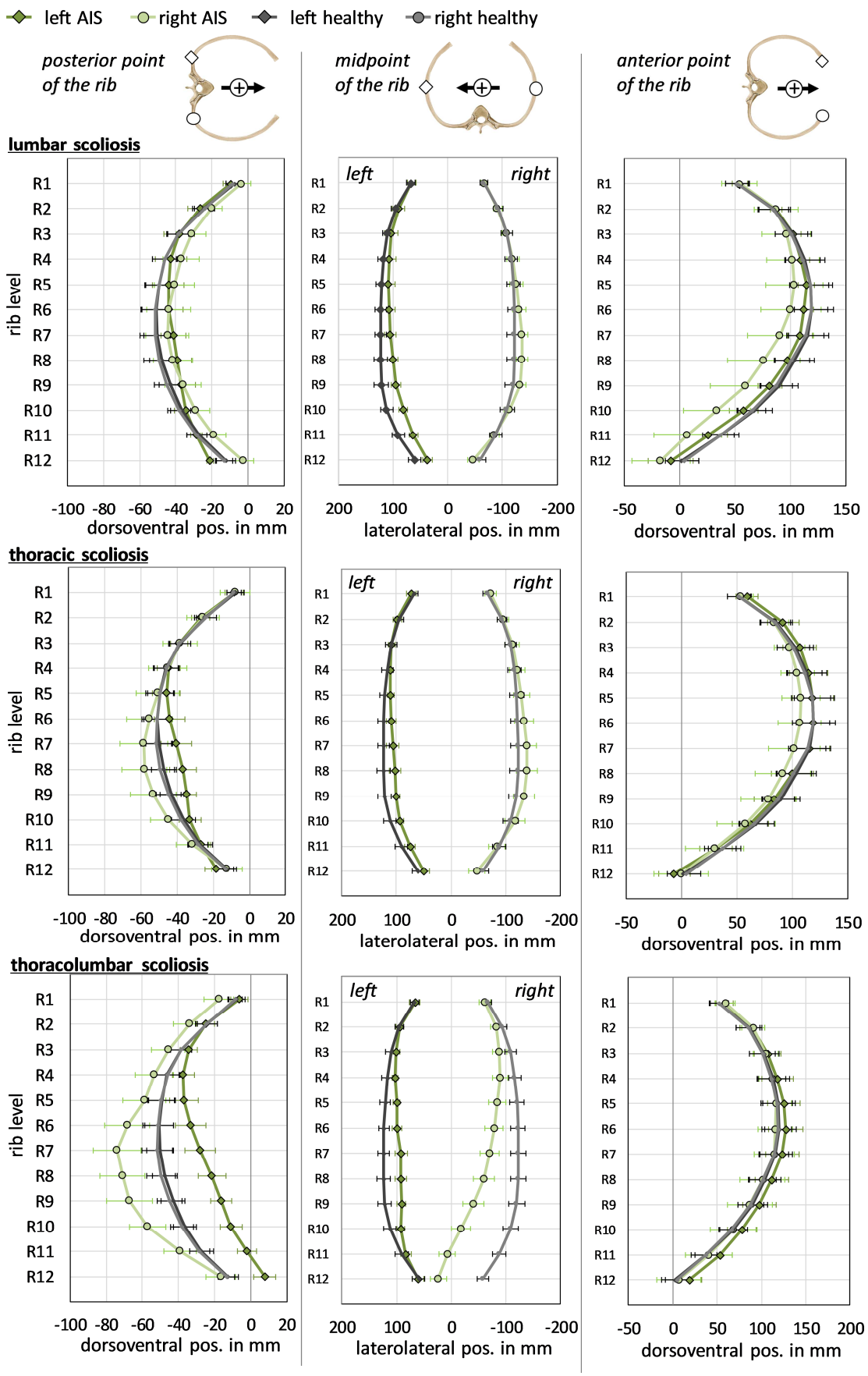


Figure 29: Position (pos.) of the ribs on the right and left side of AIS-patients and non-scoliotic ("healthy") patients. The positions are calculated relative to the chest coordinate system, which is defined as: the z-axis points from T12 to T1, the x-axis from T1 to the costo-sternal notch and the y-axis points left perpendicular to the z-x plane.

Pedicle cross-sectional area

Differences within the cross-sectional area of the pedicles between left and right side were found to be pronounced in the thoracic region, independent of the scoliotic type (Figure 28i). High peaks were measured around T3 (2.5 ± 0.79 for thoracic AIS), T7 (0.4 ± 0.19 at thoracolumbar AIS) and T12 (1.8 ± 0.3 at lumbar AIS). (*see* [151])

Rib cage deformation

All scoliosis types exhibited a deformed rib cage relative to the healthy control group (Figure 29). The deformation was most pronounced in the mid to lower level of the ribs. In the case of lumbar scoliosis, the ribs on the left and right sides were positioned more ventrally in the mid-thoracic region. Thoracic and thoracolumbar scoliosis were associated with an asymmetrical deformation of the rib cage: the ribs on the right convex side were further dorsal, while the ventral ribs were positioned more ventrally compared to the ribs attached to a healthy straight spine.

3.2 **Finite Element model of the spine and chest**

3.2.1 Spinal segment

The impact of uncertainty of the 12 spinal material parameters and the facet gap size was examined. Of the 500 parameter combinations, 432 converged successfully. As expected, the material properties had a strong effect on the RoM. (*see* [152])

Obtained RoM at each resection step

The assumed lower and upper bounds of the parameters resulted in an RoM ranging from 6°-17° in the intact condition in flexion-extension, from 5°-22° in lateral bending, and from 3°-14° in axial rotation (Figure 30). The RoM generally increased once each structure was removed. The difference between each resection step became more visible by observing the relative change of the RoM between two consecutive resection steps ($ROM_{step,i+1} / ROM_{step,i}$) (Figure 32).

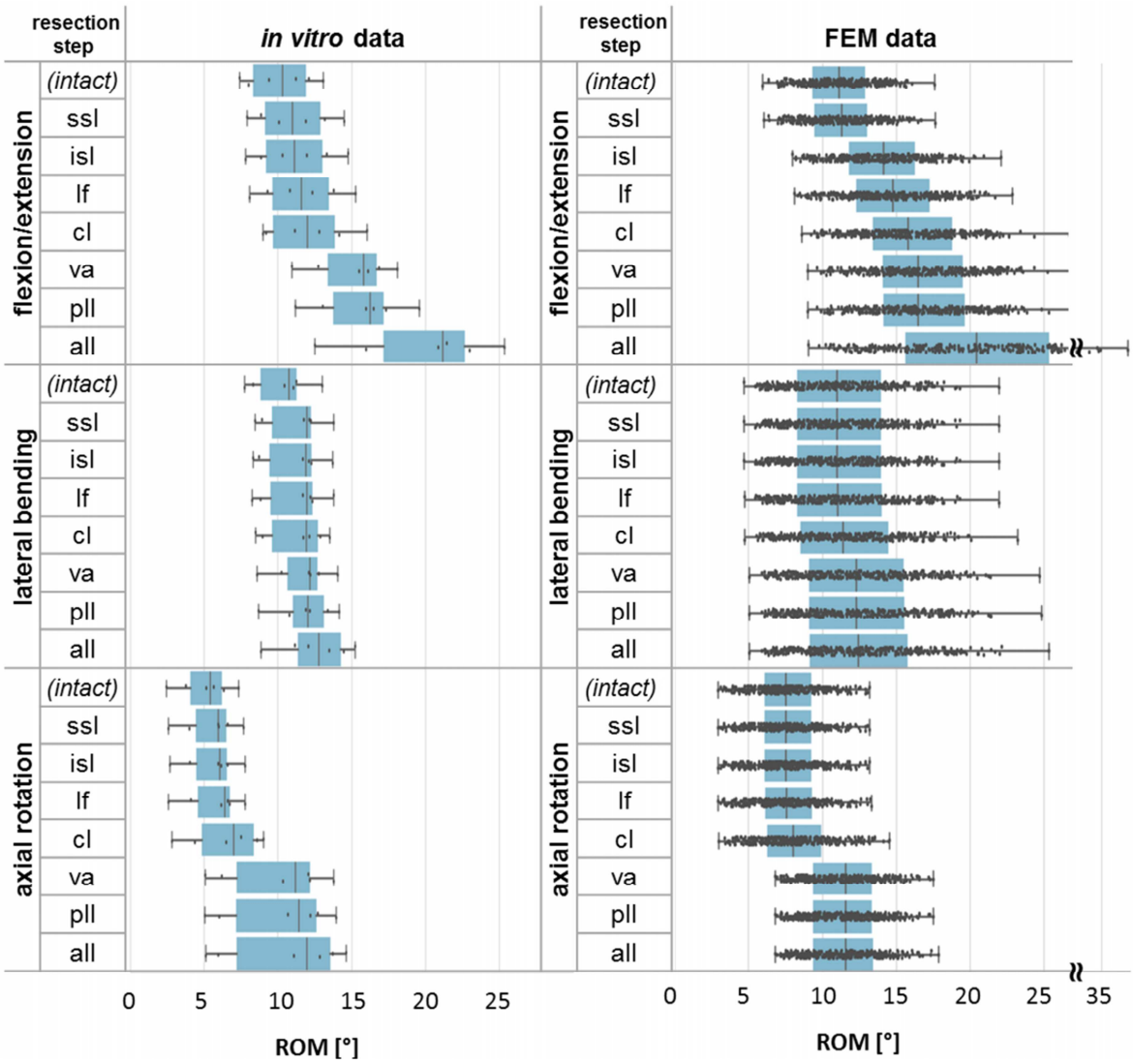


Figure 30: Variation in RoM depending on load direction and resection step. Left: In vitro data from Heuer et al. [71]. Each dot represents an individual spinal segment specimen. Right: simulation results. Each dot represents a specific parameter combination. [152]; [Reprinted with permission from Taylor & Francis]

Varying the facet gap between 0.5 and 5 mm caused a change in RoM in axial rotation by a factor between 1.1 and 2.8 compared to the range 1.4 and 1.8 measured *in vitro*. The property of the ALL altered the RoM values in flexion and extension by a factor of up to 1.7. (*see* [152])

Impact of the parameters on the RoM

The RoM was most sensitive towards the variation of the material properties of the ALL and the annulus, as well as the width of articular facet gap (Figure 31).

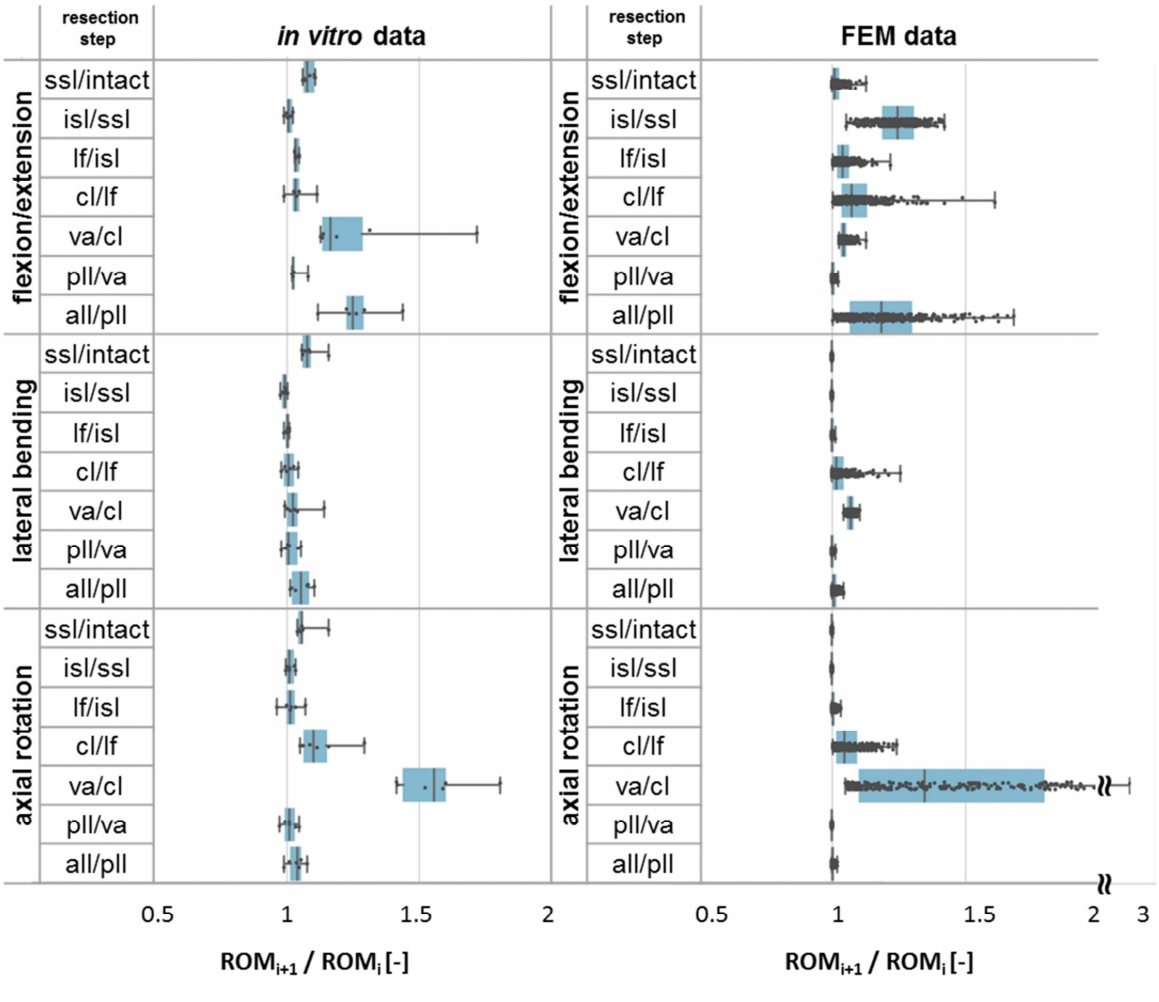


Figure 32: Variation of the relative change in RoM between subsequent resection steps, depending on the load-direction and resection step. Left: In-vitro data obtained from Heuer et al. [71]. Each dot represents a spinal motion segment. Right: simulation results. Each dot represents a specific parameter combination. [152]; [Reprinted with permission from Taylor & Francis]

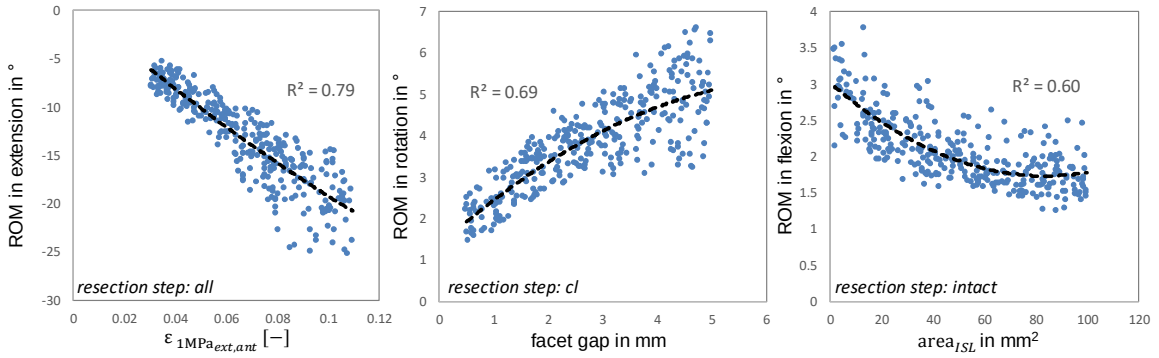


Figure 31: Relations between the RoM and the three most influential parameters: the property of the anterior annulus fibrosus, the facet joint gap and the area of the interspinous ligament. Each dot represents a specific parameter combination. High correlation values correspond to low scattering around the regression lines. [152]; [Reprinted with permission from Taylor & Francis]

The heat map of the Spearman's rank correlation coefficient illustrates how strong each parameter correlated with the RoM obtained at each resection step and loading condition (Figure 33). This plot reveals that the strain of the annulus fibrosus in the anterior region gained correlation values up to ±0.9 in all loading directions. As the facets joints were added, its correlation value dropped to 0.5 in axial rotation. The Spearman correlation coefficient between the RoM and the facet joint gap was 0.8 in axial rotation. Many material parameters of the intervertebral disc had correlation values smaller than 0.5, particularly the parameters seen for the angle of the annulus fibres. (*see* [152])

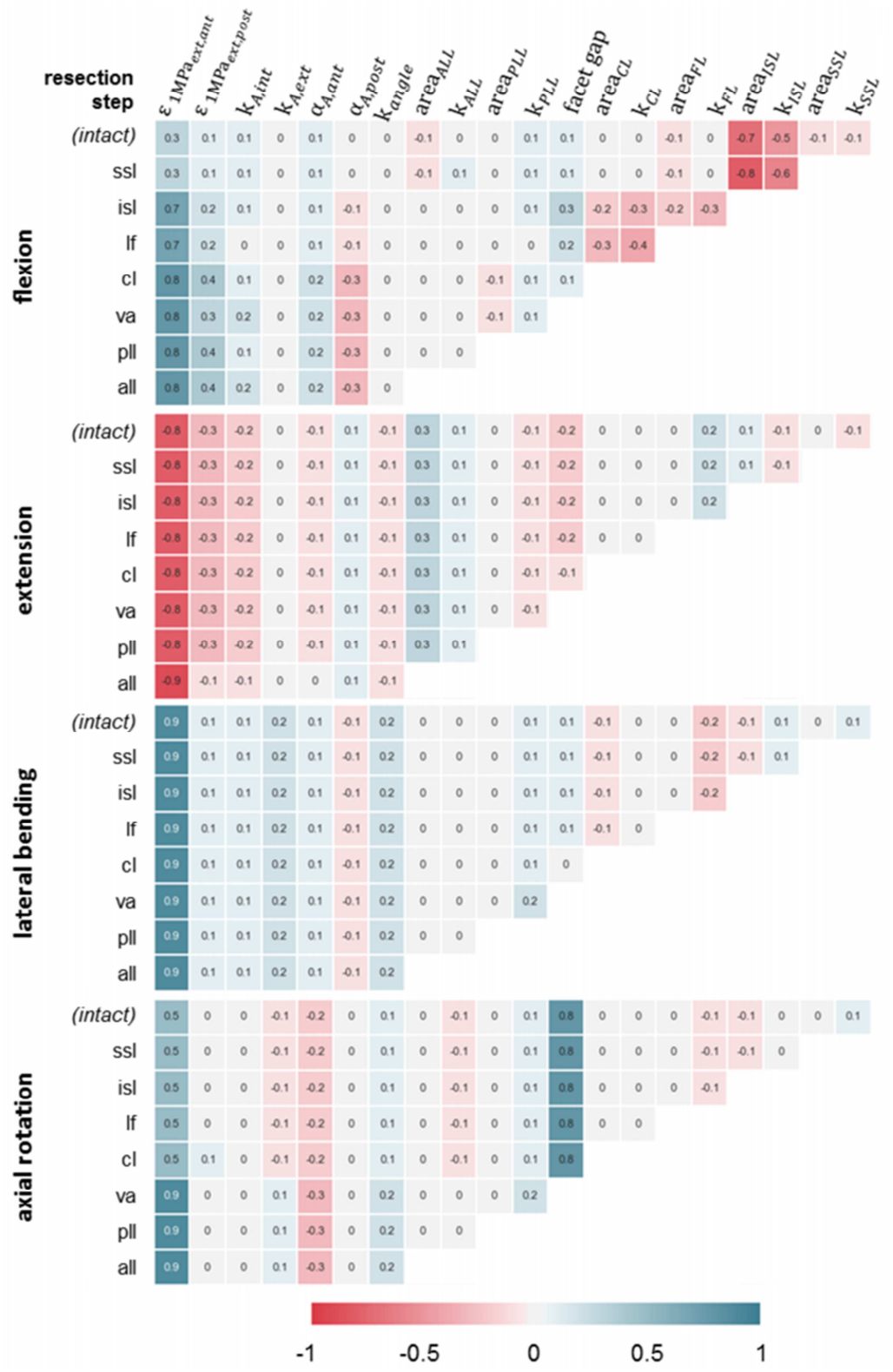


Figure 33: Spearman correlation coefficients of each modified parameter depending on the resection step and load application. [152]; [Reprinted with permission from Taylor & Francis]

3.2.2 Costovertebral joint

The impact of the value of thirteen material and five morphology parameters was investigated. Of the 2000 simulated parameter combinations, 1487 converged successfully for all load cases and resection steps. Unconverged results were mostly caused by extreme parameter combinations at the limits of the allowed parameter ranges which led to unstable conditions. *(see [154])*

Sensitivity analysis

The RoM computed for each loading condition and resection step of every parameter combination was recorded and compared to the *in vitro* data published by Lemosse (Figure 34). The variation of the material and morphology parameters resulted in torsion around the rib head with an RoM between 5.4° and 30.1°, whereas according to Lemosse, the RoM can vary within a standard deviation between 9° and 24°. After resecting all ligaments, leaving only the ACC joint (step-2), the RoM increased to an RoM between 9.7° and 39.8°, while *in vitro* ranges between 11.8° and 40.2° were reported. The sudden increase in the RoM at resection step 2 was also observed for all other loading conditions, *in vitro* as well as numerically.

The correlation plot illustrates how strongly each individual input parameter correlates

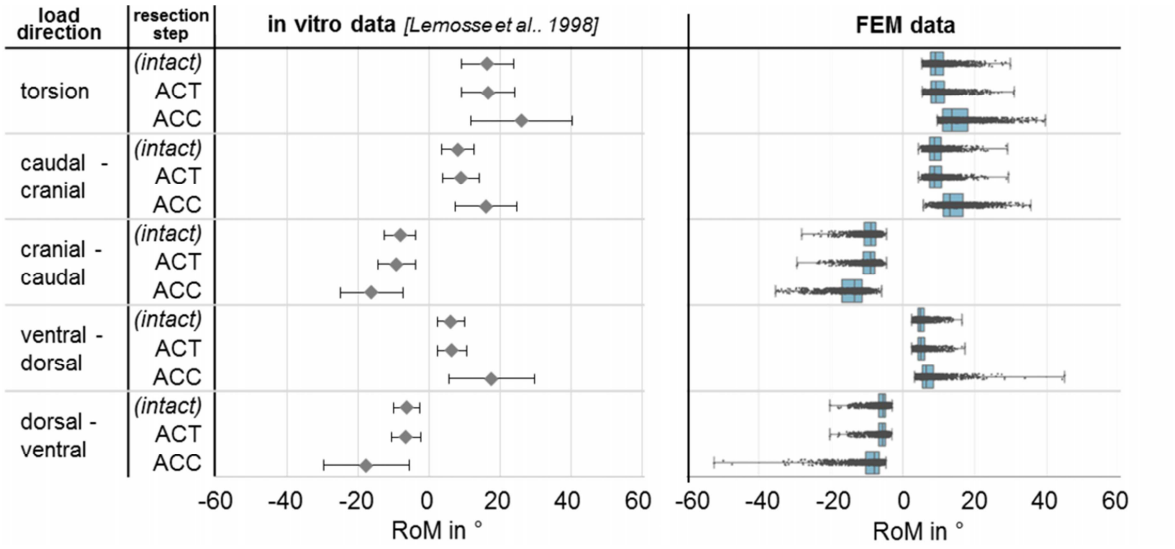


Figure 34: Range of motion (RoM) for different load conditions and resection steps. Left: Mean and standard deviation of the published data from Lemosse (Lemosse et al., 1998). Right: Distribution of the RoM obtained by varying the material properties. Each dot represents the FE-result of one specific parameter-combination. [154]; *[Reprinted with permission from Taylor & Francis]*

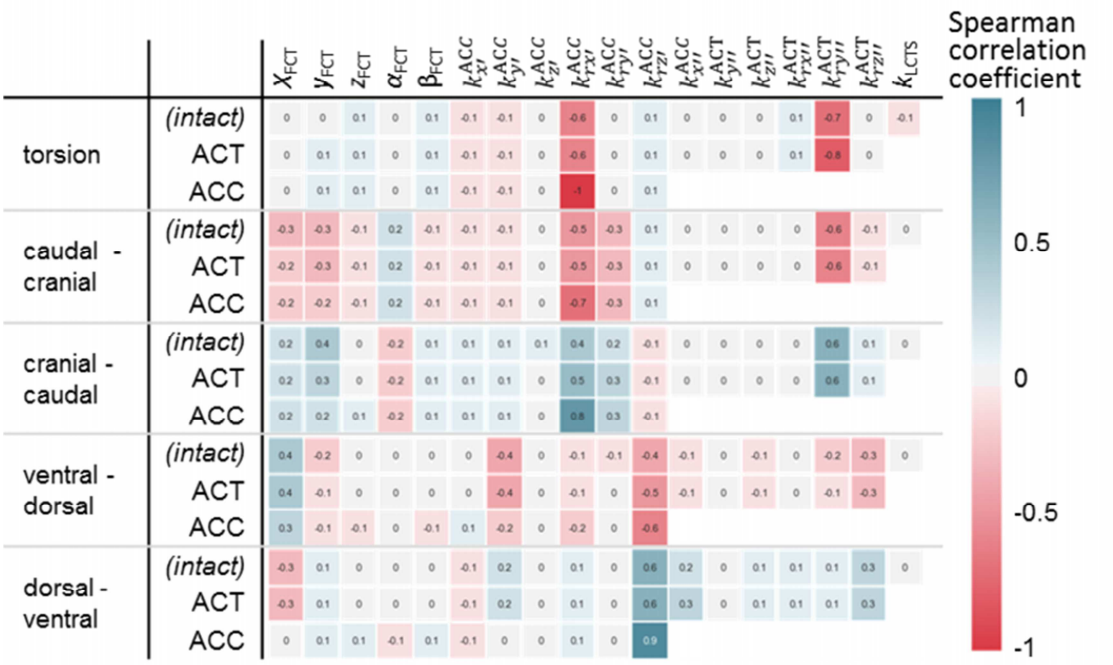


Figure 35: Spearman correlation coefficient for the varied parameters at different loading conditions and resection steps. x_{FCT}, y_{FCT}, z_{FCT}: Transversal and rotational offset of the fovea costalis transversalis to the vertebral body; k^{ACC}, k^{ACT}: transversal (x,y,z) and rotational (rx, ry, rz) stiffness of the articular capitis costae (ACC) and articular costae transverarium (ACT) relative to their coordinate system (', ''); k_{LCTS}: stiffness of the ligament costo transversarium superius (LCTS). [154]; *[Reprinted with permission from Taylor & Francis]*

with the determined RoM at each resection step and loading condition (Figure 35). The most influential parameter on the RoM in torsion was stiffness of the rotational stiffness of the ACC around its *x*-axis ($k_{rx'}^{\mathrm{ACC}}$) and of the ACT around its *y*-axis ($k_{ry''}^{\mathrm{ACT}}$). Similar results were obtained for the RoM around the cranial-caudal axis. In the ventral-dorsal direction the rotational stiffness of the ACC around its *z*-axis ($k_{rz'}^{\mathrm{ACC}}$) demonstrated the highest amount of correlation.

Regarding the morphology parameters, the ventral-dorsal position (x_{FCT}) and the lateral position (y_{FCT}) of the FCT exhibited the highest correlation values of up to ±0.4. This coefficient decreased to less than ±0.2 during torsion and once the ACT was resected. For the orientation angles of the FCT, low correlation values of less than ±0.2 were obtained.
For the intact condition, the combination of the parameters $k_{rx'}^{\mathrm{ACC}}$ and $k_{ry''}^{\mathrm{ACT}}$ showed the strongest influence on the RoM in torsion (Figure 36). Table 8 summarizes the most important input parameter combinations that are required to achieve a desired mechanical response.

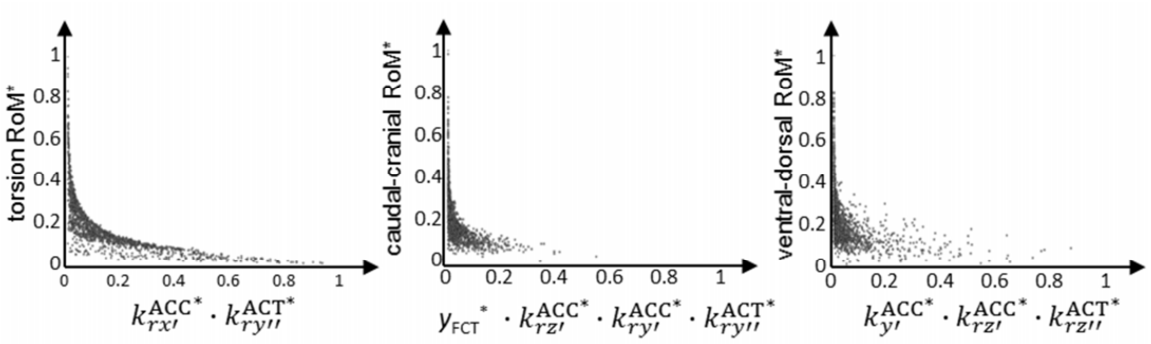


Figure 36: Scatter plot showing for each load-axis the relationship between the range of motion (RoM) and the parameter combination with the highest spearman correlation coefficient at the intact condition. Each dot represents a specific parameter combination. The values were non-dimensionalized (*) using the minimal and maximal values of each parameter. [154]; *[Reprinted with permission from Taylor & Francis]*

For example, according to this table, arbitrary combinations of parameter values for $k_{rx'}^{\mathrm{ACC}}$ between 1067 and 3799 Nmm/rad^2, as well as a $k_{ry''}^{\mathrm{ACT}}$ between 89 and 2524 Nmm/rad^2 result in an RoM in torsion between 20° and 25° for the intact condition. *(see [154])*

Table 8: Range of the parameter values which exhibited strongest sensitivity towards the specified RoM range (first column). In order to approximately obtain a desired mechanical response (RoM in first column), one may pick a combination of arbitrary parameter values, as long as these values are inside the ranges delimited by the corresponding min/max values. [154]

	RoM in °		$k_{rx'}^{ACC}$ in Nmm/rad^2		$k_{ry''}^{ACT}$ in Nmm/rad^2		$k_{ry'}^{ACC}$ in Nmm/rad^2		y_{FCT} in mm	
	min	**max**	**min**	**max**	**Min**	**max**	**min**	**max**	**min**	**max**
torsional load	5.4	10.4	972.4	19999.7	120.6	39885.0				
	10.4	15.3	951.0	15837.8	283.2	11617.0				
	15.3	20.2	1116.9	6710.8	18.3	5464.3				
	20.2	25.2	1067.2	3799.1	189.1	2524.5				
	25.2	30.1	1271.6	1703.2	314.1	1397.4				
caudal-cranial load	4.4	9.4	972.4	19999.7	120.6	39885.0	132.7	99997.3	18.4	40.1
	9.4	14.4	951.0	19781.6	18.3	36645.8	465.0	99906.5	18.4	38.8
	14.4	19.4	1480.9	11606.2	189.3	5404.9	675.9	98946.5	18.4	38.8
	19.4	24.3	1241.7	3727.5	190.4	9645.0	2808.8	84762.6	18.7	36.5
	24.3	29.3	1337.8	1435.7	314.1	433.1	28979.4	59795.8	18.7	22.6
			$k_{y'}^{ACC}$ in N/mm^2		$k_{rz'}^{ACC}$ in Nmm/rad^2		$k_{rz''}^{ACT}$ in Nmm/rad^2			
			min	**max**	**Min**	**max**	**min**	**max**		
ventral-dorsal load	2.6	5.4	0.1	14.7	2406.6	99834.9	115.5	39959.2		
	5.4	8.2	0.1	15.0	1004.2	99013.9	116.0	39726.5		
	8.2	11.0	0.1	6.6	482.4	33629.6	26.4	17841.9		
	11.0	13.7	0.1	4.6	428.2	11493.3	214.0	8024.7		
	13.7	16.5	0.4	1.3	3553.9	4955.4	520.4	924.0		

3.2.3 Material calibration algorithm

A parameter database was obtained from the parametric studies on the spinal segment and CVJ. They included information on how morphology and material parameters interact with the RoM. The parameter database included 432 parameter sets for the vertebral segments and 1487 parameter sets for the costovertebral joint. (*see* [152])

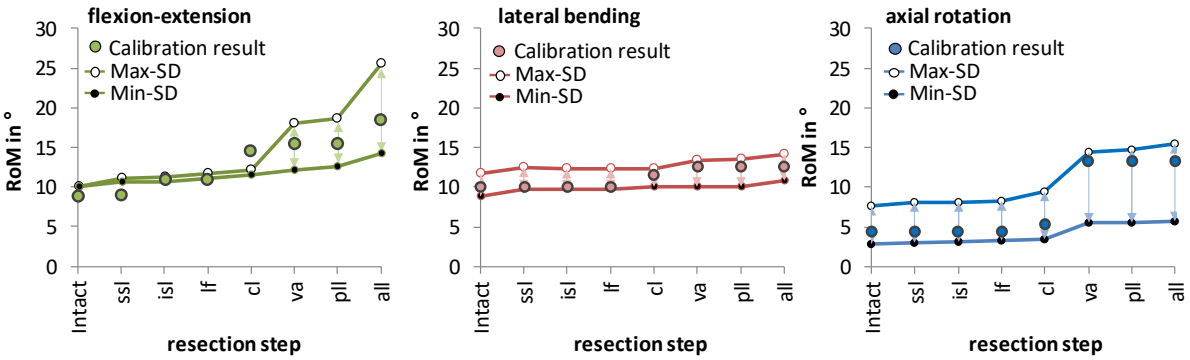


Figure 37: Exemplary result of the material calibration process for a vertebral segment L4-L5. A predefined reference RoM in combined flexion-extension of 10° was targeted. The coloured arrows indicate the RoM-region within the standard-deviation, obtained from the in vitro data from Heuer et al. [71], in flexion-extension, lateral bending and axial rotation at the seven resections steps. The encircled points indicate the obtained RoMs, after extracting the material properties from the database for the predefined reference RoM. [152]; [Reprinted with permission from Taylor & Francis]

Based on this database, the material properties were estimated to fit a targeted RoM of a joint in respect to its specific morphology.

This calibration process of the material properties considered each resection step and motion-axis, as illustrated in Figure 37.

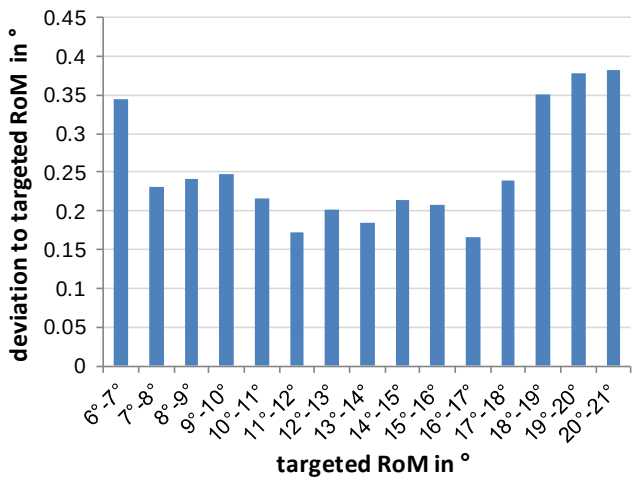


Figure 38: Deviation between trageted RoM and obtained RoM after material property extraction, depending on the magnitude of the targeted RoM of a verterbal segment.

In total, an average deviation of ±0.2° was estimated between the gained RoMs after the material property estimation and targeted RoMs between 6° and 21°. This is illustrated in Figure 38. The deviation relative to the targeted RoM generally increased towards the border RoM values (6° and 21°). This effect could be explained by the reduced amount

of data points at the outer RoM-limits within the database (see Figure 30).

This method was employed for each vertebral segment and costovertebral joint.

To create the full numerical model, the material properties were determined to fit to the RoM as listed in Table 9.

Table 9: Obtained RoM values of the vertebral segments and costo-vertebral joint. The ROMs refer to an applied pure moment of 2.5 Nm for the thoracic vertebral segment, 7.5 Nm for a lumbar vertebral segment, and 0.6 Nm for the costovertebral joint (CVJ). [153]

Vertebral segment level (*not for CVJ)	RoM of vertebral segment			RoM of costovertebral joint		
	flexion-extension	bending	Rotation	torsion	cranial-caudal	dorsal-ventral
T1 (-T2)*	8.0	7.6	8.9	40.6	13.7	8.6
T2-T3	7.7	9.6	8.6	35.9	12.7	8.0
T3-T4	6.4	8.9	7.7	31.2	11.7	7.4
T4-T5	6.1	11.3	8.8	26.5	10.7	6.7
T5-T6	6.9	10.2	7.7	21.8	9.7	6.1
T6-T7	5.1	8.6	6.4	23.5	11.8	8.6
T7-T8	4.7	8.7	6.6	25.1	13.9	11.2
T8-T9	4.3	8.4	5.7	26.8	16.0	13.7
T9-T10	5.1	7.8	5.9	28.4	18.1	16.2
T10-T11	4.9	5.2	5.0	28.4	18.1	16.2
T11 (-T12)*	4.2	5.3	3.8	28.4	18.1	16.2
T12 (-L1)*	8.6	11.7	8.7	28.4	18.1	16.2
L1-L2	7.6	10.4	7.7			
L2-L3	9.3	11.4	7.5			
L3-L4	8.1	10.2	6.1			
L4-L5	8.2	10.2	7.3			
L5-S1	7.9	7.4	6.3			

3.3 **Intrapleural pressure analysis**

Firstly, the influence of the IPP on the overall displacement and loads on the free moving spine, fixed at S1, was investigated. Secondly, to identify the influence of the IPP on the deformation of an upright spine, the lateral displacement of T1 in the x and y direction was additionally fixed.

Area of the pleural surface

The total surface of the pleura on the left side was 430 cm^2, and 437 cm^2 on the right side. The pleural surface area generally increased from T1 (10 cm^2) to T8 (60 cm^2) (Figure 39). The magnitude in deviation between the left and right pleural areas varied depending on the vertebral level, with a maximal deviation of -4.9 cm^2 at T9-T10. (see [153])

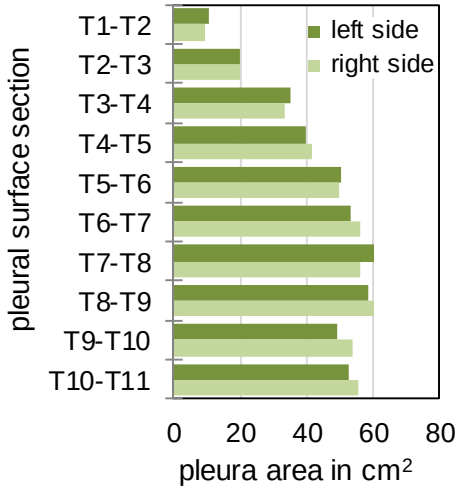


Figure 39: Pleural surface area calculated within sections defined by the vertebral levels. The pleural sections were defined by transverse planes which touched the posterior edge of the superior endplate of the vertebral bodies. [153]; [Reprinted with permission from Springer Nature]

Freely moving spine

The application of a constant pressure gradient of -6 $\frac{Pa}{mm}$, while fixing the spine at S1 only, predominantly caused a flexion of the spine (Figure 40). T1 was displaced in the sagittal plane by 50 mm and rotated in flexion by 11°. The spine also bent to the left side with a maximal deviation of 5 mm at T1.

A stepwise pressure gradient of -9 $\frac{Pa}{mm}$ below and -3 $\frac{Pa}{mm}$ above T6 increased the lateral bending of the spine to a displacement of 24 mm at T1.

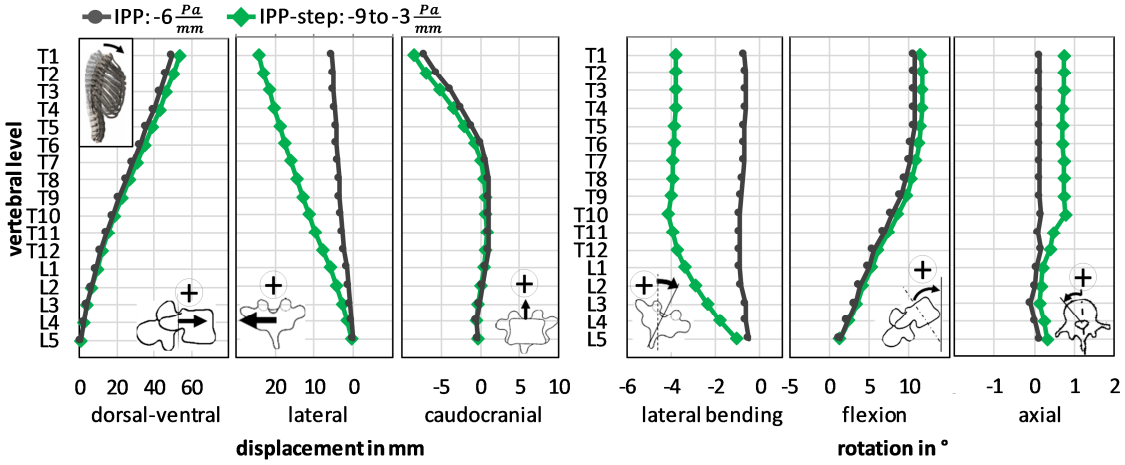


Figure 40: Displacement and rotation of the spinal vertebrae caused by a constant IPP gradient of -6 $\frac{Pa}{mm}$ (black) and by a stepwise gradient distribution (green) of -9 $\frac{Pa}{mm}$ below T6 and -3 $\frac{Pa}{mm}$ above T6. [153]; [Reprinted with permission from Springer Nature]

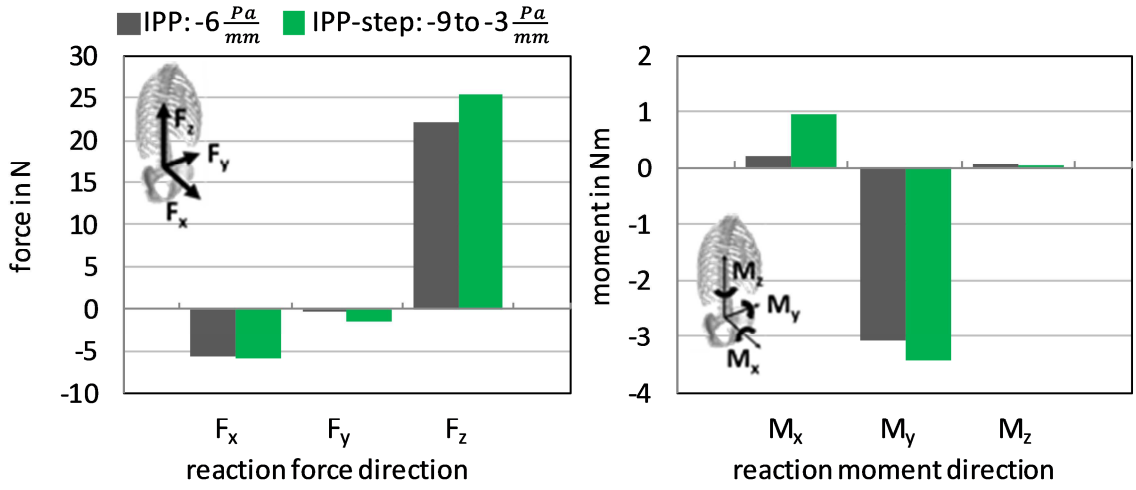


Figure 41: Reaction forces and moments acting at the base of the spine (S1). The load originates from a symmetrical intrapleural pressure distribution. [153]; [Reprinted with permission from Springer Nature]

While applying a constant IPP distribution of -6 $\frac{Pa}{mm}$, the reaction force at the base of the spine at S1 reached a magnitude of 22 N in the vertical direction (Fz) and a moment in flexion around the lateral (y) axis of 3.1 Nm (Figure 41). The stepwise IPP gradient generally increased the load on S1 in vertical direction to values of 25 N and a moment around the y-axis of 3.4 Nm.

The loads acting within the costovertebral joint of each rib were summarized at each rib level (Figure 42). Along the dorsal-ventral axis, the load vector pointed in the dorsal direction (-0.7 N) at rib 2. In the mid-thoracic region, the vector pointed in the ventral direction reaching its maximum of 2.4 N at rib 6. In the lateral direction, the orientation of the load vector also changed according to the rib level. While the load vector pointed

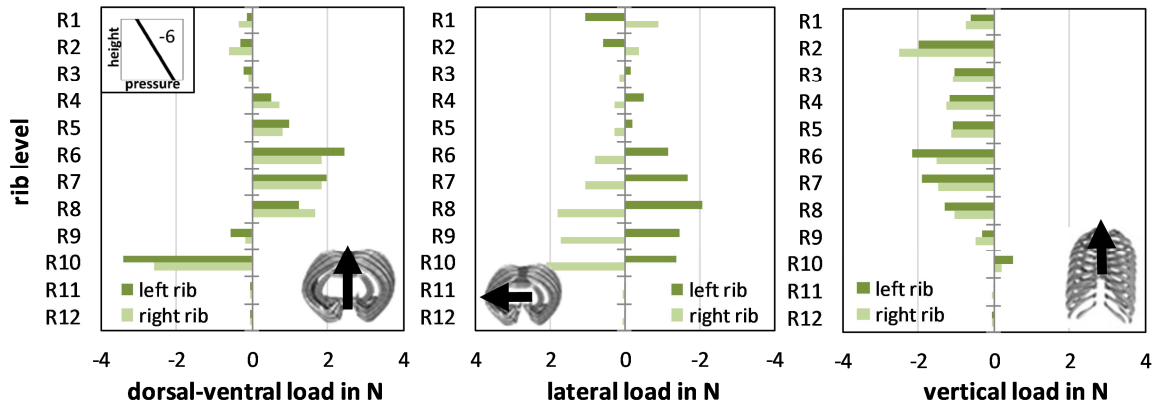


Figure 42 Forces that were transmitted from the ribs to the spinal segments at each rib level. A constant IPP distribution of -6 $\frac{Pa}{mm}$ was applied. [Reprinted with permission from Springer Nature]

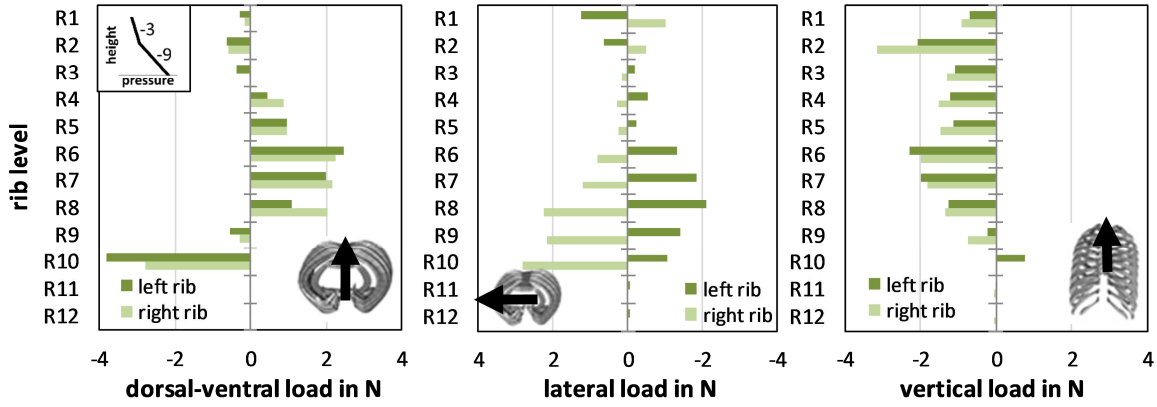


Figure 43: Forces that were transmitted from the ribs to the spinal segments at each rib level. A stepwise pressure gradient of -9 $\frac{Pa}{mm}$ below and -3 $\frac{Pa}{mm}$ above T6 was applied. [153]; [Reprinted with permission from Springer Nature]

away from the spine in the upper rib level bilaterally (max. -1 N at rib 1), the vector pointed towards the spine at rib level 3 to 10 (max. 2 N at rib 8). The highest vertical load was calculated at rib 2 with a maximum of -2.5 N. Despite an application of symmetrical pressure distribution, the vertical load was higher on the right side in the more cranial region, and on left side, higher in caudal region of the spine.

The application of a stepwise IPP gradient below and above T6 resulted in a similar load distribution compared to the constant IPP gradient distribution (Figure 43). Yet, the load magnitude generally increased while the deviation of the load between the left and right sides was more pronounced. (see [153])

Upright spinal posture

To investigate the influence of the IPP distribution on the deformation of the spine in an upright posture, the lateral displacement of T1 was additionally fixed. The influence of an asymmetrical IPP distribution was analysed by subtracting the displacements and rotations of the symmetrical condition from the asymmetrical condition.

Reducing the vertical IPP gradient on the right side from -6 $\frac{Pa}{mm}$ to -5 $\frac{Pa}{mm}$, resulted in a lateral deviation towards the right side with an apex at T11 (Figure 44). The lateral deviation went hand in hand with lateral bending of the spine, with an inflection point of the angle at T11. The vertebrae particularly rotated within the thoracic region around the axial axis towards the right side. Reducing the vertical IPP gradient on the left side caused

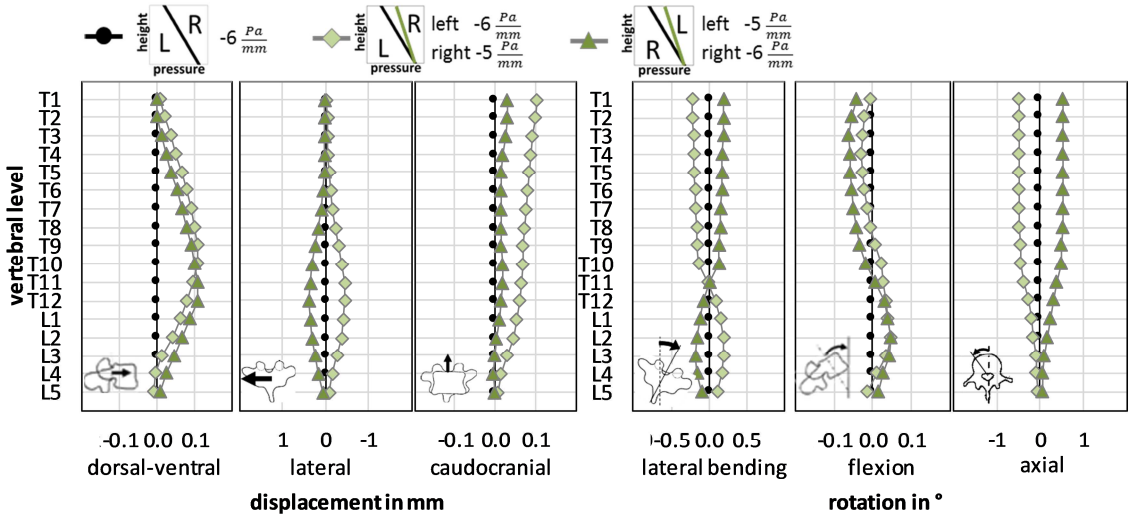


Figure 44: Displacement and rotation of the vertebral segments for an asymmetrical intrapleural pressure distribution, created by reducing the pressure gradient either on the left or the right side by -1 $\frac{Pa}{mm}$. Values represent deviation to the symmetrical pressure distribution (black). The arrows in the images indicate the positive direction of displacement and rotation. [Reprinted with permission from Springer Nature]

an opposite lateral displacement and axial rotation of the spine. In both cases, the asymmetrical IPP distribution resulted in a reduction of the kyphosis.

Furthermore, a deformation of the rib cage was obtained, as illustrated exemplary for the case of a reduced pressure on the right chest side in Figure 45. The posterior section of the right ribs displaced mainly dorsally, while the left rib exhibited a small displacement in ventral direction. The mid-point of the ribs moved in medial direction. Inducing an

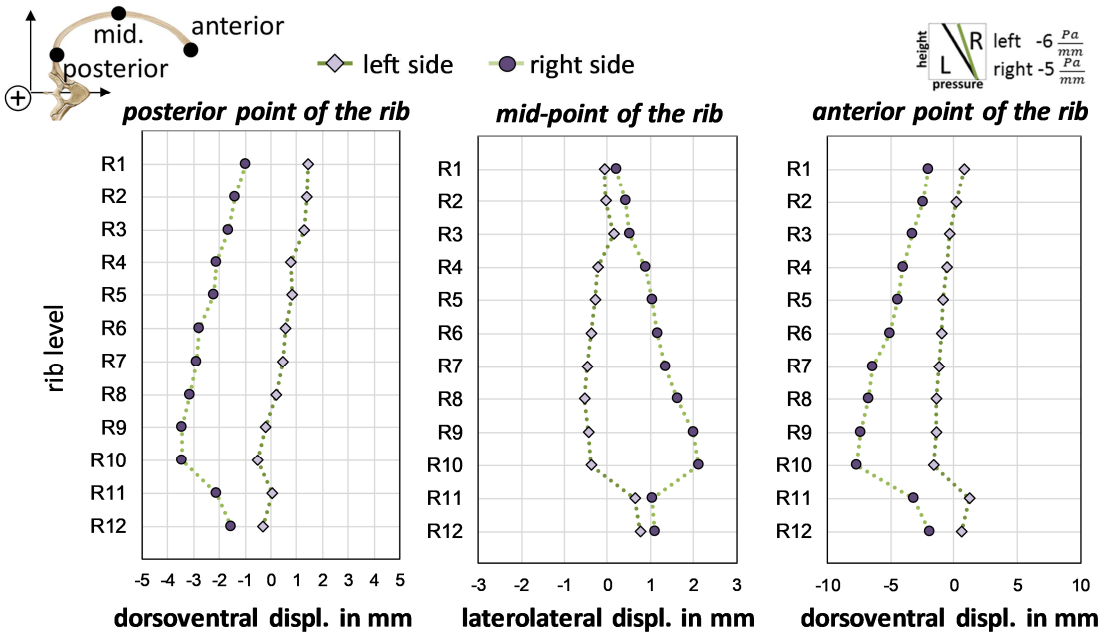


Figure 45: Displacement (displ.) of the ribs after applying an asymmetrical intrapleural pressure distribution, by reducing the pressure gradient either on the left or the right side by -1 $\frac{Pa}{mm}$ (green). The dark lines indicate the initial position of the different rib points.

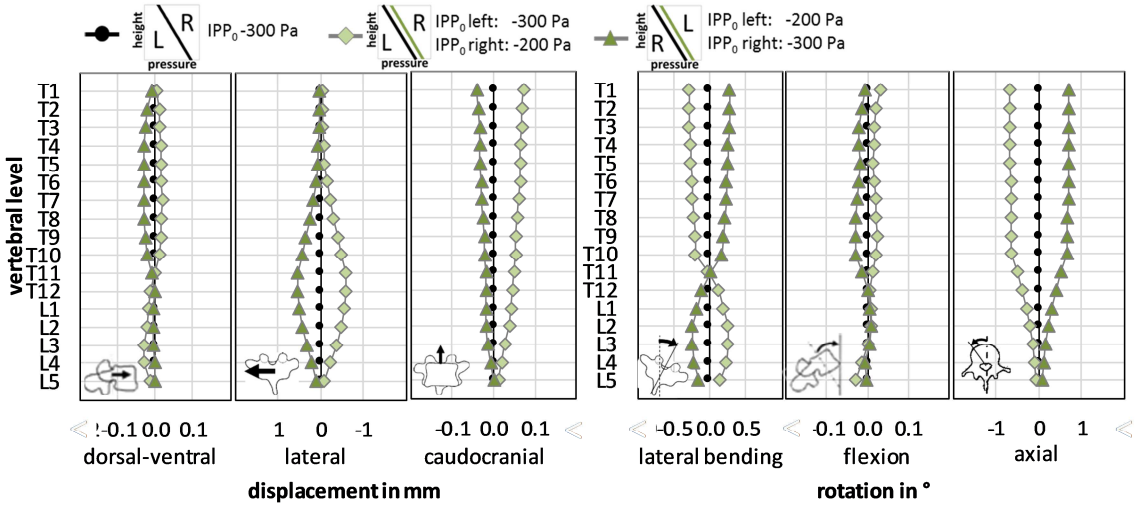


Figure 46: Displacement and rotation of the vertebral segments caused an asymmetrical pressure distribution created by reducing the base pressure either on the left or the right side by -100 Pa. All values relative to a symmetrical pressure distribution (black). The vertical IPP gradient was -6 $\frac{Pa}{mm}$ *in each case. [153]; [Reprinted with permission from Springer Nature]*

asymmetry by altering the absolute IPP base on one side from -300 Pa to -200 Pa generally resulted in a similar deformation of the spine (Figure 46). Differences were obtained in dorsoventral displacement and the flexion angle. A reduction of both parameters was obtained, which demonstrated an almost linearly distributed along the spine.

Removing the IPP unilaterally within different sections depicted the specific influence of IPP in these regions on the deformation of the spine (Figure 47). In particular, the

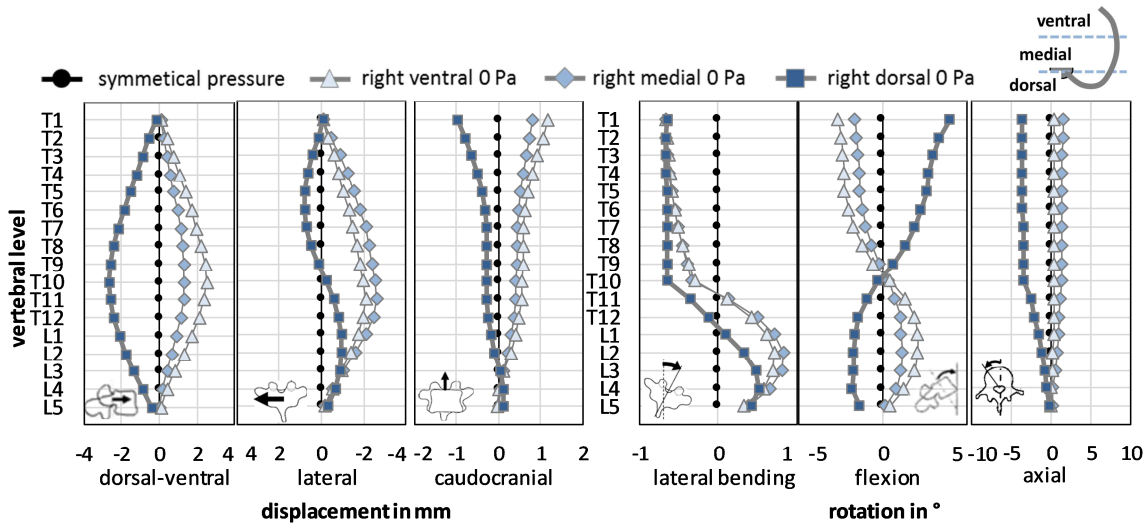


Figure 47: Displacement and rotation of the vertebral segments while removing the IPP in three different coronal sections within the right hemithorax: ventral, medial and dorsal section. Values relative to a symmetrical IPP distribution between left and right hemithorax [153]; [Reprinted with permission from Springer Nature]

presence of pressure in the dorsal region had a strong influence on the magnitude of rotation of the vertebrae. Removing the IPP on the right dorsal site resulted in a lateral deviation towards the left side in the upper thoracic region and to the right side in the lower thoracolumbar region. In contrast, removing the pressure in the right medial or ventral region resulted in a lateral deviation to the right side. The axial rotation of the vertebrae was most pronounced at removing the pressure in the dorsal region, with a maximal rotation of 3.7° at T1. (see [153])

4. Discussion

To investigate the biomechanics of scoliosis, a fully parametric FE model of the spine including the rib cage was developed. The influence of an asymmetry in the intrapleural pressure distribution on the spinal shape was investigated with the use of this model. The obtained results suggest that the IPP distribution may have a strong effect on the spinal deformity. Furthermore, deformation patterns similar to those seen in patients with an adolescent idiopathic scoliosis could be identified.

4.1 Morphology analysis

The analysis of the CT data of patients suggests that the development of morphological parameters along the spine depict a characteristic pattern which reveals a distinct load path prevalent within scoliotic spines. The deformation of the spine relative to the sagittal plane of symmetry appears to go hand in hand with multiple changes within the bone morphology.

It should be noted that also the spines of the healthy group, classified as non-scoliotic, exhibited an inherent deformation and rotation of the spine which qualitatively matched those found in scoliotic spines. These findings correspond to data measured by Kouwenhoven et al. [92], who also identified significant rotation of up to 2.7° of the vertebrae within the thoracic region of healthy patients.

The measurement of an increased length of the anterior column of scoliotic spines compared to healthy spines agrees with previous studies: the comparison of the anterior spinal length with the length of the spinal canal [143, 146], as well as the increased anterior to posterior vertebral body height [132]. However, these results do not present any evidence that scoliosis is primarily *caused* by a growth-disturbance or tethering of the spinal canal. The presence of a morphological pattern within scoliotic spines suggests, rather, a natural adaption process of the bone.

The observed increased spinal length and, concomitant, the reduced endplate area in scoliotic spines in comparison with the healthy control group might be explained by the Hueter-Volkmann Principle [75, 177] and Wolff's Law [190]. The latter would suggest that in a straight healthy spine the size of an endplate area would correlate to the axial load to which the vertebra is subjected. Should the magnitude of the axial load be independent

of the shape of the spine, the size of the endplate area would not be significantly altered in scoliotic spines. The results indeed suggest that size of the endplate area is normal in patients with AIS, yet, the spinal length is increased. According to the Hueter-Volkmann Principle [166, 167], an increase in the axial compression load would result in an decrease in the height of the bone. This concurs with the observed wedging of the vertebral body, as well as the size differences between the right and left facet areas and pedicle sizes in AIS. The latter also suggests an uneven load sharing between and within the anterior and posterior column. The pedicle size between the left and right sides deviates mainly at the apex of the scoliotic curvature, while the facet size varies predominately in the region of the inflection point of the curvature (Figure 48).

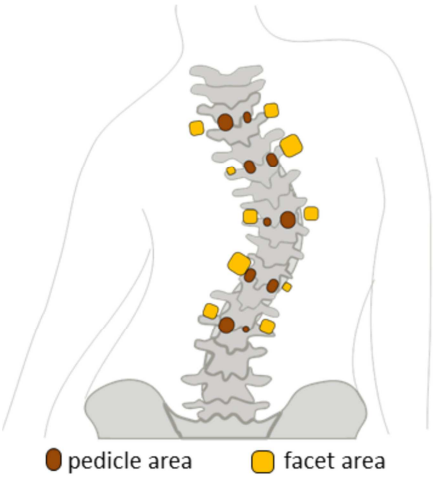


Figure 48: Qualitative sketch of the variation of the pedicle and facet area size along a scoliotic curvature. [151]; [Reprinted with permission from Taylor & Francis]

These findings suggest that the concave site of the vertebral bodies in the region of the apex is subjected to higher loads. The site of loading on the articular facets changes above and below the apex. (*see* [151])

Limitations of the morphology analysis

This study was mainly limited by the rather small patient number. Due to ethical concerns, CT images of high quality which cover the entire thoracic and lumber spine including the chest are rarely taken. This makes the analysed images within this study an exceptional database.

Sources of error include the placement of the landmarks, particularly those on the scoliotic vertebrae, since the selection of the right, left and anterior vertebral edges on strongly distorted vertebrae proved to be challenging. These errors, however, should be captured by the quantified inter- and intra-rater variability. (*see* [151])

Due to the distinct correlation between deformation and multiple morphological changes, the deformation of bony structures may very well be secondary, caused by inherent loads deforming the spine and triggering scoliotic changes.

4.2 Finite element model of the spine and chest

An FE-model generator was developed which allowed for the consideration of a subject-specific morphology and RoM of the spine (T1-S1) and rib cage by using distinct parameters. Prior to identifying the influence of material properties and morphology on the RoM, an uncertainty study was performed on the spinal segment and CVJ.

4.2.1 Spinal segment

Distinct material parameters of a spinal segment which had a strong effect on the RoM of the segment were identified. These were, in particular, the properties of the annulus fibrosus, the gap size between the articulating surfaces of the facet joints and the property of the ISL. (*see* [152])

The overall selected parameter ranges appeared adequate, as they resulted in a similar RoM response at each resection step as found in the *in vitro* experiments of Heuer [71]. Deviations between the numerical and *in vitro* data may be affected by morphological differences, such as the disc height [133], which were not considered in this study. The high degree of uncertainty in the material properties published in the literature led to a correspondingly wide scatter in the RoM of the spinal segment. Therefore, a single set of material parameter combinations cannot reflect the broad range of spinal response nor can this explain the impact of a specific structure on the flexibility of the spinal unit. Niemeyer [133] estimated that the natural variability of the morphology may explain a variation in the RoM of 4° in flexion and extension, 3° in lateral bending and 1.5° in axial rotation. In contrast, the impact of the material parameters investigated in this study resulted in RoM differences which were nearly twice as high.

The data suggested that the intervertebral disc properties have a strong impact on the stiffness of a spinal unit. The variation in the collagen fibre angle seemed to be weakly correlated with the overall RoM, yet the orientations of these fibres may be important for local stress distribution within the annulus fibrosus [120].

The gap between the articular facets is a parameter which is difficult to determine from a radiograph or CT scan and also depends on the spinal posture. However, the sensitivity analysis revealed a major influence of this parameter on spinal flexibility. Facet gaps between approximately 1.3 mm and 2.4 mm resulted in RoMs that are comparable to those measured *in vitro*, and which also agree with the facet gap thickness measured *in vivo* [163].

The relative change of the RoM by varying the ISL properties during flexion did not correspond to the *in vitro* data of Heuer [71], who identified only a minor influence of this structure. This discrepancy may be due to multiple factors. Firstly, the stiffness of a ligament may depend on the vertebral level, whereas Heuer solely considered an L4-L5 segment. The stiffness properties on isolated ISL *in vitro* were obtained from multiple vertebral levels [30, 72]. Thus, the chosen parameter ranges for the ISL in this study which were extracted from the literature, may have been too high. In addition, the orientation of the collagen fibres were modelled in cranial-caudal direction, while the orientation may differ within segments *in vitro* [150]. The impact of the ISL may be more pronounced at other loading conditions which were not performed in the *in vitro* experiments.

In conclusion, the performed statistical analysis of the variability within parameter values might help to estimate the sensitivity and total uncertainty which propagate through biomechanical simulations. This variability can affect the reliability of the predictions.

4.2.2 Costovertebral joint

The impact of the variability of material and morphology parameters on the stiffness of a CVJ was investigated. The chosen model and selected parameter ranges were adequate, as they resulted in a similar RoM found in the *in vitro* experiments performed by Lemosse [104].

The main challenge of modelling the CVJ lies in its complexity. It consists of two synovial joints and multiple ligaments connecting the rib to the spine. Previous numerical models reduced the CVJ to a single joint element and neglected the various load paths from the rib to the spine. In this study, however, an approach is presented which considered the

main load sharing paths of the CVJ between rib and vertebral body, rib and transverse process, as well as the rib and cranial vertebra.

The sensitivity analysis exhibited that only few parameters strongly correlated with the RoM. These parameters were the rotational stiffness of the ACC around the torsion axis, the rotational stiffness of the ACT, and the lateral position of the FCT. The LCTS properties showed weak correlation with the RoM, which corresponds to the *in vitro* data of Lemosse et al. This was a surprising result, since a biomechanical impact of the LCTS could be expected. However, low correlation values do not necessarily mean that the influence of the material properties can be neglected: The correlation of a material property with the RoM can be affected by the chosen parameter-value range, further loading conditions, as well as the resection step sequence.

The complexity of the numerical model was limited by the small amount of experimental data on the mechanics of the CVJ published to date. This information is necessary for the calibration and validation of a CVJ model. The accurate representation of the biomechanics of the CVJ is relevant for the load transmission between rib cage and spine. This is necessary for the simulation of respiratory mechanics or for the influence of brace treatment on the shape of the spine.
This parametric study provides data that can help identify important morphology and material parameters necessary for the creation of an adequate numerical model of the CVJ. *(see [154])*

4.2.3 Material calibration algorithm

The methodology for estimating material parameters based on morphology and predefined RoM, which was based on the database obtained from the uncertainty analysis, generated adequate results within the predefined parameter range. An accuracy of 0.2° is adequate as it lies within the accuracy of the experimental measurement of the RoM *in vitro* of approximately 1° [188]. The deviation between the expected RoM and the obtained RoM generally increased towards the border regions of the reference RoM, since the database did not include sufficient data points within this region. The accuracy

for determining the material properties based on a given RoM in flexion-extension and morphology, depended on the size and quality of the database. The accuracy of obtaining predefined RoM values could be improved by increasing the parameter database and improving the material extraction algorithm (e.g. response surface methodology instead of nearest-neighbour).

The primary advantage of identifying the material properties based on the parameter-database is that the stiffness properties can be automatically obtained and rapidly modified. This allows for the estimation of an error and uncertainty range during biomechanical simulations of the spine. In addition, new research data obtained from *in vivo* and/or *in vitro* studies could be considered in the numerical model. (*see* [152])

4.3 Intrapleural pressure analysis

The numerical results suggest that the IPP may have a strong effect on the shape of an erect spine. The IPP can induce forces via the rib cage which are non-linearly distributed and cause a displacement and rotation of the spine.

The direction and magnitude of the deformation of the spine were dependent on the distribution and magnitude of the IPP. The simulation of a symmetric IPP distribution on the left and right hemithorax resulted in an asymmetrical deformation of the spine out of the sagittal symmetry plane. This asymmetry could be explained by the asymmetrical load distribution along the spine. However, the surface area, and therefore the total load, was only slightly higher on the right side. Thus , it is assumed that the asymmetry is caused by an asymmetrical shape of the chest wall between the left and right chest side, and slight misalignment of the spine within the CT. Applying the stepwise pressure gradient (-9 $\frac{Pa}{mm}$, -3 $\frac{Pa}{mm}$) increased the asymmetry, since the total pressure is higher compared to the linear IPP gradient case (-6 $\frac{Pa}{mm}$).

The simulation of an asymmetrical IPP distribution between a left and right hemithorax resulted in a lateral deformation towards the side of reduced pressure. The estimated deformation patterns were most comparable to those seen in patients with thoracolumbar scoliosis (Figure 49). General differences between the simulated results and morphological characteristics of scoliotic spines are reasonable since the simulation

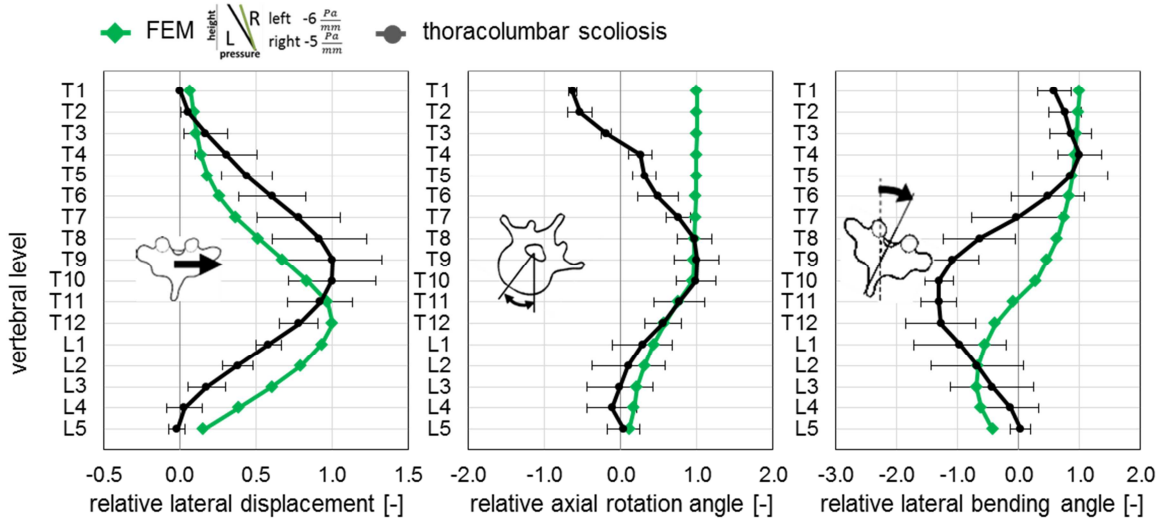


Figure 49: Exemplary comparison between FEM results and data obtained from patients with a thoracolumbar AIS. Displacement and rotation parameters were calculated relative to the minimal value. [153]; [Reprinted with permission from Springer Nature]

considered neither muscle forces nor tissue adaptation processes. Better approximation towards the scoliotic curvature types could be expected once considering these aspects. (*see* [153])

Clinical aspect on pleural scoliosis

An important aspect which has been widely neglected in aetiology debates of AIS involves the stresses which arise within the rib cage. Clinical studies reported that interventions affecting the pleura were closely related to deformations of the spine, notably scoliosis. The secondary formation of pleural scoliosis depends on the surgical intervention which also influences the risk for developing scoliosis. Spinal deformations can also develop secondarily either due to pneumonectomy (risk: 90%) [79], chest wall resection/thoracoplasty (risk: 67-99%) [39, 44, 60, 85, 115], thoracotomy (risk: 40-50%) [19, 32, 47] or organ (heart) transplantation (risk: 22%) [29, 45]. Adolescents are generally considered to be at higher risk to develop scoliosis after surgery compared to mature patients [19, 39, 47, 68, 85, 164]. Rib resections above the 6th rib [60], as well as resections, particularly of the posterior part of the ribs, were also described as risk factors for scoliosis [39].

The assumption that asymmetrical pressures and stresses which arise within the rib cage can induce scoliosis had already been hypothesized at the beginning of the 20th century. In 1934, Bisgard compared anatomical characteristics of pleural and idiopathic scoliosis in

512 patients [20]. With the available technology of the time, he identified that in contrast to patients diagnosed with idiopathic scoliosis, patients with pleural scoliosis had only a slight rotation of the vertebra, an absence of a rib hump, and a deviation of the mediastinum and short and sharply angulated spinal curves. However, a mechanical link between the stresses within the rib cage and the occurrence of scoliosis has not yet been established.

The spinal morphology of patients who developed scoliosis after pleural interventions were not investigated within this study. Since the bone is mature within these patients, the disc potentially adapts more to the altered load situation than the bone. This would explain the sharply angulated spinal curve in patients with a pleural scoliosis, compared to the curvature observed in AIS.

The assumption that the pathology of the IPP is related to the occurrence of scoliosis is supported by the reported risk factors for the development of scoliosis. Rib resections above the 6^{th} rib are described as risk factors for scoliosis which corresponds to the region where the IPP acts along the chest wall [60]. A further risk factor are rib resections in the dorsal region [39]. The results of this study support this assumption, since the absence of the IPP on one side in the dorsal region had the strongest impact on the vertebral rotation. In comparison, the absence of pressure in medial and ventral regions mainly contributed to the lateral displacement of the spine.

After unilateral pneumonectomies, the pleural cavity is absent at the site of pneumonectomy, and therefore, the IPP as well. The IPP should now act only on the non-resected site which would imply a spinal deformation to the side of the resected lung. Interestingly, a pneumonectomy causes spinal deformation away from the side of the resection. According to the obtained results, two factors could explain this phenomenon. Either, a pneumonectomy provokes a cicatrisation which causes more negative stress on the chest wall on the resected side. Or, a more ventral load still acts on the chest wall after the lung has been resected. The latter would explain a lateral deformation without a vertebral rotation. (*see* [153])

Weight distribution and scoliosis

It is assumed that the weight of the intrathoracic and abdominal organs is also counterbalanced by the IPP and recoil force of the visceral pleura. This would imply that the reaction load of the spine caused by the IPP should be within the same order of magnitude as the weight of the organs. The summation of the mean weight of the heart (0.33 kg), the lungs (0.84 kg), the liver (1.56 kg) and spleen (0.14 kg) results in a total mean weight of 2.88 kg (general range: 1.46-5.16 kg) [126, 127]. The calculated vertical load of 22 N approximately corresponds to 2.2 kg. Thus, the organ weight and reaction load are within the same order of magnitude despite the strong standard-deviation in the weight of organs, the uncertainty of exact IPP values, and further possible weight-bearing structures, such as ligaments connecting the organs directly to the chest/sternum.

Assuming that, firstly, the organ weight is proportional to the magnitude of the IPP at the end of expiration, and secondly, the IPP induces forces which deform the spine, an asymmetrical organ weight distribution would result in a deformation of the spine. This is particularly the case if the load cannot be compensated, for example by muscle forces of the spine. A correlation between asymmetrical weight (density) distribution and spinal deformation within the thorax has already been reported in the literature [92].

Whether an asymmetrical IPP distribution plays a key role in the formation of idiopathic scoliosis is not known to date. This is especially due to the challenges in measuring the IPP distribution *in vivo*. The simulations suggest, however, that the forces emanating from an asymmetrical IPP distribution may trigger *in vivo* the deformation of the spine. Possible explanations for such an asymmetric IPP distribution may be an asymmetrical organ weight distribution and variations in the amount of intrapleural fluid (e.g. pleural effusion). Furthermore, potential structures such as tendons and muscles which usually compensate the forces emanating from the rib cage, may be abnormal in scoliotic patients.

The interaction between intrapleural and intraabdominal pressure (IAP) would be a further interesting aspect to consider. These two pressure regions are separated by the diaphragm, where they most likely interact. The IPP and the IAP values also lie within the

same order of magnitude at the end of expiration (approximately 400 Pa) [125]. According to the results, the IPP can potentially reduce the stability of the spine by inducing a deformity. In contrast, it is thought that the IAP increases the stability of the spine [73]. The occurrence of scoliosis secondary to the prune-belly syndrome, in which the abdominal muscles (and most likely the IAP) are reduced, might indicate a correlation of IAP, IPP and scoliosis [99].

Limitations of the IPP analysis

The modelled IPP distribution was deduced from published experiments which were mainly performed on dogs. The IPP distribution in humans might vary in magnitude and distribution in both vertical and lateral directions along the surface of the lung. Yet, a general similarity between the IPP distribution in dogs and humans can be assumed since the esophageal pressure gradients and pleura surface pressure gradients measured in humans are comparable to the values measured in dogs [171]. It should be noted that no explicit study which focused on a potential asymmetrical IPP distribution within subjects could be found in the literature. Due to the inherently asymmetrical anatomy of humans and limited published data, it is likely that an asymmetry in the IPP exists.

The determination of the exact *in vivo* or even *in vitro* material properties of an individual spinal segment remains a great challenge, since these properties cannot be measured directly and can, therefore, only be approximated. Thus, the calculated deformations of the spine should only be considered as an estimation. In addition, the model was generated from a patient in the supine posture. The shape of the spine alters once the patient is upright which may change the magnitude of spinal deformation. Not lying perfectly straight in the CT may also affect the alignment of the chest in the model and load distribution. (*see* [153])

4.4 **Outlook**

4.4.1 Numerical model of the spine and chest

The developed parametric FE model of the spine and chest may be a powerful tool to investigate various biomechanical conditions of the spine and thorax. Currently, the

programme enables the generation of models of the thorax that can consider a broad range of physiological and scoliotic curvatures and chest shapes. Furthermore, the stiffness of the each spinal segment and CVJ can be adapted. The validity of chest biomechanics could be further improved by calibrating the motion of the complete rib cage using *in vitro* data.

As a next step, instrumentation techniques may be implanted within the model to simulate surgical interventions. This would enable the investigation and optimization of the treatment and correction of spinal deformities. The model of the instrumentation could be verified, using for example *in vitro* experiments that deal with various fusion techniques.

An ultimate goal would be the simulation of spinal deformities under physiological conditions, such as an erect posture that considers gravitational loads. This could give, for instance, insight into local stress distribution along the spine, which may explain the asymmetrical bone formation seen in AIS.
To achieve this, the mechanics of the spinal muscles as well as the intrinsic load distribution need to be considered within the model. Despite emerging publications using multi-body models to simulate muscle forces of the spine, there remains a great lack of knowledge on muscle mechanics and regulation of the upright spine. Furthermore, the anatomical correct representation of the gravitational loads and the load-bearing of the thorax has been neglected in past biomechanical models.
In this thesis, important fundaments for generating an adequate biomechanical model of the spine and chest, which considered gravitational loads, have been elaborated.

4.4.2 Aspects on an asymmetry in the intrapleural pressure

The resulting hypothesis of this thesis that an asymmetry in the intrapleural pressure distribution between left and right sides triggers the development of scoliosis requires verification, clinically as well as experimentally.

A clinical approach to investigate the existence of an asymmetrical IPP within patients with scoliosis requires the development of a non-invasive method to measure the IPP.

According to literature, increased amount of fluid (pleural effusions) may also be an indicator for an alteration of the IPP. Therefore, clinical studies could additionally focus on the amount of pleural fluid and thickness of the interpleural gap within scoliotic patients.

An asymmetry in the IPP distribution could also exist even if the amount of intrapleural fluid appears normal. The asymmetrical pressure distribution may then be triggered by an asymmetrical weight distribution of the intrathoracic organs, such as a misalignment of the heart.

Furthermore, the presence of an asymmetrical IPP within humans might be non-pathological. In such cases certain spinal structures which usually counterbalance these asymmetrical forces may be abnormal and lead to the development of scoliosis.

The investigation of the IPP experimentally is very challenging, since the reproduction of the complex pleural physiology in a test setup is difficult.

Improvements to the numerical model that mirror the *in vivo* situation would need to include bone adaptation and the muscles.

Identifying the IPP as a possible causative factor for the development of idiopathic scoliosis may have a major impact on its treatment. Currently this is not addressed.

Presently, the treatment is symptomatic: addressing muscle balance with physiotherapy and straightening of the curved spine surgically. Both treatment options most likely do not alter the IPP. Brace treatment might indeed counterbalance the asymmetrical IPP distribution by applying opposite forces to the outer surface of the rib cage. The brace should then should be worn as long as the asymmetrical inner stresses act.

Surgical correction and subsequent fixation of the spinal curvature aim to restrain the spine. Yet, the asymmetrical loads would still act on the treated spine, which may lead to a postoperative deformation and loosening of the fixation devises.

Spinal deformities caused by an asymmetrical IPP distribution might only be sustainably treated by directly addressing the intrapleural physiology.

5. Summary and Conclusion

The aetiology of scoliosis during adolescence is in most cases (85%) unknown (idiopathic). To investigate potential causes and treatments of scoliosis, a fully parametric finite element model of the spine and chest was developed. This work investigated the principle hypothesis that adolescent idiopathic scoliosis (AIS) is triggered by an asymmetrical load distribution resulting in a malformation of the bone. Furthermore, the impact of a potential asymmetry in the intrapleural pressure (IPP) distribution on the spinal shape was explored.

The biomechanical aspect of the hypothesis was analysed using a subject-specific numerical model of the human spine (levels: T1-S1) and rib cage of a healthy 13-year-old male. The finite element model was generated using a self-developed program which allows a rapid semi-automatic generation of numerical models that consider the patient-specific morphology and a predefined flexibility of the main joints. The material properties of the soft-tissue were primarily extracted from literature. The material properties of the spinal segments and costovertebral joints were further optimized to fit the specific range of motion obtained from *in vitro* tests.

In view of the close relationship between the form and function of the skeleton, the bone morphology of the spine and chest was quantified using CT data of individuals. The comparison of the bone morphology of patients, with (n = 21, 15 ± 2 years) and without (n = 48, 23 ± 12 years) AIS, revealed a characteristic morphological pattern in patients with AIS. This pattern included wedging and rotation of the vertebral bodies, differences between the right and left pedicle and facet size, as well as, asymmetrical rib cage deformities. This indicates the presence of an inherent asymmetrical stress distribution along the scoliotic spine. It should be noted, however, that in the non-scoliotic patient group a predisposition towards a characteristic scoliotic curvature was on average also observed.

Simulations of various assumed intrapleural pressure distributions suggest that an asymmetrical intrapleural pressure can lead to spinal deformation patterns comparable

to those seen in scoliotic spines. In particular, the pressure within the dorsal section of the rib cage had a strong influence on vertebral rotation, whereas the pressure in medial and ventral regions demonstrated a lateral displacement. An asymmetrical pressure between the left and right hemithorax resulted in lateral deviation of the spine towards the side of the reduced magnitude of negative pressure.

The application of the IPP, assumed within the numerical model, resulted in a compressive force of 22.3 N in craniocaudal direction of the spine, which corresponds to 2.3 kg of organ weight. This reaction force supports the assumption that the IPP contributes in counterbalancing the weight of the intrathoracic organs.

Due to the current lack of a non-invasive method to measure the IPP *in vivo*, clinical verification of the influence of the IPP on spinal stability remains unclear and challenging. It is known, however, that scoliosis can develop secondarily to surgical interventions of the pleura.

In conclusion, the results of this study suggest that the intrapleural pressure distribution has the potential to play a key role in the development of spinal deformities. The interaction between the pleural physiology and the thorax may be an important piece in the puzzle to further understand the biomechanical *in vivo* condition and explain various spinal pathologies. Furthermore, the developed numerical model is suitable to simulate the biomechanics of the spine and chest. It can be a useful tool to investigate various spinal pathologies and treatment strategies.

6. Literature

1. Adams M a, McNally D S, Dolan P: „Stress“ distributions inside intervertebral discs. The effects of age and degeneration. J Bone Joint Surg Br 78: S. 965–72 (1996)
2. Agostoni E: Mechanics of the pleural space. Physiol Rev 52: S. 57–128 (1972)
3. Agostoni E, D’Angelo E: Thickness and pressure of the pleural liquid at various heights and with various hydrothoraces. Respir Physiol 6: S. 330–342 (1969)
4. Agostoni E, D’Angelo E, Roncoroni G: The thickness of the pleural liquid. Respir Physiol 5: S. 1–13 (1968)
5. Agostoni E, Miserocchi G, Bonanni M V: Thickness and pressure of the pleural liquid in some mammals. Respir Physiol 6: S. 245–256 (1969)
6. Agostoni E, Mognoni P, Torri G, Miserocchi G: Forces deforming the rib cage. Respir Physiol 61: S. 105–117 (1967)
7. Andriacchi T, Schultz A, Belytschko T, Galante J: A model for studies of mechanical interactions between the human spine and rib cage. J Biomech 7: S. 497–507 (1974)
8. Arjmand N, Gagnon D, Plamondon a., Shirazi-Adl a., Larivière C: A comparative study of two trunk biomechanical models under symmetric and asymmetric loadings. J Biomech 43: S. 485–491 (2010)
9. Ashley G: The relationship between the pattern of ossification and the definitive shape of the mesosternum in man. J Anat (1956)
10. Ashman R B, Cowin S C, Van Buskirk W C, Rice J C: A continuous wave technique for the measurement of the elastic properties of cortical bone. J Biomech 17: S. 349–361 (1984)
11. Aubin C E, Dansereau J, Parent F, Labelle H, de Guise J a: Morphometric evaluations of personalised 3D reconstructions and geometric models of the human spine. Med Biol Eng Comput 35: S. 611–8 (1997)
12. Aubin C E, Labelle H, Chevrefils C, Desroches G, Clin J, Eng A B M: Preoperative planning simulator for spinal deformity surgeries. Spine (Phila Pa 1976) 33: S. 2143–52 (2008)
13. Aubin C-E, Labelle H, Ciolofan O C: Variability of spinal instrumentation configurations in adolescent idiopathic scoliosis. Eur Spine J 16: S. 57–64 (2007)

14. Banchero N, Schwartz P E, Tsakiris A G, Wood E H: Pleural and esophageal pressures in the upright body position. J Appl Physiol 23: S. 228–234 (1967)
15. Bar-Yishay E, Hyatt R E, Rodarte J R: Effect of heart weight on distribution of lung surface pressures in vertical dogs. J Appl Physiol 61: S. 712–8 (1986)
16. Beyer B, Sholukha V, Dugailly P M, Rooze M, Moiseev F, Feipel V, Van Sint Jan S: In vivo thorax 3D modelling from costovertebral joint complex kinematics. Clin Biomech 29: S. 434–438 (2014)
17. Beyer B, Van Sint Jan S, Chèze L, Sholukha V, Feipel V: Relationship between costovertebral joint kinematics and lung volume in supine humans. Respir Physiol Neurobiol 232: S. 57–65 (2016)
18. Bick E M, Barash E S, Lehman L: Congenital scoliosis without vertebral anomaly; the vertebral histology of two cases. Clin Orthop 12: S. 285–290 (1958)
19. Van Biezen F C, Bakx P A, De Villeneuve V H, Hop W C: Scoliosis in children after thoracotomy for aortic coarctation. J Bone Joint Surg Am 75: S. 514–518 (1993)
20. Bisgard J: Thoracogenic scoliosis: influence of thoracic disease and thoracic operations on the spine. Arch Surg 29: S. 417–445 (1934)
21. Brasiliense L, Lazaro B, Reyes P: Biomechanical contribution of the rib cage to thoracic stability. Spine (Phila Pa 1976) 36: S. E1686–E1693 (2011)
22. Braune W, Fischer O: Über den Schwerpunkt des Menschlichen Körpers mit Rücksicht auf die Ausrüstung des Deutschen Infanteristen. . Leipzig, S. 160 (1890)
23. Brickley-Parsons D, Glimcher M J: Is the chemistry of collagen in intervertebral discs an expression of Wolff's Law? A study of the human lumbar spine. , *Spine*, 9: . S. 148–63 (1984)
24. Brink R C, Schlösser T P C, Colo D, Vavruch L, Van Stralen M, Vincken K L, Malmqvist M, Kruyt M C, Tropp H, Castelein R M: Anterior Spinal Overgrowth Is the Result of the Scoliotic Mechanism and Is Located in the Disc. Spine (Phila Pa 1976) 42: S. 818–822 (2017)
25. Cammarata M, Aubin C-É, Wang X, Mac-Thiong J-M: Biomechanical risk factors for proximal junctional kyphosis: a detailed numerical analysis of surgical instrumentation variables. Spine (Phila Pa 1976) 39: S. E500-7 (2014)
26. Cappello M, De Troyer A: Role of rib cage elastance in the coupling between the abdominal muscles and the lung. J Appl Physiol 97: S. 85–90 (2004)

27. Carter D R, Beaupré G S: Skeletal function and form: mechanobiology of skeletal development, aging, and regeneration, 296: . Cambridge University Press, (2001)
28. Carter O D, Haynes S G: Prevalence rates for scoliosis in US adults: results from the first National Health and Nutrition Examination Survey. Int J Epidemiol 16: S. 537–544 (1987)
29. Ceroni D, Beghetti M, Spahr-Schopfer I, Faundez A, Kaelin A: Corrective surgery for idiopathic scoliosis after heart transplantation. Eur Spine J 10: S. 454–457 (2001)
30. Chazal J, Tanguy A, Bourges M, Gaurel G, Escande G, Guillot M, Vanneuville G: Biomechanical properties of spinal ligaments and a histological study of the supraspinal ligament in traction. J Biomech 18: S. 167–176 (1985)
31. Cherniack R M, Farhi L E, Armstrong B W, Proctor D F: A Comparison of Esophageal and Intrapleural Pressure in Man. , *Journal of Applied Physiology*, 8: . S. 203–211 (1955)
32. Chetcuti P, Myers N A, Phelan P D, Beasley S W, Dickens D R V: Chest wall deformity in patients with repaired esophageal atresia. J Pediatr Surg 24: S. 244–247 (1989)
33. Clauser C E: Weigth, volume, and center of mass of segments of the human body. S. 109 (1969)
34. Clin J, Aubin C-É, Parent S: Biomechanical Simulation and Analysis of Scoliosis Correction Using a Fusionless Intravertebral Epiphyseal Device. Spine (Phila Pa 1976) 40: S. 369–376 (2015)
35. Coulam C M, Wood E H: Regional differences in pleural and esophageal pressures in head-up and head-down positions. J Appl Physiol 31: S. 277–287 (1971)
36. Crisco J J, Panjabi M M, Yamamoto I, Oxland T R: Euler stability of the human ligamentous lumbar spine. Part II: Experiment. Clin Biomech 7: S. 27–32 (1992)
37. D'Angelo E, Agostoni E: Continuous recording of pleural surface pressure at various sites. Respir Physiol 19: S. 356–368 (1973)
38. Dempster W, Gaughran G: Properties of body segments based on size and weight. Am J Anat 18: S. 33–54 (1967)
39. DeRosa G P: Progressive scoliosis following chest wall resection in children. Spine (Phila Pa 1976) 10: S. 618–622 (1985)
40. Desbiens-Blais F, Clin J, Parent S, Labelle H, Aubin C-E: New brace design combining

CAD/CAM and biomechanical simulation for the treatment of adolescent idiopathic scoliosis. Clin Biomech (Bristol, Avon) 27: S. 999–1005 (2012)

41. Dickson R a, Deacon P: Spinal growth. J Bone Joint Surg Br 69: S. 690–692 (1987)
42. Doelken P, Huggins J T ., Pastis N J ., Sahn S A: Pleural manometry. Chest 126: S. 1764–9 (2004)
43. Dreischarf M, Zander T, Shirazi-Adl a, Puttlitz C M, Adam C J, Chen C S, Goel V K, Kiapour a, Kim Y H, Labus K M, Little J P, Park W M, Wang Y H, Wilke H J, Rohlmann a, Schmidt H: Comparison of eight published static finite element models of the intact lumbar spine: predictive power of models improves when combined together. J Biomech 47: S. 1757–66 (2014)
44. Dunlay R P, Jones K B, Weinstein S L: Scoliosis caused by rib fusion following thoracotomy for tracheoesophageal fistula: case report. Iowa Orthop J 27: S. 95–8 (2007)
45. Dunn H K, Aiona M D: Spinal instrumentation and fusion for idiopathic scoliosis in a renal-transplant patient: a case report. Spine (Phila Pa 1976) 7: S. 177–179 (1982)
46. Duprey S, Subit D, Guillemot H, Kent R W: Biomechanical properties of the costovertebral joint. Med Eng Phys 32: S. 222–7 (2010)
47. Durning R P, Scoles P V, Fox O D: Scoliosis after thoracotomy in tracheoesophageal fistula patients. A follow-up study. J Bone Joint Surg Am 62: S. 1156–1159 (1980)
48. Ebara S, Iatridis J C, Setton L a, Foster R J, Mow V C, Weidenbaum M: Tensile properties of nondegenerate human lumbar anulus fibrosus. , *Spine*, 21: . S. 452–461 (1996)
49. Eberlein R, Holzapfel G, Schulte-Bauer C: An Anisotropic Model for Annulus Tissue and Enhanced Finite Element Analyses of Intact Lumbar Disc Bodies. Comput Methods Biomech Biomed Engin 4: S. 209–229 (2001)
50. Eckert M, Fayet M, Cheze L, Bouquet R, Voiglio E, Verriest J: Costovertebral joint behaviour during frontal loading of the thoracic cage. , *IRCOBI Conference, Sept 20-22*. S. 195–206 (2000)
51. El-Rich M, Shirazi-Adl A, Arjmand N: Muscle activity, internal loads, and stability of the human spine in standing postures: combined model and in vivo studies. Spine (Phila Pa 1976) 29: S. 2633–42 (2004)
52. Feiz H H, Afrasiabi A, Parvizi R, Safarpour A, Fouladi R F: Scoliosis after

thoracotomy/sternotomy in children with congenital heart disease. Indian J Orthop 46: S. 77–80 (2012)

53. Frost H M: Skeletal structural adaptations to mechanical usage (SATMU): 1. Redefining Wolff's Law: The Bone Modeling Problem. Anat Rec 226: S. 403–413 (1990)
54. Frost H M: Skeletal structural adaptations to mechanical usage (SATMU): 2. Redefinigns Wolff's Law: The Bone Remodelling Problem. Anat Rec 226: S. 414–422 (1990)
55. Galbusera F, Bassani T, La Barbera L, Ottardi C, Schlager B, Brayda-Bruno M, Villa T, Wilke H-J: Planning the Surgical Correction of Spinal Deformities: Toward the Identification of the Biomechanical Principles by Means of Numerical Simulation. Front Bioeng Biotechnol 3: S. 1–14 (2015)
56. Galbusera F, Schmidt H, Noailly J, Malandrino A, Lacroix D, Wilke H-J, Shirazi-Adl A: Comparison of four methods to simulate swelling in poroelastic finite element models of intervertebral discs. J Mech Behav Biomed Mater 4: S. 1234–1241 (2011)
57. Galbusera F, Schmidt H, Wilke H-J: Lumbar interbody fusion: a parametric investigation of a novel cage design with and without posterior instrumentation. Eur Spine J 21: S. 455–62 (2012)
58. De George F V, Fisher R L: Idiopathic scoliosis: genetic and environmental aspects. J Med Genet 4: S. 251–7 (1967)
59. Ghezelbash F, Shirazi-Adl A, Arjmand N, El-Ouaaid Z, Plamondon A, Meakin J R: Effects of sex, age, body height and body weight on spinal loads: Sensitivity analyses in a subject-specific trunk musculoskeletal model. J Biomech 49: S. 3492–3501 (2016)
60. Glotzbecker M P, Gold M, Puder M, Hresko M T: Scoliosis after chest wall resection. J Child Orthop 7: S. 301–307 (2013)
61. Gréalou L, Aubin C E, Sevastik J A, Labelle H: Simulations of Rib Cage Surgery for the Management of Scoliotic Deformities. , *Studies in health technology and informatics*. [Online]. Verfügbar unter: http://www.ncbi.nlm.nih.gov/pubmed/15456059. [Zugegriffen: 30-Sep-2013] (2002)
62. Grundler S: In-vitro-Untersuchungen zur segmentalen Beweglichkeit der thorakalen

Wirbelsäule mit schrittweiser Reduktion von anatomischen Strukturen. , Universität Ulm (2017)

63. Guo X, Chau W W, Chan Y L, Cheng J C Y: Relative anterior spinal overgrowth in adolescent idiopathic scoliosis. Results of disproportionate endochondral-membranous bone growth. J Bone Jt Surg Br Vol 85: S. 1026–1031 (2003)
64. Hajji M A, Wilson T A, Lai-Fook S J: Improved measurements of shear modulus and pleural membrane tension of the lung. J Appl Physiol 47: S. 175–181 (1979)
65. Harkness R D: Biological functions of collagen. Biol Rev 36: S. 399–455 (1961)
66. Harless E: The static moments of the component masses of the human body. Trans Math-Phys, R Bavar Acd Set 8: S. 71–96 (1860)
67. Hefti F: Pathogenesis and biomechanics of adolescent idiopathic scoliosis (AIS). J Child Orthop 7: S. 17–24 (2013)
68. Helenius I, Jalanko H, Remes V, Sairanen H, Salminen S, Holmberg C, Palmu P, Tervahartiala P, Valta H, Sarna S, Helenius M, Mäkitie O, Peltonen J: Scoliosis after solid organ transplantation in children and adolescents. Am J Transplant 6: S. 324–30 (2006)
69. Henao J, Aubin C-É, Labelle H, Arnoux P-J: Patient-specific finite element model of the spine and spinal cord to assess the neurological impact of scoliosis correction: preliminary application on two cases with and without intraoperative neurological complications. Comput Methods Biomech Biomed Engin S. 1–10 (2015)
70. Herkommer A: In-vitro-Untersuchungen zur segmentalen Beweglichkeit der thorakalen Wirbelsäule. , Ulm University (2010)
71. Heuer F, Schmidt H, Klezl Z, Claes L, Wilke H-J: Stepwise reduction of functional spinal structures increase range of motion and change lordosis angle. J Biomech 40: S. 271–80 (2007)
72. Hindle R J, Pearcy M J, Cross a.: Mechanical function the human lumbar interspinous and supraspinous ligaments. J Biomed Eng 12: S. 340–344 (1990)
73. Hodges P W, Eriksson A E M, Shirley D, Gandevia S C: Intra-abdominal pressure increases stiffness of the lumbar spine. J Biomech 38: S. 1873–1880 (2005)
74. Holzapfel G a., Schulze-Bauer C a J, Feigl G, Regitnig P: Single lamellar mechanics of the human lumbar anulus fibrosus. Biomech Model Mechanobiol 3: S. 125–140 (2005)

75. Hueter C: Anatomische Studien an den Extremit{ä}tengelenken Neugeborener und Erwachsener. Arch f{ü}r Pathol Anat und Physiol und f{ü}r Klin Med 26: S. 484–519 (1863)

76. Hulse Neufeld J, Haghighi P, Machado T: Growth related increase in rat intervertebral disc size: a quantitative radiographic and histologic comparison. Lab Anim Sci 40: S. 303–307 (1990)

77. Hyatt R E, Bar-yishay E, Abel M D: Influence of the heart on the vertical gradient of transpulmonary pressure in dogs. J Appl Physiol 58: S. 52–57 (1985)

78. Ibrahim A F, Darwish H H: The costotransverse ligaments in human: a detailed anatomical study. Clin Anat 18: S. 340–5 (2005)

79. Jacobsen S, Rosenklint A, Halkier E: Post-Pneumonectomy Scoliosis. Acta Orthop Scand 45: S. 867–872 (1974)

80. Janssen M M a, Kouwenhoven J-W M, Schlösser T P C, Viergever M a, Bartels L W, Castelein R M, Vincken K L: Analysis of preexistent vertebral rotation in the normal infantile, juvenile, and adolescent spine. Spine (Phila Pa 1976) 36: S. E486--E491 (2011)

81. Janssen M M A, Vincken K L, Kemp B, Obradov M: Pre-existent vertebral rotation in the human spine is influenced by body position. S. 1728–1734 (2010)

82. Janssen M M A, de Wilde R F, Kouwenhoven J-W M, Castelein R M: Experimental animal models in scoliosis research: a review of the literature. Spine J 11: S. 347–58 (2011)

83. Jones E, Oliphant T, Peterson P, others: {SciPy}: Open source scientific tools for {Python}. . (2017)

84. Julkunen P, Wilson W, Isaksson H, Jurvelin J S, Herzog W, Korhonen R K: A review of the combination of experimental measurements and fibril-reinforced modeling for investigation of articular cartilage and chondrocyte response to loading. Comput Math Methods Med 2013: (2013)

85. Kawakami N, Winter R B, Lonstein J E, Denis F: Scoliosis secondary to rib resection. J Spinal Disord 7: S. 522–7 (1994)

86. Kawamata M, Omote K, Namiki A, Miyabe M: Measurement of intercostal and pleural pressures by epidural catheter. Anaesthesia 49: S. 208–210 (1994)

87. Keaveny T M, Hayes W C: A 20-year perspective on the mechanical properties of

trabecular bone. J Biomech Eng 115: S. 534–542 (1993)

88. Kindig M, Li Z, Kent R, Subit D: Effect of intercostal muscle and costovertebral joint material properties on human ribcage stiffness and kinematics. Comput Methods Biomech Biomed Engin 18: S. 556–570 (2015)
89. Kindsfater K, Lowe T, Lawellin D, Weinstein D, Akmakjian J: Levels of platelet calmodulin for the prediction of progression and severity of adolescent idiopathic scoliosis. J Bone Joint Surg Am 76: S. 1186–1192 (1994)
90. de Kleuver M, Lewis S J, Germscheid N M, Kamper S J, Alanay A, Berven S H, Cheung K M, Ito M, Lenke L G, Polly D W, Qiu Y, van Tulder M, Shaffrey C: Optimal surgical care for adolescent idiopathic scoliosis: an international consensus. Eur Spine J 23: S. 2603–2618 (2014)
91. Kouwenhoven J W, Castelein R M: The pathogenesis of adolescent idiopathic scoliosis: review of the literature. Spine (Phila Pa 1976) 33: S. 2898–2908 (2008)
92. Kouwenhoven J-W M, Bartels L W, Vincken K L, Viergever M a, Verbout A J, Delhaas T, Castelein R M: The relation between organ anatomy and pre-existent vertebral rotation in the normal spine: magnetic resonance imaging study in humans with situs inversus totalis. Spine (Phila Pa 1976) 32: S. 1123–1128 (2007)
93. Kouwenhoven J-W M, Vincken K L, Bartels L W, Castelein R M: Analysis of preexistent vertebral rotation in the normal spine. Spine (Phila Pa 1976) 31: S. 1467–72 (2006)
94. Kouwenhoven J-W M, Vincken K L, Bartels L W, Meij B P, Oner F C, Castelein R M: Analysis of Preexistent Vertebral Rotation in the Normal Quadruped Spine. Spine (Phila Pa 1976) 31: S. E754-8 (2006)
95. Kouwenhoven J W M, Van Ommeren P M, Pruijs H E J, Castelein R M: Spinal decompensation in neuromuscular disease. Spine (Phila Pa 1976) 31: S. 188–191 (2006)
96. Krueger J J, Bain T, Patterson J L: Elevation gradient of intrathoracic pressure. J Appl Physiol 16: S. 465–468 (1961)
97. Lai-Fook S J, Rodarte J R: Pleural pressure distribution and its relationship to lung volume and interstitial pressure. J Appl Physiol 70: S. 967–978 (1991)
98. Lai-Fook S J: Pleural mechanics and fluid exchange. Physiol Rev 84: S. 385–410 (2004)

99. Lam K S, Mehdian H: The importance of an intact abdominal musculature mechanism in maintaining spinal sagittal balance: Case illustration in prune-belly syndrome. , *Spine*, 24: . S. 719–722 (1999)

100. Langdahl B, Ferrari S, Dempster D W: Bone modeling and remodeling: potential as therapeutic targets for the treatment of osteoporosis. Ther Adv Musculoskelet Dis 8: S. 225–235 (2016)

101. Langenskiöld a., Michelsson J-E: The Pathogenesis of Experimental Progressive Scoliosis. Acta Orthop 33: S. 3–26 (1962)

102. Langenskiold A, Michelsson J: Experimental Progressive Scoliosis in the Rabbit. J Bone Jt Surg 43B: S. 116–20 (1961)

103. Lemos M, Pozo R M K, Montes G S, Saldiva P H N: Organization of collagen and elastic fibers studied in stretch preparations of whole mounts of human visceral pleura. Ann Anat 179: S. 447–452 (1997)

104. Lemosse D, Le Rue O, Diop a, Skalli W, Marec P, Lavaste F: Characterization of the mechanical behaviour parameters of the costo-vertebral joint. Eur Spine J 7: S. 16–23 (1998)

105. Liebsch C, Graf N, Appelt K, Wilke H-J: The rib cage stabilizes the human thoracic spine: An in vitro study using stepwise reduction of rib cage structures. PLoS One 12: S. e0178733 (2017)

106. Liebsch C, Graf N, Wilke H J: Wire cerclage can restore the stability of the thoracic spine after median sternotomy: an in vitro study with entire rib cage specimens. Eur Spine J S. 1–7 (2016)

107. Little J P, Adam C: Development of a computer simulation tool for application in adolescent spinal deformity surgery. Lect Notes Comput Sci (including Subser Lect Notes Artif Intell Lect Notes Bioinformatics) 5958 LNCS: S. 90–97 (2010)

108. Little J P, Adam C: Patient-specific computational biomechanics for simulating adolescent scoliosis surgery: Predicted vs clinical correction for a preliminary series of six patients. Int j numer method biomed eng 27: S. 347–356 (2011)

109. Little J P P, Adam C J J: Geometric sensitivity of patient-specific finite element models of the spine to variability in user-selected anatomical landmarks. Comput Methods Biomech Biomed Engin S. 37–41 (2013)

110. Little J P, Adam C J: The effect of soft tissue properties on spinal flexibility in

scoliosis: biomechanical simulation of fulcrum bending. Spine (Phila Pa 1976) 34: S. E76-82 (2009)

111. Little J P, Izatt M T, Labrom R D, Askin G N, Adam C J: An FE investigation simulating intra-operative corrective forces applied to correct scoliosis deformity. Scoliosis 8: S. 9 (2013)
112. Liu S, Margulies S S, Wilson T A: Deformation of the dog lung in the chest wall. J Appl Physiol 68: S. 1979–1987 (1990)
113. Lonstein J E, Carlson J M: The prediction of curve progression in untreated idiopathic scoliosis during growth. J Bone Joint Surg Am 66: S. 1061–1071 (1984)
114. Lowe T, Edgar M, Margulies J: Etiology of Idiopathic Scoliosis: Current Trends in Research. J Bone Jt Surg 82: S. 1157 (2000)
115. Loynes R: Scoliosis after thoracoplasty. J Bone Jt Surg Br S. 484–98 (1972)
116. Lu Y M, Hutton W C, Gharpuray V M: Do bending, twisting, and diurnal fluid changes in the disc affect the propensity to prolapse? A viscoelastic finite element model. Spine (Phila Pa 1976) 21: S. 2570–9 (1996)
117. Machida M, Dubousset J, Imamura Y, Miyashita Y, Yamada T, Kimura J: Melatonin. A possible role in pathogenesis of adolescent idiopathic scoliosis. , *Spine*, 21: . S. 1147–52 (1996)
118. Majdouline Y, Aubin C-E, Wang X, Sangole A, Labelle H: Preoperative assessment and evaluation of instrumentation strategies for the treatment of adolescent idiopathic scoliosis: computer simulation and optimization. Scoliosis 7: S. 21 (2012)
119. Majdouline Y, Aubin C E, Sangole A, Labelle H: Computer simulation for the optimization of instrumentation strategies in adolescent idiopathic scoliosis. Med Biol Eng Comput 47: S. 1143–1154 (2009)
120. Malandrino A, Noailly J, Lacroix D: Regional annulus fibre orientations used as a tool for the calibration of lumbar intervertebral disc finite element models. Comput Methods Biomech Biomed Engin 5842: S. 37–41 (2013)
121. Mannion F, Meier M, Grob D, Müntener M: Paraspinal muscle fibre type alterations associated with scoliosis: an old problem revisited with new evidence. Eur Spine J 7: S. 289–93 (1998)
122. McMahon S M, Proctor D F, Permutt S: Pleural surface pressure in dogs. J Appl Physiol 27: S. 881–885 (1969)

123. Mente P L, Stokes I a, Spence H, Aronsson D D: Progression of vertebral wedging in an asymmetrically loaded rat tail model. Spine (Phila Pa 1976) 22: S. 1292–1296 (1997)

124. Michelsson J E: The development of spinal deformity in experimental scoliosis. Acta Orthop Scand Suppl S. Suppl 81:1-91 (1965)

125. Milanesi R, Caregnato R C A: Intra-abdominal pressure: an integrative review. Einstein (São Paulo) 14: S. 423–430 (2016)

126. Molina D K, DiMaio V J M: Normal organ weights in men: part I-the heart. Am J Forensic Med Pathol 33: S. 362–7 (2012)

127. Molina D K, DiMaio V J M: Normal organ weights in men: part II-the brain, lungs, liver, spleen, and kidneys. Am J Forensic Med Pathol 33: S. 368–72 (2012)

128. Moore K L, Dalley A F, Agur A M R: Clinically oriented anatomy, 53: . Lippincott Williams & Wilkins, (2013)

129. Nachlas I W, Borden J N: Experimental scoliosis; the role of the epiphysis. Surg Gynecol Obstet 90: S. 672–680 (1950)

130. Negrini S, Minozzi S, Chockalingam N, Tb G, Kotwicki T, Maruyama T, Romano M, Zaina F: Braces for idiopathic scoliosis in adolescents (Review). (2015)

131. Negrini S, Aulisa A G, Aulisa L, Circo A B, de Mauroy J C, Durmala J, Grivas T B, Knott P, Kotwicki T, Maruyama T, Minozzi S, O'Brien J P, Papadopoulos D, Rigo M, Rivard C H, Romano M, Wynne J H, Villagrasa M, Weiss H-R, Zaina F: 2011 SOSORT guidelines: Orthopaedic and Rehabilitation treatment of idiopathic scoliosis during growth. Scoliosis 7: S. 3 (2012)

132. Newell N, Grant C A, Keenan B E, Izatt M T, Pearcy M J, Adam C J: Quantifying Progressive Anterior Overgrowth in the Thoracic Vertebrae of Adolescent Idiopathic Scoliosis Patients: A Sequential Magnetic Resonance Imaging Study. Spine J 41: S. E382–E387 (2016)

133. Niemeyer F, Wilke H-J, Schmidt H: Geometry strongly influences the response of numerical models of the lumbar spine—A probabilistic finite element analysis. J Biomech 45: S. 1414–1423 (2012)

134. Oda I, Abumi K, Lü D, Shono Y, Kaneda K: Biomechanical role of the posterior elements, costovertebral joints, and rib cage in the stability of the thoracic spine. Spine (Phila Pa 1976) (1996)

135. Oliphant T E: Python for scientific computing. , *Computing in Science and Engineering*, 9: . S. 10–20 (2007)
136. Paulsen F, Waschke J: Atlas der Anatomie des Menschen : Bd. 2., Brust, Bauch, Becken, untere Extremitäten, Haut / Sobotta. Urban & Schwarzenberg, München ; Wien ; Baltimore (1982)
137. Pearsall D J, Reid J G, Ross R: Inertial properties of the human trunk of males determined from magnetic resonance imaging. Ann Biomed Eng 22: S. 692–706 (1994)
138. Pearsall D, Reid J, Livingston L: Segmental inertial parameters of the human trunk as determined from computed tomography. Ann Biomed Eng S. 198–210 (1996)
139. Petit Y, Aubin C E, Labelle H: Patient-specific mechanical properties of a flexible multi-body model of the scoliotic spine. Med Biol Eng Comput 42: S. 55–60 (2004)
140. Pingel T H: Beitrag zur Herleitung und numerischen Realisierungeines mathematischen Modells der menschlichen Wirbelsaüle. (1991)
141. Pintar F, Yoganandan N, Myers T, Elhagediab A, Sances A: Biomechanical properties of human lumbar spine ligaments. J Biomech 25: S. 1351–1356 (1992)
142. Porter R W: Can a short spinal cord produce scoliosis?. Eur Spine J 10: S. 2–9 (2001)
143. Porter R: Idiopathic scoliosis: the relation between the vertebral canal and the vertebral bodies. Spine (Phila Pa 1976) S. 1360–1366 (2000)
144. Rohlmann a, Zander T, Rao M, Bergmann G: Applying a follower load delivers realistic results for simulating standing. J Biomech 42: S. 1520–6 (2009)
145. Romano M, Minozzi S, Zaina F, Saltikov J B, Chockalingam N, Kotwicki T, Hennes A M, Negrini S: Exercises for Adolescent Idiopathic Scoliosis. Spine (Phila Pa 1976) 38: S. E883–E893 (2013)
146. Roth M: Idiopathic scoliosis from the point of view of the neuroradiologist. Neuroradiology 21: S. 133–138 (1981)
147. Russell G G, Raso V J, Hill D, McIvor J: A comparison of four computerized methods for measuring vertebral rotation. Spine (Phila Pa 1976) 15: S. 24–7 (1990)
148. Rutishauser W J, Banchero N, Tsakiris A G, Edmundowicz A C, Wood E H: Pleural pressures at dorsal and ventral sites in supine and prone body positions. J Appl Physiol 21: S. 1500–1510 (1966)
149. Rutishauser W J, Banchero N, Tsakiris A G, Wood E H: Effect of gravitational and

inertial forces on pleural and esophageal pressures. J Appl Physiol 22: S. 1041–1052 (1967)

150. Scapinelli R, Stecco C, Pozzuoli A, Porzionato A, Macchi V, De Caro R: The lumbar interspinous ligaments in humans: Anatomical study and review of the literature. Cells Tissues Organs 183: S. 1–11 (2006)
151. Schlager B, Krump F, Boettinger J, Niemeyer F, Ruf M, Kleiner S, Beer M, Wilke H J: Characteristic morphological patterns within adolescent idiopathic scoliosis may be explained by mechanical loading. Eur Spine J 27: S. 2184–2191 (2018)
152. Schlager B, Niemeyer F, Galbusera F, Volkheimer D, Jonas R, Wilke H-J: Uncertainty analysis of material properties and morphology parameters in numerical models regarding the motion of lumbar vertebral segments. Comput Methods Biomech Biomed Engin S. 1–11 (2018)
153. Schlager B, Niemeyer F, Galbusera F, Wilke H J: Asymmetrical intrapleural pressure distribution: a cause for scoliosis? A computational analysis. Eur J Appl Physiol 118: S. 1315–1329 (2018)
154. Schlager B, Niemeyer F, Liebsch C, Galbusera F, Boettinger J, Vogele D, Wilke H-J: Influence of morphology and material properties on the range of motion of the costovertebral joint - a probabilistic finite element analysis. Comput Methods Biomech Biomed Engin S. 1–9 (2018)
155. Schlösser T P C, Van Der Heijden G J M G, Versteeg A L, Castelein R M: How „idiopathic“ is adolescent idiopathic scoliosis? A systematic review on associated abnormalities. PLoS One 9: S. 1–10 (2014)
156. Schmidt H, Heuer F, Wilke H-J: Which axial and bending stiffnesses of posterior implants are required to design a flexible lumbar stabilization system?. J Biomech 42: S. 48–54 (2009)
157. Schultz A, Benson D, Hirsch C: Force-deformation properties of human costo-sternal and costo-vertebral articulations. J Biomech 7: S. 311–318 (1974)
158. Schwab F, Dubey A, Gamez L, El Fegoun A B, Hwang K, Pagala M, Farcy J P: Adult scoliosis: prevalence, SF-36, and nutritional parameters in an elderly volunteer population. Spine (Phila Pa 1976) 30: S. 1082–1085 (2005)
159. Sham M L, Zander T, Rohlmann A, Bergmann G: Effects of the rib cage on thoracic spine flexibility. Biomed Tech Biomed Eng 50: S. 361–365 (2005)

160. Shen W, Niu Y, Mattrey R F, Fournier A, Corbeil J, Kono Y, Stuhmiller J H: Development and validation of subject-specific finite element models for blunt trauma study. J Biomech Eng 130: S. 021022 (2008)
161. Shirazi-Adl A, Ahmed A M, Shrivastava S C: Mechanical response of a lumbar motion segment in axial torque alone and combined with compression. Spine (Phila Pa 1976) 11: S. 914–27 (1986)
162. Shono Y, Kaneda K, Yamamoto I: A biomechanical analysis of Zielke, Kaneda, and Cotrel-Dubousset instrumentations in thoracolumbar scoliosis. A calf spine model. Spine (Phila Pa 1976) 16: S. 1305–1311 (1991)
163. Simon P, Orías A A E, Andersson G B J, An H S, Inoue N: In Vivo Topographic Analysis of Lumbar Facet Joint Space Width Distribution in Healthy and Symptomatic Subjects. Spine (Phila Pa 1976) 37: S. 1058–1064 (2012)
164. Soyer T, Karnak I, Ciftci A O, Senocak M E, Tanyel F C, Büyükpamukçu N: The results of surgical treatment of chest wall tumors in childhood. Pediatr Surg Int 22: S. 135–139 (2006)
165. Stålbom M: Musculoskeletal system simulations to analyse muscle forces and movement pattern. (2008)
166. Stokes I A F: Mechanical effects on skeletal growth. J Musculoskelet Neuronal Interact 2: S. 277–280 (2002)
167. Stokes I A, Spence H, Aronsson D D, Kilmer N: Mechanical modulation of vertebral body growth. Implications for scoliosis progression. Spine (Phila Pa 1976) 21: S. 1162–1167 (1996)
168. Stokes I, Windisch L: Vertebral height growth predominates over intervertebral disc height growth in adolescents with scoliosis. Spine (Phila Pa 1976) 31: S. 1600–1604 (2006)
169. Stokes I a. F, Spence H, Aronsson D D, Kilmer N: Mechanical Modulation of Vertebral Body Growth. , *Spine*, 21: . S. 1162–1167 (1996)
170. Sundaram S H H ., Feng C C C: Finite Element Analysis of the human thorax. J Biomech 10: S. 505–516 (1977)
171. Surprenant E L, Rodbard S: A hydrostatic pressure gradient in the pleural sac. Am Heart J 66: S. 215–220 (1963)
172. Ueno, Liu: A three-dimensional nonlinear finite element model of lumbar

intervertebral joint in torsion. J Biomech Eng 109: S. 200–9 (1987)

173. Urban J P, Roberts S: Development and degeneration of the intervertebral discs. Mol Med Today 1: S. 329–335 (1995)
174. Vergari C, Ribes G, Aubert B, Adam C, Miladi L, Ilharreborde B, Abelin-Genevois K, Rouch P, Skalli W: Evaluation of a Patient-Specific Finite-Element Model to Simulate Conservative Treatment in Adolescent Idiopathic Scoliosis. Spine Deform 3: S. 4–11 (2015)
175. Vezin P, Berthet F: Structural characterization of human rib cage behavior under dynamic loading. Stapp Car Crash J 53: S. 93–125 (2009)
176. Viceconti M, Olsen S, Nolte L P, Burton K: Extracting clinically relevant data from finite element simulations. Clin Biomech 20: S. 451–454 (2005)
177. Volkmann R: Die Krankheiten der Bewegungsorgane. Handb der Allg und Spez Chir Bd II, Abt 1: S. 350–351 (1869)
178. Wang P M, Lai-Fook S J: Effect of mechanical ventilation on regional variation of pleural liquid thickness in rabbits. Lung 175: S. 165–173 (1997)
179. Wang S, Qiu Y, Zhu Z, Ma Z, Xia C: Histomorphological study of the spinal growth plates from the convex side and the concave side in adolescent idiopathic scoliosis. 10: S. 1–10 (2007)
180. Wang X, Aubin C-E, Robitaille I, Labelle H: Biomechanical comparison of alternative densities of pedicle screws for the treatment of adolescent idiopathic scoliosis. Eur Spine J 21: S. 1082–90 (2012)
181. Weinstein S L, Dolan L a, Cheng J C Y, Danielsson A, Morcuende J a: Adolescent idiopathic scoliosis. Lancet 371: S. 1527–37 (2008)
182. Wenger D R, Carollo J J, Wilkerson J a, Wauters K, Herring J a: Laboratory testing of segmental spinal instrumentation versus traditional Harrington instrumentation for scoliosis treatment. Spine (Phila Pa 1976) 7: S. 265–269
183. Wiener-Kronish J P, Gropper M A, Lai-Fook S J: Pleural liquid pressure in dogs measured using a rib capsule. , *Journal of Applied Physiology*, 59: . S. 597–602 (1985)
184. Wilke H J, Neef P, Caimi M, Hoogland T, Claes L E: New in vivo measurements of pressures in the intervertebral disc in daily life. Spine (Phila Pa 1976) 24: S. 755–62 (1999)

185. Wilke H-J, Geppert J, Kienle A: Biomechanical in vitro evaluation of the complete porcine spine in comparison with data of the human spine. Eur Spine J 20: S. 1859–68 (2011)

186. Wilke H-J, Mathes B, Midderhoff S, Graf N: Development of a scoliotic spine model for biomechanical in vitro studies. Clin Biomech 30: S. 182–187 (2015)

187. Wilke H J, Herkommer A, Werner K, Liebsch C: In vitro analysis of the segmental flexibility of the thoracic spine. PLoS One 12: S. 1–16 (2017)

188. Wilke H J, Jungkunz B, Wenger K, Claes L E: Spinal segment range of motion as a function of in vitro test conditions: Effects of exposure period, accumulated cycles, angular- deformation rate, and moisture condition. Anat Rec 251: S. 15–19 (1998)

189. Wilson T a, Rehder K, Krayer S, Hoffman E a, Whitney C G, Rodarte J R: Geometry and respiratory displacement of human ribs. J Appl Physiol 62: S. 1872–1877 (1987)

190. Wolff J: Das Gesetz der Transformation der Knochen. DMW - Dtsch Medizinische Wochenschrift 19: S. 1222–1224 (1893)

191. Wood E H, Nolan A C, Donald D E, Edmundowicz A C, Marshall H W: Technics for Measurement of Intrapleural and Pericardial Pressures in Dogs Studied Without Thoracotomy and Methods for Their Application To Study of Intrathoracic Pressure Relationships During Exposure To Forward Acceleration. Mayo Clin Rochester Mn S. 1–3 (1963)

192. Wozniczka J K, Ledonio C G T, Polly D W, Rosenstein B E, Nuckley D J: Adolescent Idiopathic Scoliosis Thoracic Volume Modeling: The Effect of Surgical Correction. J Pediatr Orthop (2016)

193. Wu H C, Yao R F: Mechanical behavior of the human annulus fibrosus. J Biomech 9: S. 1–7 (1976)

194. Yekutiel M, Robin G C, Yarom R: Proprioceptive function in children with adolescent idiopathic scoliosis. Spine (Phila Pa 1976) 6: S. 560–566 (1981)

195. Yoshida T: Anatomy and development of elastic fibers in human pleurae. In: Kawasaki Igakkaishi, Kawasaki Igakkaishi, , S. 83–91 (1991)

196. Zaleske D J, Ehrlich M G, Hall J E: Association of glycosaminoglycan depletion and degradative enzyme activity in scoliosis. Clin Orthop Relat Res S. 177–181 (1980)

197. Zander T, Rohlmann A, Bergmann G: Influence of ligament stiffness on the mechanical behavior of a functional spinal unit. J Biomech 37: S. 1107–11 (2004)

Appendix

A-1. Raw data of RoM data of Figure 18 and 19.

Table 10: Mean and the standard-deviation (SD) of the RoM in flexion and extension of different vertebral segments. Data obtained from in vitro experiments. Values plotted in Figure 18b.

Moment [Nm]	Vertebral segment	ROM in Flexion-Extension mean [°]	SD
2.5	T1-T2	7.01	0.47
	T2-T3	5.13	2.96
	T3-T4	3.88	1.07
	T4-T5	3.42	0.86
	T5-T6	3.93	1.42
	T6-T7	5.73	0.55
	T7-T8	2.78	0.66
	T8-T9	3.26	0.75
	T9-T10	3.60	0.89
	T10-T11	3.50	1.15
7.5	T11-T12	3.64	0.81
	T12-L1	6.69	2.16
	L1-L2	7.14	2.09
	L2-L3	9.72	3.99
	L3-L4	8.16	2.21
	L4-L5	11.47	3.61
	L5-S1	12.06	5.47

Table 11: Standard deviation of the RoM values relative to the intact condition at flexion-extension for the thoracic region (T2-T3) and the lumbar region (L4-L5). In vitro data was obtained from Heuer [71].

T2-T3 Resection step	**Flexion-Extension**		**lateral bending**		**axial rotation**	
	Min-Sd	Max-Sd	Min-Sd	Max-Sd	Min-Sd	Max-Sd
(intact)	1.00	1.00	0.90	1.27	1.04	1.31
ssl	1.00	1.07	0.92	1.28	1.08	1.33
isl	1.01	1.09	0.92	1.28	1.09	1.35
lf	1.04	1.17	0.94	1.30	1.09	1.42
cl	1.10	1.18	0.92	1.38	1.19	1.71
va	1.65	1.89	0.95	1.56	1.62	2.19
pll	1.76	2.13	0.92	1.70	1.66	2.55
all	1.89	2.51	1.03	1.80	1.67	2.72
nuc	2.37	2.94	1.27	2.27	1.94	3.12

L4-L5 Resection step	**Flexion-Extension**		**lateral bending**		**axial rotation**	
	Min-Sd	Max-Sd	Min-Sd	Max-Sd	Min-Sd	Max-Sd
(intact)	1	1	0.88	1.18	0.28	0.76
ssl	1.06	1.1	0.98	1.24	0.3	0.8
isl	1.06	1.12	0.97	1.23	0.31	0.81
lf	1.11	1.17	0.98	1.24	0.32	0.82
cl	1.15	1.21	1	1.24	0.35	0.95
va	1.22	1.8	0.99	1.33	0.55	1.45
pll	1.26	1.86	1.01	1.35	0.56	1.48
all	1.43	2.55	1.08	1.42	0.57	1.55
nuc	2.07	3.29	1.48	1.84	1.18	2.24

A-2. Material calibration process

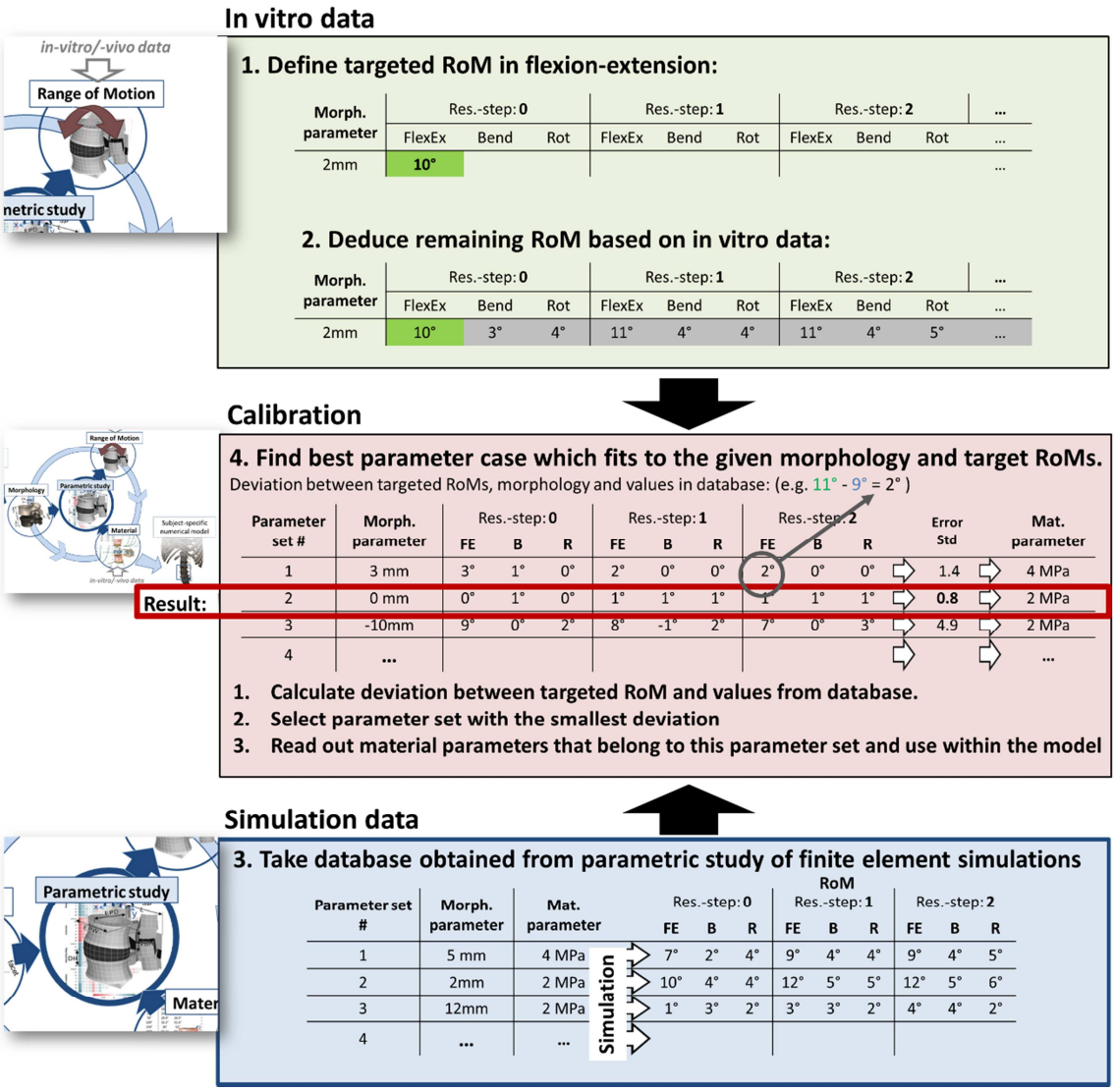


Figure 50: Schema of the basic material calibration process. At first, a range of motion (RoM) is defined in flexion-extension at the intact condition, Resection (Res.) step 0. Secondly, the remaining RoMs are estimated based on the in-vitro data (see A-1). From the parameter database, obtained from parametric studies, the parameter set is selected which fits best to the targeted RoM and morphology.

A-3. The ParaSpine program

The ParaSpine program generates a finite element model of the spine and chest. Input into the program are mainly landmark or parameter data. As an output a complete FE-Model with adjusted material properties is obtained. Within the program the range of the vertebral levels, as well the rib cage and muscles can be included.

It is divided into multiple sub-modules, which all can be executed independently. All necessary files for running the program should be included in the folder called "ParaSense". These file are:

File	Description
ParaSpine_setup.txt	Includes all specifications, such as • which vertebral levels should be generated • include chest and/or muscles • default parameters
ParaSpine_para.txt	All parameters, including their default values, that are necessary to build the geometry in Ansys
ParaSpine_Material.txt	Table of all material parameters and properties for each vertebral level
ParaSpine_Para.txt	List of all morphology parameters and their values of each vertebral and rib level.
Folder: "Landmarks"	Includes files of the coordinates of the landmarks.

The main python script

This script is the main script that loads all sub-modules. It is called using the "run_paraspine()" command.

```
def run_paraspine(imp_para, target_path, module):
    """Import module
    Input Parameters:
```

imp_para :	List	Includes parameters that are do be changed. It is distinguished between geometry and material parameters: - geometry parameter: ["paraname:vertnumber",value] - material parameter: ["paraname:index:vertnumber:dim",value] Whereas e.g. stress: dim=1, strain: dim=2 e.g. imp_para = [["para1:24",1.232],["matpara:-:22:1",33.2]],
target_path:	String	Path to which results should be copied to. If files should stay

		in inital "name" folder type: ""
module:	List of integer	which module should be acitvated

Local parameters:

Para_data	dictionary	Contains the parameters that are to be changed (material 'm', geometry 'g').
path	dictionary	contains all path directions

```
    #================================================================
    #---CHECK input content
    if isinstance(imp_para, list)==False:
            print("INPUT-ERROR: imp_para must be a list! e.g.
            imp_para=[]")
            exit()

            if module==[]:    #default model generation from landmarks
            module=[1,2,3,4,5]
    #----------------------------------------------------------------
    if target_path!="":
            path["NewPath"] = target_path
    else:
            path["NewPath"] = path["study_res"]
    #================================================================
    """Calculate from Xray-point data anatomical parameters  """
    if 0 in module:
            path_py = path["py"]+"\\Xray2Para"
            exec(compile(open(path_py+"\\RUN_Xray2Para.py").read(),
            path_py+"\\RUN_Xray2Para.py", 'exec'))
    #================================================================
"""Calculate from CT-landmarks anatomical parameters. Scripts:
Landmarks2Para. Add also RoM-calibration values"""

    if 1 in module:
        path_py = path["py"]+"\\Landmarks2Para"
        exec(compile(open(path_py+"/RUN_Landmarks2Para.py").read(),
        path_py+"/RUN_Landmarks2Para.py", 'exec'))
    #================================================================
    """Calibrate material properties for each vert and CVJ """
    if 11 in module:
            print("Run_Calibration running")
            from SpineCalibration import Run_Calibration_ThLu
            path_py = path["py"]+"\\SpineCalibration"
            imp_para = Run_Calibration_V2.mat_calibration(SpineData,
                            imp_para, path)
    #================================================================
    """Modify input parameters """
    """ Check if imported parameters are valid and create dictionary
Para_data """
    if len(imp_para)!=0:
            print("Write and edit parameter file (ParaSpine_Para.txt)...")
            Para_data,check = modify_para.dicParaData(imp_para, SpineData, ParaData, path)
            if check==False:
                    wait=input("Error")
                    exit()
            modify_para.parafile(Para_data,path)
```

```
    #=====================================================================
    """Para2Para: Modify/estimate missing parameters """
    if 2 in module:
            org_data.init(2,path)
            path_py = path["py"]+"\Para2Para"
            exec(compile(open(path_py+"/RUN_Para2Para.py").read(),
                    path_py+"/RUN_Para2Para.py", 'exec'))
            org_data.exit(2,path)
    #=====================================================================
"""Para4Check: Checks parameters in "ParaSpine_Para.txt" if they are suitable for the model-
generation, and if not modifies them. """
    if "check" in module:
            from Para4Check import Run_Para4Check
            run_module = Run_Para4Check.para4check(SpineData,path)
#=====================================================================
    """Para2Ansys: Creates input files for ANSYS, which include model

parameters.""

    if 3 in module:
            org_data.init(3,path)
            path_py = path["py"]+"\Para2Ansys"
            exec(compile(open(path_py+"/RUN_para2ansys.py").read(),
            path_py+"/RUN_para2ansys.py", 'exec'))
            org_data.exit(3,path)
#=====================================================================
"""Runs ANSYS APDL script. For more detail, see the APDL main script "ParaSpine.inp" """
    if 4 in module:
            org_data.init(4,path)
            path_py = path["py"]+"\\AnsysScripts\\"
            print(path_py+"Run_BATCH_Ansys.cmd")
            os.system(path_py+"Run_BATCH_Ansys.cmd")
            org_data.exit(4,path)
#=====================================================================
    """ Material: Edit material file, that will be imported by Abaqus
"""
    if len(imp_para)!=0:
            modify_para.matfile(Para_data,SpineData,path)
#=====================================================================
    """ Generates files for ABAQUS: material (abaqmesh_material.inp).
    """
    if 5 in module:
            org_data.init(5,path)
            path_py = path["py"]+"\Ansys2Abaqus"
            exec(compile(open(path_py+"/RUN_Ansys2Abaqus.py").read(),
            path_py+"/RUN_Ansys2Abaqus.py", 'exec'))
            org_data.exit(5,path)
#=====================================================================
    """ Copy data into unique folder """
    if target_path!="":
            org_data.init(99,path)
#=====================================================================
    """ Returns path which contains all generated files """
    return target_path
```

Acknowledgment

I would like to express my deepest gratitude to my supervisor Prof. Dr. Hans-Joachim Wilke for the opportunity to work on this PhD project at the Institute of Orthopaedic Research and Biomechanics in Ulm. I thank him for his guidance throughout the dissertation, trust and providing the freedom to develop and pursue ideas.

I would like to acknowledge PD Dr. Michael Akbar from the University Hospital Heidelberg as a reviewer of this thesis.

I would like to thank PD Dr. Michael Ruf (SRH-Klinikum Bad Wildbad), PD Dr. Michael Akbar (University Hospital Heidelberg), and from Radiology Department Ulm, Prof. Dr. Meinrad Beer, Dr. Stefan Schmidt and Dr. Sebastian Kleiner for their most valuable scientific assistance and collaboration.

I thank Prof. Dr. Anita Ignatius for providing a constructive and open environment at the Institute.

Special appreciation goes to Dr. Frank Niemeyer and Dr. Fabio Galbusera for their supervision and support. In particular, I value their profound and constructive comments, reviewing various manuscripts, and the in-depth discussions.

I would like to thank all the colleagues and friends of the Spine Group for their immense support. Special thanks goes to René Jonas, David Volkheimer, Nikolas Berger-Roscher, Christian Liebsch, Laura Zengerle, Julius Böttinger and Florian Krump. For technical and administrative support I wish to thank Andrea Grau, Alexandra Naylor, Angelika Reindl, Brigitte Siegel and Werner Ohmayer. In addition, I thank all the colleagues of the Institute of Orthopaedic Research and Biomechanics for the enjoyable and pleasant work atmosphere.

Warmest gratitude goes to Hanna for her patience, support and encouragement throughout the PhD years. Finally, many thanks go to my parents and brothers!

Curriculum vitae *(removed)*